

# Optical, vibrational, thermal, electrical, damage and phase-matching properties of lithium thioindate

S. Fossier, S. Salaiin, J. Mangin and O. Bidault

*Laboratoire de Physique de l'Université de Bourgogne (UMR-CNRS 5027), 9 avenue A. Savary, F-21078 Dijon, France.*

I. Thénot and J.-J. Zondy\*

*BNM-SYRTE, Observatoire de Paris (UMR-CNRS 8630),  
61, avenue de l'Observatoire, F-75014 Paris, France.*

W. Chen

*Laboratoire de Physicochimie de l'Atmosphère (UMR-CNRS 8101)  
Université du Littoral Côte d'Opale,  
145, Av. Maurice Schumann,  
F-59140 Dunkerque, France.*

F. Rotermund† and V. Petrov

*Max-Born Institute for Nonlinear Optics and Ultrafast Spectroscopy, 2A Max-Born St, D-12489 Berlin, Germany.*

P. Petrov and J. Henningsen

*Danish Institute of Fundamental Metrology,  
B 307, Matematiktorvet, DK-2800, Lyngby, Denmark.*

A. Yelisseyev, L. Isaenko and S. Lobanov

*Design and Technological Institute for Monocrystals SB-RAS  
43, Russkaya St, RU-630058, Novosibirsk, Russia.*

O. Balachninaite,‡ G. Slekyš,‡ and V. Sirutkaitis‡

*Altechna Co. Ltd, Ukmerges 41A-203, LT-2004, Vilnius, Lithuania.*

S. Zelt

*Universität Kaiserslautern, FB Physik, Erwin-Schrödinger-Str 46, D-67663, Kaiserslautern, Germany.*

(Dated: March 24, 2019)

Lithium thioindate ( $\text{LiInS}_2$ ) is a new nonlinear chalcogenide bi-axial material transparent from 0.4 to 12  $\mu\text{m}$ , that has been successfully grown in large sizes and good optical quality. As a result of a three-year intensive characterization campaign of its main properties, we report new and updated physical parameters that are relevant for laser and nonlinear optics applications: lattice phonon vibrational spectra, thermal expansion and thermo-optic coefficients, specific heat at constant pressure, thermal conductivity, piezo-electric and electro-optic coefficients, laser damage thresholds, accurate optical linear dispersion and nonlinear second-order susceptibility coefficients. We provide also a detailed study of the in and out-of-principal plane phase-matching characteristics and associated effective nonlinear coefficients. New experimental results on direct mid-IR (5 - 12  $\mu\text{m}$ ) down-conversion (femtosecond parametric amplification and continuous-wave (cw) difference-frequency generation) pumped by Ti:sapphire laser sources are reported. As main advantages with respect to existing ternary chalcopyrite mid-IR materials,  $\text{LiInS}_2$  displays one of the highest energy bandgaps, a nearly-isotropic thermal expansion behavior, high thermal conductivity associated with high optical damage thresholds, and a nonlinearity and transparency superior to those of the iso-structural  $\text{KTiOPO}_4$ .

PACS numbers: 42.70.Mp; 42.65.Ky, 42.65.Lm, 65.40.Ba, 65.40.De, 78.20.Fm, 78.20.Hp, 78.20.Jq, 78.20.Nv, 78.30.Fs, 61.80.Ba

---

\*Electronic address: jean-jacques.zondy@obspm.fr

†Present address: Department of Molecular Science and Technology, Ajou University, 5 Wonchun-dong, Paldal-gu, 442-749 Suwon, Korea

‡Also at: Laser Research Centre, Quantum Electronics Depart-

---

ment, Vilnius University, LT-2040 Vilnius, Lithuania

## I. INTRODUCTION

The intensive search for new nonlinear materials for the generation of coherent tunable radiation in the mid-IR ( $2 - 20 \mu\text{m}$ ), a spectral range of importance for molecular spectroscopy, atmospheric sensing and various opto-electronic devices, remains a continuing challenge. In contrast with the oxides (with IR transmission range not exceeding  $\sim 5 \mu\text{m}$ ) that attracted much attention lately, such deep mid-IR materials cannot be grown by well mastered and harmless hydrothermal, flux or Czochraski methods. Instead the more complex Bridgman-Stockbarger growth technique [1] in sealed (high atmosphere) ampoules, with volatile and chemically reactive starting components, is the only method used to produce large size single domain crystals, and this certainly hampered their development all the more that special post-growth treatments are needed to restore stoichiometry and improve their optical quality.

To date, only few suitable nonlinear crystals combining an extended transparency from the visible/near-IR to the deep mid-IR and large enough birefringence to allow phase-matching over the whole transparency range are available. The majority of these compounds belong to the ternary chalcogenide semi-conductors of the  $A^I B^{III} C_2^{VI}$  family, where  $A = \text{Cu, Ag}$ ;  $B = \text{Al, Ga, In}$ ;  $C = \text{S, Se, Te}$  [2]. Except for  $\text{AgInS}_2$ , which can exist in both the tetragonal and orthorhombic phases [3], these crystallize in the chalcopyrite ( $\text{CuFeS}_2$ ) structure with  $I\bar{4}2d$  space group and tetragonal symmetry (class)  $\bar{4}2m$  but only few of them possess sufficient birefringence. Most of the commercially available nonlinear crystals ( $\text{AgGaS}_2$  or  $\text{AGS}$ ,  $\text{AgGaSe}_2$  or  $\text{AGSe}$ ,  $\text{ZnGeP}_2$  or  $\text{ZGP}$ ,  $\text{GaSe}$ ,  $\text{CdSe}$ ) or more confidential ones ( $\text{HgGa}_2\text{S}_4$  or  $\text{HGS}$ ,  $\text{Ag}_3\text{AsS}_3$  or proustite,  $\text{Tl}_3\text{AsSe}_3$  or  $\text{TAS}$ ) have their advantages and drawbacks [4, 5]. Despite their higher nonlinearity compared with the oxides, one limitation stems from their low energy bandgap, which prevents the use of pump lasers below  $1 \mu\text{m}$  due to severe linear and two-photon absorption and associated thermal effects.  $\text{ZGP}$  has a high nonlinearity ( $72 \text{ pm/V}$ ) and thermal conductivity but requires pump wavelength above  $2 \mu\text{m}$  due to its residual absorption in the near-IR. The noble metal compounds ( $\text{AGS}$ ,  $\text{AGSe}$ ) have the lowest residual absorption, but their poor thermal conductivity due to low-energy phonon spectrum limits their performance, especially in cw applications [6, 7, 8, 9]. Furthermore, their thermal expansion is anisotropic along the direction parallel and perpendicular to the optic axis, which is a source of thermo-mechanical stresses.  $\text{CdSe}$ 's transparency extends up to  $18 \mu\text{m}$  but its low birefringence and nonlinearity limit its phase-matching capability.  $\text{GaSe}$  is a soft, cleaving compound that cannot be cut at directions different from the optical axis, further its large birefringence results in severe walkoff limitations.

Two new materials belonging to the  $A^I B^{III} C_2^{VI}$  chalcogenide family, where the metal cations are replaced with the lighter alkali metal ( $A = \text{Li}$ ), can now be added to

this limited list:  $\text{LiInS}_2$  or lithium thioindate ( $\text{LIS}$ ) and  $\text{LiInSe}_2$  or lithium selenoindate ( $\text{LISe}$ ). They were shown to crystallize with the  $\beta\text{-NaFeO}_2$  structure (orthorhombic  $\text{Pna}2_1 \equiv C_{2v}^9$  symmetry, point group  $mm2$ ), which is a distorted superstructure of the wurtzite type, as early as 1965 [10]. Hence, contrary to the other mid-IR compounds, these new materials are biaxial and isostructural to, e.g.,  $\text{KTiOPO}_4$  ( $\text{KTP}$ ). The linear and nonlinear properties of  $\text{LIS}$  were briefly studied by Boyd and co-workers in the early 70's, using small and poor quality samples [11], but very few works (mainly focused on its optical bandgap characterization and photoluminescence spectra [12, 13, 14]) have followed since until recently due to problems associated to its reliable growth in large size (up to  $20 \text{ mm}$  in length) allowing to design good optical quality single domain elements for practical applications. These growth problems, associated with the high chemical activity of  $\text{Li}$ , were solved recently [15] and large crystals of high optical quality became available for practical nonlinear optical applications [16, 17, 18]. To our knowledge, there is only one other group which has succeeded previously in synthesizing this material with comparable size [19], but this work was also stopped recently. While only non-phase-matched second-harmonic generation ( $\text{SHG}$ ) was used by Boyd and co-workers to determine the nonlinear properties of  $\text{LIS}$  [11], the first phase-matched  $\text{SHG}$  experiment using the tunable output of a pulsed  $\text{LiNbO}_3\text{-OPO}$  near  $2.5 \mu\text{m}$  was reported only recently [16]. The range of fundamental wavelength was extended to  $6 \mu\text{m}$  using the radiation from a free-electron laser and  $\text{ZGP}$ -frequency doubler [17] and rough estimation of the effective nonlinear coefficients was extracted from those measurements. Direct parametric down-conversion in the range  $4.8 - 9 \mu\text{m}$ , using a femtosecond ( $200 \text{ fs}$ )  $\text{Ti:sapphire}$  amplifier as the pump source, was simultaneously reported with an upper-bound value of the two-photon absorption ( $\text{TPA}$ ) at  $800 \text{ nm}$  of  $\beta = 0.04 \text{ cm/GW}$  [18], owing to the high bandgap energy of  $\text{LIS}$  [13, 19, 20]. Such a value is about 100 times less than the value for  $\text{AGS}$  or 1000 times less than for  $\text{AGSe}$  at  $1.32 \mu\text{m}$  [21], for instance, although some reversible gray-tracking phenomenon occurred due to non-phase-matched blue second-harmonic ( $\text{SH}$ ) at higher pumping (Section XI).

These preliminary experiments allowed to assess the potential of  $\text{LIS}$  over the existing mid-IR materials, and justify the need for a complete characterization of its optical properties. In this paper, we report the main results of an intensive investigation campaign involving a network of laboratories in Europe, on the characterization of the main properties: absorption and thermal capacity (Section III), vibrational (Section IV), thermal expansion and thermo-optic coefficients (Section V), electro-optic and piezo-electric (Section VI), linear optical and thermo-optic dispersions (Section VII), phase-matching predictions (Section VIII), nonlinear coefficients (Section IX), parametric down-conversion (Section X) and optical damage (Section XI) of  $\text{LIS}$  grown (Section II) at

one of the co-authors institute (Design and Technological Institute of Monocrystals or DTIM). Given that LIS is pyro-electric, the paper is concluded by preliminary attempts to invert its macroscopic polarization by use of an external electric field. The preliminary work on LISe has just started and will not be reported here [22].

## II. GROWTH OF LITHIUM THIOINDATE

Single-domain crystals of LIS are grown by the Bridgman-Stockbarger technique in a vertical setup with counter-pressure on seeds along (001) and (010) directions [10, 11, 12, 15, 23, 24, 25]. From the literature the melting point of LIS varies from  $T_{\text{melt}} = 980^\circ\text{C}$  to  $T_{\text{melt}} = 1040^\circ\text{C}$ . The directed crystallization is performed from a melt of elemental Li, In and S, unlike previous reported methods that used Li,  $\text{In}_2\text{S}_3$ , and S [23, 24]. In the melt zone the temperature is maintained at  $\sim 1100\text{ K}$  and decreases to  $\sim 900\text{ K}$  in the growth zone. The phase diagram as well as a representation of the chemical structure of this compound can be found in Ref. [25].

Particular attention is paid to the purity of the starting Li, In and S: these elements are with a nominal purity of 99.999% for S and In, and 99.9% for Li. Sulfur is additionally purified by sublimation in dynamic or static vacuum while metals are cleaned by repeated zonal melting and directed crystallization. A correction of the stoichiometric Li:In:S = 1:1:2 ratios is made taking into account the differing chemical stability of the elements to weight loss during the runs, due to volatilization and interaction between the melt and the container walls. To avoid Li interaction with silica ampoules the synthesis is performed in a special polished graphite crucible located inside a silica ampoule. Some sulfur loss takes place because of its interaction with the graphite walls. The charged ampoules are moved in an optimal thermal gradient of 10 – 15 K/cm at a rate of  $\sim 10\text{ mm/day}$ . This technique allows the growth of crystal ingots with diameters up to 20 mm and lengths up to 50 mm. Although sometimes colorless to a great extent, the as-grown ingots are usually milky because of small inclusions of various phases and it is necessary to anneal them in  $\text{Li}_2\text{S}$  or  $\text{S}_2$  vapor at temperature close to the melting point ( $T_{\text{melt}} \sim 1000^\circ\text{C}$ ) in order to remove the small opaque inclusions [15]. Since the vapor composition and partial pressure of gaseous species are unknown the optimal conditions for obtaining high optical quality elements are empirically found run after run. This empirical technique allows also to adjust the deviation from stoichiometric composition in a narrow, up to  $\pm 1\text{ wt.}\%$ , range of component content. The crystal coloration after the thermal post-growth treatment changes then from almost colorless (or slightly yellow) for as-grown, to salmon-rose tinge depending on the growth and post-growth treatment conditions and chemical composition. Using X-ray diffraction technique parallelipipedic optical elements of a specified orientation relative to the crystallographic axes are cut from the in-

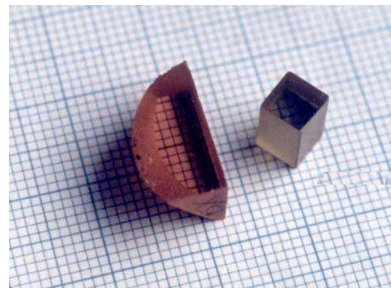


FIG. 1: Photograph of a rose phase (half-moon shaped) and a yellow phase (cubic shaped)  $\text{LiInS}_2$  optical elements.

got (in regions of highest transparency). The optical elements with aperture up to  $1\text{ cm}^2$  and length up to 15 mm are then polished for optical measurements or for nonlinear frequency conversion (Fig. 1).

### A. Composition, structural and luminescence properties

Precise chemical analysis - using differential dissolution techniques (DDT) and inductively-coupled plasma (ICP) method - shows that the composition of colorless (or yellow tinge) and rose samples is  $\text{Li}_{0.98}\text{In}_{1.03}\text{S}_{2.00}$  ( $\text{Li}_{0.96}\text{In}_{1.06}\text{S}_{1.98}$ ) and  $\text{Li}_{0.86}\text{In}_{1.04}\text{S}_{1.98}$  respectively [15]. Lithium deficit ( $N_{\text{Li}} : N_{\text{In}} < 1$ ) is observed for all samples, the annealed rose ones being characterized by a higher sulfur content ( $N_{\text{Li+In}} : N_{\text{S}} < 1$ ). The band-structure nature of LIS has been confirmed to be of the *direct* type (direct transitions between parabolic bands) [13]. The forbidden band gap values estimated by us ( $E_g = 3.72$  and  $3.57\text{ eV}$  at 80K and 300K, respectively, which are in good agreement with previous measurements [13, 19, 20]), the position of the long-wave edge of transparency ( $13\mu\text{m}$  at an absorption of  $6\text{ cm}^{-1}$ ) and the crystal symmetry group were found identical for all crystal colorations although small variations in lattice parameters due to point defects were also observed [26].

A detailed and general structural analysis of  $\text{A}^{\text{I}}\text{B}^{\text{III}}\text{C}_2^{\text{VI}}$  compounds, where  $\text{A}^{\text{I}}$  is an alkali metal such as Li, has been given by Kish *et al* [27]. Compared to the denser chalcopyrite structure of AGS or AGSe [28], the  $\beta\text{-NaFeO}_2$  structure of Li-chalcogenides allows the presence of empty cavities within the unit cell volume (see Fig.1 in Ref. [29] for instance for the unit cell representation). The value of the orthorhombic lattice parameters are  $a = 6.874(1)\text{ \AA}$ ,  $b = 8.033(2)\text{ \AA}$ ,  $c = 6.462(1)\text{ \AA}$  for as-grown colorless LIS, and  $a = 6.890(1)\text{ \AA}$ ,  $b = 8.053(1)\text{ \AA}$ ,  $c = 6.478(1)\text{ \AA}$  for slightly yellowish samples. They are slightly lower than the values reported by Hoppe [10] and Boyd *et al* [11] or Kamijoh *et al* [12] and Kish *et al* [30], but most closely to the last one. They modify to  $a = 6.896(1)\text{ \AA}$ ,  $b = 8.058(2)\text{ \AA}$ ,  $c = 6.484(4)\text{ \AA}$  for rose annealed samples. Concomitantly, the density changes from  $\rho = 3.52\text{ g/cm}^3$  to  $\rho = 3.44\text{ g/cm}^3$ . We have cho-

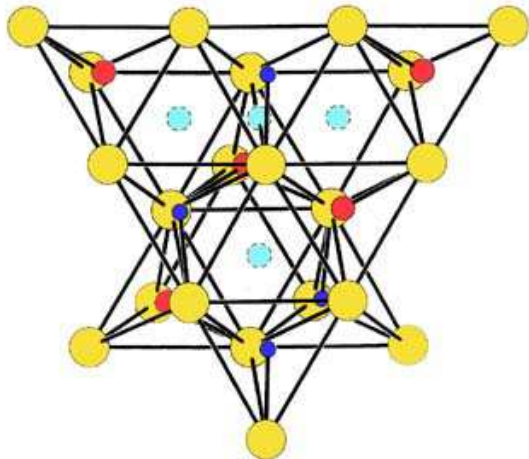


FIG. 2: Fragment of the orthorhombic unit cell structure: large grey circle,  $S^{2-}$ ; medium dark circle,  $In^{3+}$ ; small dark circle,  $Li^+$ . The 3 empty areas materialized with dotted circles indicate the location of tetra-pores.

sen  $c < a < b$  where  $c$  is the polar two-fold axis which coincides with the selection of Boyd *et al* [11]. This convention satisfies the recommendation of Roberts [31] for unique designation of the orthorhombic class  $mm2$ .

A fragment of the structure of LIS is shown in Fig. 2. It is formed by  $LiS_4$  and  $InS_4$  tetrahedrons. The  $S^{2-}$  ions are arranged in hexagonal packing with tetragonal and octahedral cavities (tetra- and octapores) [27]. Two types of point defects can be assessed from the structural analysis: lithium and sulfur vacancies ( $V_{Li}$ ,  $V_S$ ) in as-grown samples, some of which recombine with Li, S at annealing in  $S_2$  and  $Li_2S$  vapor, and anti-site  $In_{Li}$  defects which are expected to be present in all samples. Formation of the latter is possible thanks to close values of cation tetrahedral radii as  $R(Li^+)_4 = 0.59\text{\AA}$  and  $R(In^{3+})_4 = 0.66\text{\AA}$ . The  $V_S$  defects give rise to a strong absorption band at 363nm, whereas an intense broadband blue luminescence at 420-480nm, observed for most of the crystals, is related to donor ( $In_{Li}$ )-valence band transition [13, 15]. The 585nm luminescence in samples annealed in  $S_2$  vapor, is associated with donor ( $In_{Li}$ )-acceptor ( $V_{Li}$ ) transitions. From the energy level diagram it follows that the energy level, relating to  $In_{Li}$  would be located at about 120 meV above that of  $V_S$  [12].

### B. Rare-earth doping of lithium thioindate

The less dense  $\beta$ - $NaFeO_2$  structure allows in particular doping with rare-earth (RE) active ions which can be hosted inside the octapores. Such a preliminary doping experiment with  $Nd^{3+}$  ions was previously reported with the aim of investigating RE:LIS potential as a self

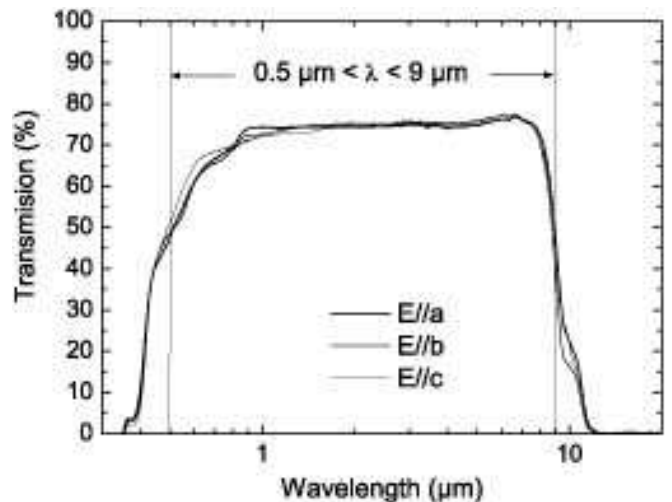


FIG. 3: Polarized transmission spectra of an annealed LIS sample (thickness 5 mm), not corrected for the Fresnel loss.

down-converting material [32]. Sulfides are chemically more stable than halogenides (such as  $KPb_2Cl_5$  [33]) and they can be used as hosts for laser action up to 6 microns, all the more advantageous since the phonon vibration spectrum of LIS is restricted to phonon energies  $\hbar\omega_{max} < 400\text{ cm}^{-1}$  (see Section IV). The dopant was added as  $Nd_2S_3$  during the growth process. The segregation coefficient was estimated to be about 0.02, and the Nd concentration inside the crystal was determined to be only  $\sim 0.06\text{ wt.}\%$  using spectral analysis with an etalon. The RE doping hampered considerably the crystal growth, since the Nd:LIS as-grown ingots were only  $5 \times 5 \times 5\text{ mm}^3$  in size and much darker than for pure LIS. The optical spectroscopy of the doped crystals confirmed the presence of  $Nd^{3+}$  active ions, both in absorption (presence of a set of weak lines centered at 760, 820 and 900 nm corresponding to electronic transitions from the ground state  $^4I_{9/2}$  to manifolds as ( $^4S_{3/2} + ^4F_{7/2}$ ), ( $^2H_{9/2} + ^4F_{5/2}$ ) and  $^4F_{3/2}$  in  $Nd^{3+}$ ) and in luminescence (40-nm broad emission centered at 1080 nm and corresponding to the  $^4F_{3/2} \rightarrow ^4I_{11/2}$  lasing transition) [16, 32]. Nd doping was found to stimulate by one order of magnitude the blue photo-luminescence of pure crystals, meaning that doping favors the formation of interstitial and anti-site indium defects ( $In_{Li}$ ). From the intensity of the absorption lines, a  $Nd^{3+}$  absorption cross-section of  $\sigma_{abs} \sim 2 \times 10^{-20}\text{ cm}^2$  has been inferred, roughly 3 times lower than the value in YAG [34].

### III. RESIDUAL ABSORPTION AND SPECIFIC HEAT OF LIS

Fig. 3 shows the polarized transmission spectra of a thick ( $L = 5\text{ mm}$ ) annealed optical element. The 350-800nm range was recorded with a Perkin Elmer Lambda 900 spectrophotometer and the infrared part

recorded with a Fourier-Transform rapid-scan Interferometer (BRUKER IFS 113V FTIR spectrometer). The transmission has not been corrected for the Fresnel loss at the input/output polished facets. Depending on the growth and annealing conditions, some absorption bands due to the various point defects - in particular excess sulfur ions occupying interstitial sites - may limit the transmission window in the visible side. These visible bands, responsible of the rose coloration of the annealed samples, restrict the genuine  $T \sim 70\%$  transmission range to  $0.8 - 8.1\mu\text{m}$ . The post-growth thermal treatment, however, improves considerably the transparency within the above window. At  $T \geq 50\%$ , the useful range for cw applications with  $L \geq 5\text{mm}$  is extended from  $0.5\mu\text{m}$  to  $8.9\mu\text{m}$ . In high power femtosecond parametric amplification (as in cw DFG) idler generation almost up to the zero IR transmission level ( $12\mu\text{m}$ ) will be reported in Section X. The absorption coefficient  $\alpha(\lambda)$  within the full transparency window deduced from the FTIR spectra amounts to  $0.1 - 0.15\text{cm}^{-1}$ . These values are overestimated as we shall see below. To obtain a reliable value, the residual loss within the clear transmission window was also directly measured using various laser sources on annealed thick samples ( $L \sim 5\text{mm}$ ) and the derived coefficients  $\alpha(\lambda)$  are confronted to the result of laser calorimetry measurement of absorptances.

#### A. Residual absorption loss: laser line and calorimetric measurements

Two rose parallelepipedic optically polished samples A1 (dimensions  $4 \times 5 \times 5\text{mm}^3$ , cut at  $66^\circ$  from the  $a$  crystallographic axis for propagation in the  $a - b$  plane) and A2 (dimension  $5 \times 5 \times 5\text{mm}^3$ , cut at  $28^\circ$  from the  $c$  crystallographic axis for propagation in the  $a - c$  plane) were used for absorptance measurements. Laser-line measurements were performed using several extended-cavity AlGaAs and InGaAsP diode lasers at  $\lambda = 0.780, 0.843$  and  $1.265\mu\text{m}$  delivering  $\sim 3\text{mW}$  of cw power, a cw extended-cavity InGaAsP diode laser ( $\lambda = 1.550\mu\text{m}$ ) and the  $2.53\mu\text{m}$  idler output from a periodically-poled LiNbO<sub>3</sub> (PPLN) cw OPO [35]. The laser beam was focused to a small waist of  $\sim 100\mu\text{m}$  in order to scan the sample aperture area and to avoid some etalon effect arising from multiple interference when a parallel beam is used (the samples were slightly tilted from normal incidence). The direction of polarization of the laser sources were set parallel to  $c$  or perpendicular (lying in the  $a - b$  plane) for sample A1 and parallel to  $b$  or perpendicular (lying in the  $a - c$  plane) for sample A2. The short term (1 s) power stability of all laser sources was better than  $\pm 1\%$ . A sensitive photodiode connected to a trans-impedance preamplifier was used to detect the light. To enhance the measurement sensitivity, all transmittance was measured using a differential technique, by nulling first the incoming power using a reference voltage and measuring the small imbalance voltage once the sample is introduced in

TABLE I: Absorption coefficients of annealed LIS samples (A1 and A2), each with  $L = 5\text{mm}$ , measured at several laser lines. E denotes the direction of the laser electric field. All coefficients are in  $\text{cm}^{-1}$  ( $\pm 20\%$ ).

Wavelength (nm)	A1 sample		A2 sample	
	$\alpha$ (E//c)	$\alpha$ (E//a - b)	$\alpha$ (E//b)	$\alpha$ (E//a - c)
780	0.049	0.066	0.199	0.110
843	0.025	0.144	0.232	0.170
1265 <sup>a</sup>	0.089	0.075	0.124	0.049
1550	-	-	0.144	0.085
2530	0.055	0.051	0.045	0.050

<sup>a</sup>Unfocused beam with 1 mm diameter.

the beam path. The Fresnel reflected power from each facet (with ideal reflectivity  $R = [(n - 1)/(n + 1)]^2$ ) was also carefully measured and subtracted to the imbalance voltage, and the absorptance  $A = 1 - \exp(-\alpha L)$  (where  $L = 5\text{mm}$  is the sample length) calculated from the net transmittance  $T = (1 - R_1)(1 - R_2)(1 - A)$ , where  $R_{1,2}$  are the measured input and output facets reflectivity. Only the transmittance of the primary refracted beam was measured (secondary refracted spots blocked). The uncertainty in  $\alpha(\lambda)$  is estimated to be  $\pm 20\%$ . The results of the measurements, reported in Table I, show some significant scatter but indicate an average absorption loss coefficient of  $\langle \alpha \rangle = (0.05 \pm 0.004)\text{cm}^{-1}$  for the longest wavelength ( $\lambda = 2.53\mu\text{m}$ ) lying well inside the clear transparency region. However, the amount of scatter loss, as compared to genuine absorption loss, cannot be assessed with laser transmission measurements.

Hence calorimetric absorptance measurements were performed on sample A2, to derive a more accurate value of  $\alpha$  from the absorptance  $A$ , using the formula

$$A = \frac{m C_{th} \Delta T}{P t_B} \quad (1)$$

where  $m = 0.438\text{g}$  is the measured mass of sample A2,  $P$  is the laser power,  $t_B$  the irradiation time,  $C_{th}$  (in unit of  $\text{J/kg/K}$ ) is the thermal capacity of the sample and  $\Delta T$  is the temperature rise of the sample due to the heat deposited. The absorptance measurements were performed according to the International Standard ISO11551 (Test method for absorptance of optical components) which defines the procedures and techniques for obtaining comparable values for the absorptance of optical components. In these procedures, the assumption is made that the absorptance of the test sample is constant within the temperature fluctuations experienced by the component during the measurement, constant within the volume of the component (which was inferred from the previous transmittance measurement with focused laser beam) and independent of the power density of the impinging radiation.

The core of the laser calorimeter set-up (Fig. 4), is made of a thermally isolated camera (TIC) in which

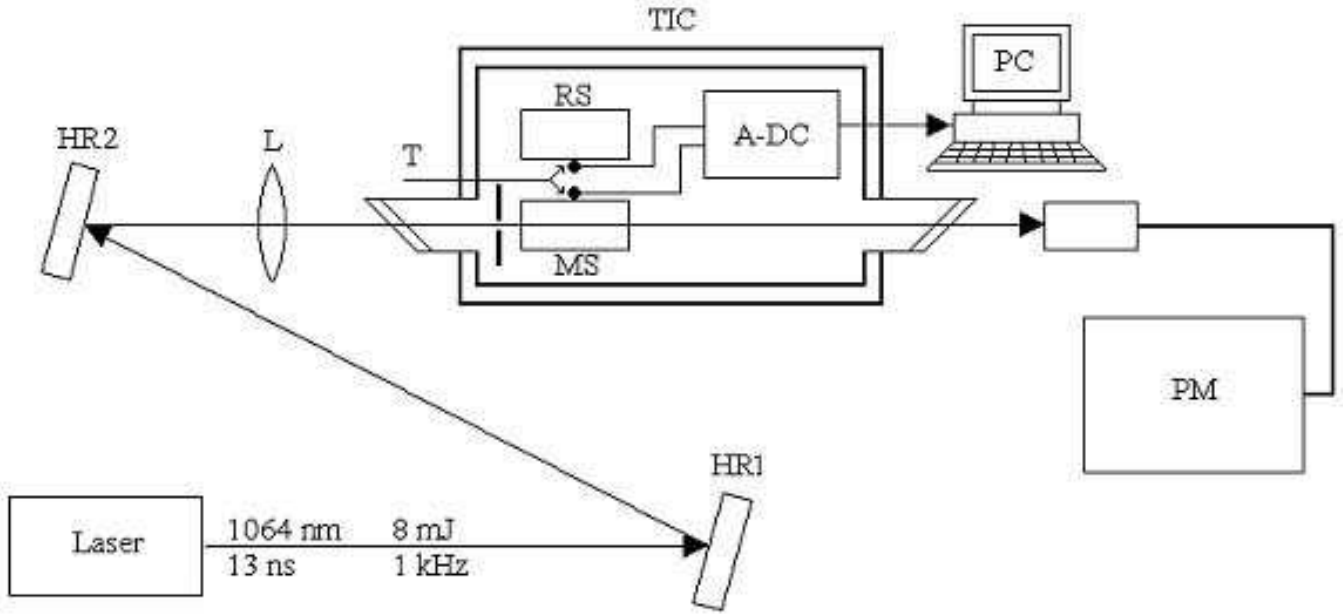


FIG. 4: Calorimetric setup for absorbance measurements (HR-high reflectivity mirrors, L-lens, MS-measured sample, RS-reference sample, T-thermistor, A-DC-analogo-digital converter, PM-power meter, PC-personal computer).

the measured (MS) and a reference sample (RS) were mounted. The laser radiation passed only through the tested sample, the reference sample being used to monitor the temperature changes caused by room air temperature fluctuations within the TIC. Both MS and RS samples were mounted on special holders ensuring a good thermal contact between the calibrated thermal sensor (small bead thermistor) and the samples. A linearly polarized, diode-pumped Q-switched (1kHz repetition rate, 13ns pulse-width) Nd:YAG laser was focused to a  $\sim 1$ mm spot diameter onto the LIS sample (MS). The average power was limited to  $< 1.6$ W to avoid possible damage (pulse energy  $< 1.6$ mJ corresponding to an energy density of  $\sim 0.2$  J/cm<sup>2</sup> and intensity of 15MW/cm<sup>2</sup>). To ensure that reflected or stray light will not strike the holder and thermistor, the beam path in front of the RS sample was apertured with a 1.2mm diameter diaphragm. The irradiation time was selected in the range between 30s and 180s according to the requirement of ISO 11551 for pulsed method. The temperature of the MS thermistor was digitized by an analog-to-digital converter (A-DC) and recorded versus time by a computer (PC), for various impinging powers.

Fig. 5 displays a typical temperature plot obtained for  $P = 1$ W and a polarization along the  $c$  axis. The rising part corresponds to the irradiation time window  $t_B = 70$ s. To evaluate the temperature change  $\Delta T$  following irradiation (according to the ISO 11551 standard), one has to extrapolate the exponentially decaying part of the plot to a time  $t = t_0 + t_B/2$ , where  $t_0$  is the starting irradiation time. The absorbance value for a laser polarization along  $c$  axis,  $A_c$ , or perpendicular (in the  $a-b$  plane)  $A_{a-b}$  was deduced as the average of measurements

with several impinging power. Using the value determined further for  $C_{th}$  ( $= 535$  J/kg/K, see below), one finds  $A_c = 0.019(\pm 0.0005)$  and  $A_{a-b} = 0.0205(\pm 0.0005)$ , leading to residual absorption values  $\alpha_c = 0.0384$  cm<sup>-1</sup> and  $\alpha_{a-b} = 0.0414$  cm<sup>-1</sup> at 1064nm. These values are slightly lower than the values determined from laser line transmission, meaning that absorption loss dominates over scattering loss in the annealed samples. Further improvements in the growth and post-growth treatments, aimed at the reduction of point defects, are needed to bring down the residual loss to the level of  $\sim 0.01$  cm<sup>-1</sup> which is the best result obtained for AGS [8, 9, 28, 36].

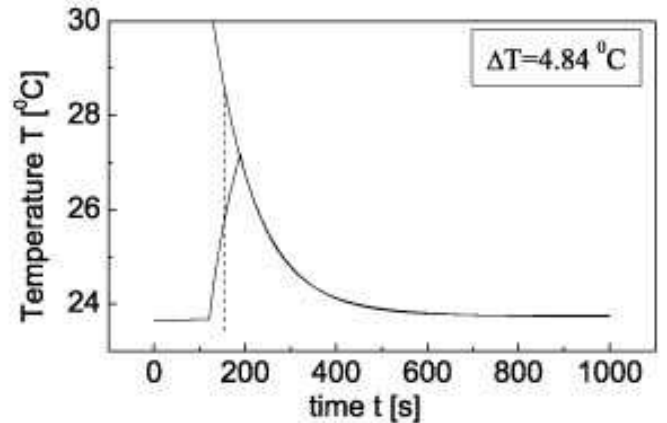


FIG. 5: Dynamics of the temperature change of sample A1, for a laser power  $P = 1$  W and polarization along  $c$ -axis and irradiation time  $t_B = 70$ s.  $\Delta T$  is given by the height of the dashed vertical segment lying in the middle of the irradiation window.

## B. Specific heat at constant pressure

To use relation (1), the thermal capacity  $C_{th}$  had to be measured. This quantity is linked to the molar heat capacity (or *specific heat*) at constant pressure,  $C_p(T) = (\Delta Q/\Delta T)_p$  (in units of J/mol/K), by  $C_{th} = C_p/M$  where  $M = 185.88 \times 10^{-3}$  kg is the molar mass of LIS. By definition, the molar specific heat is the amount of energy  $\Delta Q$  required to raise the temperature of one mole of material by  $\Delta T = 1$  K. By the time these measurements were performed, no published data on  $C_p$  were available to us hence we had to measure  $C_{th}$  using a specially built small calorimeter with known mass and thermal capacity. These latter parameters were further checked by measuring the well known thermal capacity of a few reference materials (KDP, LiNbO<sub>3</sub> and BK7 glass). Such a calibration allowed to estimate some constants of the calorimeter, such as thermal losses. Once the mass and thermal capacity of the calorimeter accurately determined, the A2 sample was heated to  $T = 35^\circ\text{C}$  inside an oven with precisely regulated temperature (temperature fluctuation  $< 0.1$  K), and inserted into the calorimeter with initial temperature of  $\sim 25^\circ\text{C}$ . The dynamics of temperature changes of the calorimeter was monitored with the same thermistor and data acquisition software as used for the absorptance measurement. From the measured ( $\Delta T \sim 0.4^\circ\text{C}$ ) temperature rise and the mass of sample A2, we determined a value of  $C_{th} = 535 (\pm 25)$  J/kg/K. Using the molar mass value  $M$ , the deduced molar specific heat at constant pressure of LIS is  $C_p(T = 308\text{K}) = 99.4 (\pm 5)$  J/mol/K.

It is interesting to compare this value with the results of  $C_p(T)$  measurements by Kühn *et al* on polycrystalline LIS material [37]. The general theoretical expression of  $C_p(T)$  for anharmonic solids is

$$C_p(T) = 12R \left[ F(x_D) + \sum_{k=1}^N c_k T^k \right] \quad (2)$$

where  $R$  is the molar mass constant,  $x_D = T_D/T$  ( $T_D$  is the Debye temperature) and  $F(x_D)$  is the Debye function describing the temperature dependence in the harmonic lattice vibration approximation,

$$F(x_D) = \frac{3}{x_D^3} \int_0^{x_D} \frac{x^4 e^x dx}{(e^x - 1)^2}. \quad (3)$$

The value of  $N$  and the absolute magnitudes of the coefficients  $c_k$  in the sum expansion in (2) can be considered as a measure of the degree of lattice anharmonicity, while the sign of  $c_k$  is essentially determined by the shape of the interatomic potential. In Eq. (2), the leading coefficients  $c_1$  and  $c_3$  were found negative for all A<sup>I</sup>B<sup>III</sup>C<sub>2</sub><sup>VI</sup> chalcogenide compounds, and the magnitude of  $c_k$  was found  $\sim 10$  times higher and independent of the anion C<sup>2-</sup> for Li-compounds. This means that the anharmonic contribution of the lattice potential energy is much stronger in LiInC<sub>2</sub><sup>VI</sup> compounds ( $N = 4$  in Eq. 2) than in A<sup>I</sup>B<sup>III</sup>C<sub>2</sub><sup>VI</sup>

chalcopyrite compounds ( $N = 3$ ). In LIS, this is related to the specific nature of the Li-S bond, which is about twice weaker than the In-S bond [38]. As a consequence, the temperature dependence of  $C_p(\text{LIS})$  is much weaker than for AgInS<sub>2</sub> and AGSe [39], and the resulting  $C_p(T)$  values for LIS are the lowest of all chalcogenides. Our value,  $C_p(T = 308\text{K}) = 99.4 (\pm 5)$  J/mol/K, measured on a large size single crystal is very close to the upper bound theoretical value of  $C_p(T \rightarrow \infty) = 12R = 99.77$  J/mol/K, but slightly above the value measured by Kühn *et al* on polycrystalline LIS ( $C_p(\sim 310\text{K}) = 92$  J/mol/K, assuming that  $T_D = 310(\pm 50)$  K [37]). Our value is almost identical to the specific heat at room temperature of AgInS<sub>2</sub> (96 J/mol/K) and AGSe (99.8 J/mol/K) [39]. The specific nature of the Li-S bond will be also apparent in the thermal expansion behavior of LIS (see Subsection V A).

## IV. VIBRATIONAL PROPERTIES

The vibrational properties have been investigated by means of Raman spectroscopy and infrared reflectivity in polarized light at room temperature. The group theory analysis shows that, at the zone centre for the  $\beta$ -NaFeO<sub>2</sub> structure, the 48 normal phonon modes are distributed among the various irreducible representations of the C<sub>2v</sub><sup>9</sup> factor group as follows:

$$\Gamma^{vib} = 12A_1 + 12A_2 + 12B_1 + 12B_2. \quad (4)$$

The three acoustic phonon modes have A<sub>1</sub>, B<sub>1</sub> and B<sub>2</sub> symmetries; the 45 remaining (optical) modes are Raman-active. A<sub>1</sub> modes will be active when the experimental configuration selects a diagonal *aa*, *bb* or *cc* component of the Raman tensor, while the selection of *ba*, *ca* and *cb* components will respectively allow the observation of the optical phonons of A<sub>2</sub>, B<sub>1</sub> and B<sub>2</sub> symmetry. A<sub>2</sub>-type phonons being infrared inactive, the IR-reflectivity spectra should then contain 11 polar modes of each A<sub>1</sub>, B<sub>1</sub> and B<sub>2</sub> symmetries, with dipole moment respectively parallel to *c*, *a* and *b* crystallographic axes. In theory, every optical phonon may then be observed by means of IR-reflectivity and/or Raman-scattering. Nonetheless, depending on various factors such as the more or less polar character of bonds, even an active mode may be unobservable.

To obtain results on every phonon type, we used two LIS rose-tinge samples cut from the same ingot, with sizes  $4 \times 4 \times 5$  mm<sup>3</sup> and parallel optically polished facets (4x4 mm<sup>2</sup>) normal to *a* and *c* axes. Infrared reflection spectra were recorded in the spectral range 18.3 - 600 cm<sup>-1</sup> with the FTIR interferometer (BRUKER IFS 113V), and this whole range of data was used to adjust the parameters of the dielectric permittivity model shown in Eq.(5). The experimental spectra, recorded at quasi-normal incidence (at an angle of incidence of 6°) with an electric field polarisation parallel to *a*, *b* and *c* axes, are shown in Fig. 6 (symbols). As can be seen from these graphs, each

reflectivity spectrum is rather complex and exhibits several more or less overlapping bands, and the high-energy band(s) in each polarization generally show some additional structure (slight inflexion in the band shape) that suggests, in addition to a strong mode, the presence of several other modes contributing to the same band. Actually, from the numerical analysis of the experimental results, it is found that for each direction of polarization, there are three polar modes in the high frequency band (350 - 420  $\text{cm}^{-1}$ ) and medium frequency band (250-350  $\text{cm}^{-1}$ ) and the remaining five polar modes, not all observable in Fig. 6, are in the low frequency region ( $< 250 \text{ cm}^{-1}$ )

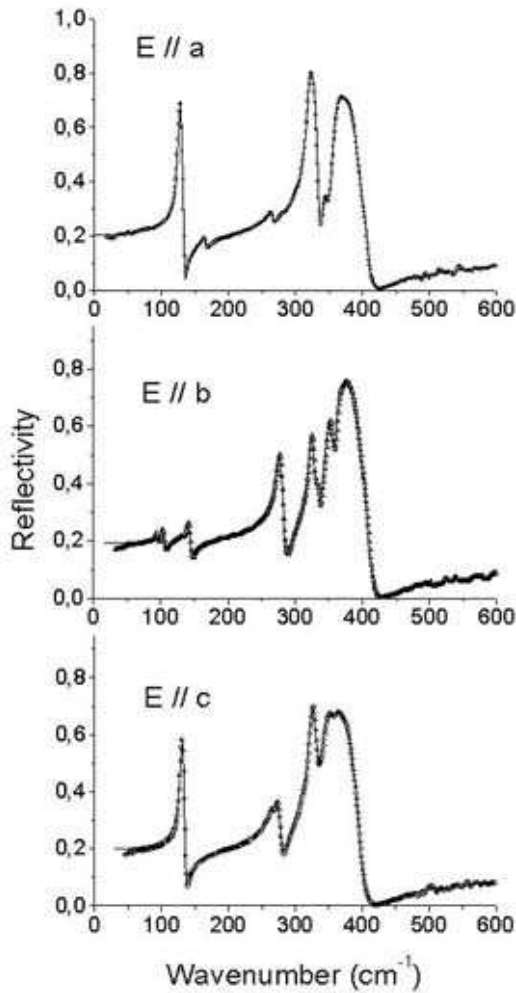


FIG. 6: Infrared reflection curves (symbols) recorded with polarized light with an electric field parallel to the crystallographic axes *a* - B<sub>1</sub> modes -, *b* - B<sub>2</sub> modes - and *c* - A<sub>1</sub> modes. The continuous lines represent in each case the best-fit reflectivity curves calculated with the model in Eqs.(5)-(6).

Polarized micro-Raman experiments were performed using a Jobin-Yvon T64000 Raman spectrometer equipped with a confocal microscope and a liquid-N<sub>2</sub> cooled CCD detector. Raman spectra were recorded at

room temperature in the region 12 - 600  $\text{cm}^{-1}$  in triple subtractive configuration with an 1800 gr/mm grating. To increase the quality and resolution of the spectra, we chose to use the 647nm red line of an argon-krypton laser (P=100 mW) which experiences lower absorption loss than a green laser [40]. To avoid possible influence of surface defects, the confocal microscope focused the laser beam at a depth of 60  $\mu\text{m}$  under the surface. A scattering geometry will be described by the notation  $e_1(p_1p_2)e_2$  [41] where  $e_i$  identifies the propagation direction of the laser light, polarized along  $p_i$ ,  $e$  and  $p$  being *a*, *b* or *c* crystallographic axes; the subscripts  $i = 1$  and 2 refer to incident and scattered beams respectively. A polarizer and a half-wave plate were used to select the different components of the crystalline Raman tensor  $b(aa)b$ ,  $c(bb)c$ ,  $b(cc)b$ ,  $c(ba)c$ ,  $b(ca)b$  and  $a(cb)a$  that correspond to A<sub>1</sub> (the first three), A<sub>2</sub>, B<sub>1</sub> and B<sub>2</sub> symmetries respectively. Fig. 7 shows some of the experimental spectra. The Raman spectra are dominated by a strong mode of A<sub>1</sub> symmetry at  $\sim 268 \text{ cm}^{-1}$ , also apparent in the IR reflectivity spectra for E//*b* and E//*c*.

Due to the respective mass of the atoms, high (low) frequency modes obviously imply movements of Li-S (In-S) bonds. Phonons of medium frequency (250-350  $\text{cm}^{-1}$ ), visible in both IR-reflectivity and Raman scattering, are attributed to In-S bonds [20] while those of highest frequency (above 350  $\text{cm}^{-1}$ , Fig. 6) that give rise to strong IR bands but no observable Raman line are due to weaker Li-S bonds [38]. Polar modes TO $\approx$ LO splitting observed in the infrared measurements for any of the explored polarizations is rather important in the high frequency region (strong IR-bands) which attests for a high polar (ionicity) character of Li-S bonds in this crystal. The splitting decreases with the phonon frequency to become so small for low frequency modes that no corresponding band appears in the reflectivity spectrum which indicates a mostly covalent character of the In-S bonds. However, even if a phonon cannot be observed by means of IR-reflectivity, its Raman activity may be high, which is the case for modes lying below 100  $\text{cm}^{-1}$ . Actually intense Raman lines appear in the low and mid-frequency region, when almost no line can be detected above roughly 350  $\text{cm}^{-1}$ . In order to fit the experimental IR-reflectivity spectra, and get the best-fit reflectivity curves (lines in Figure 6, in a good agreement with experimental points) we used the so-called *four-parameter model*, convenient to represent even asymmetrical and wide bands [42]. This model expands the factorized form of the dielectric permittivity function as

$$\epsilon(\omega) = \epsilon' - i\epsilon'' = \epsilon_\infty \prod_{j=1}^N \frac{\Omega_{j,LO}^2 - \omega^2 + i\gamma_{j,LO}\omega}{\Omega_{j,TO}^2 - \omega^2 + i\gamma_{j,TO}\omega} \quad (5)$$

to fit a reflectivity curve described by the Fresnel formula

$$R(\omega) = \left| \frac{\sqrt{\epsilon(\omega)} - 1}{\sqrt{\epsilon(\omega)} + 1} \right|^2. \quad (6)$$

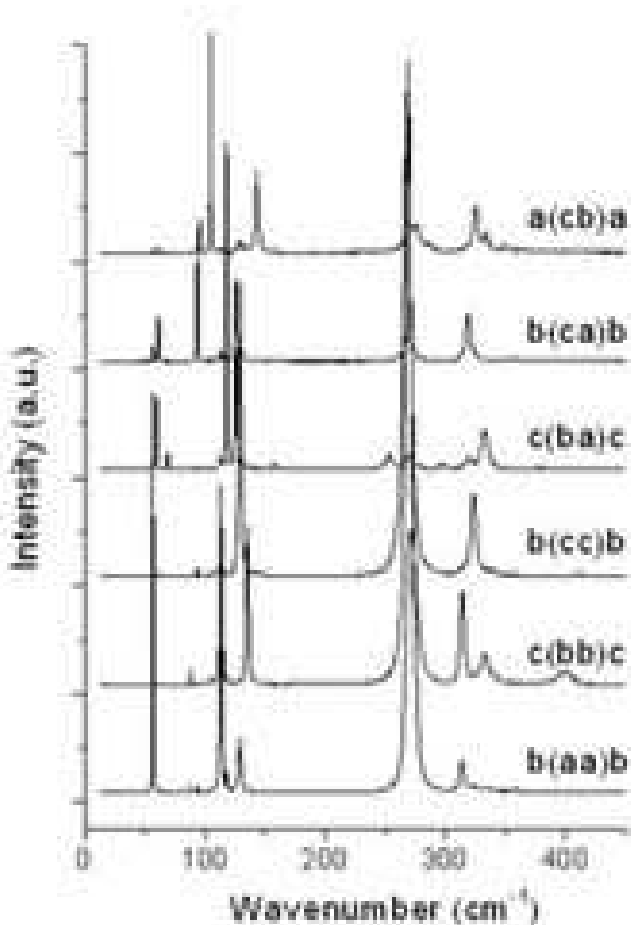


FIG. 7: Polarized Raman spectra (shifted for reasons of clarity) recorded at room temperature. The experimental configurations  $b(aa)b$ ,  $c(bb)c$ ,  $b(cc)b$  correspond to  $A_1$  modes,  $c(ba)c$  to  $A_2$  modes,  $b(ca)b$  to  $B_1$  modes and  $a(cb)a$  to  $B_2$  modes. A few peaks in each spectrum have been attributed to an interference of an intense line active in another geometry.

In the  $\beta$ - $\text{NaFeO}_2$  structure, the model implies for a given polarization  $N$  damped oscillators, the number  $N$  being at most equal to 11 (number of theoretically observable modes, predicted in this structure by group theory analysis). The  $j$ -th damped oscillator represents the  $j$ -th observed infrared active couple of modes, characterized by four adjustable parameters, namely the longitudinal  $\Omega_{j,\text{LO}}$  and transverse  $\Omega_{j,\text{TO}}$  angular frequencies, and the corresponding damping frequencies  $\gamma_{j,\text{LO}}$  and  $\gamma_{j,\text{TO}}$ . The high-frequency limit values of the dielectric constant is also adjusted to yield  $\varepsilon_\infty(A_1)=3.99$ ,  $\varepsilon_\infty(B_1)=4.09$ ,  $\varepsilon_\infty(B_2)=3.97$ .

Table II lists the wavenumbers  $\bar{\nu}_j = \Omega_j/2\pi c$  and damping rates  $\bar{\gamma}_j = \gamma_j/2\pi c$  (expressed in  $\text{cm}^{-1}$ ) of the observed optical phonons deduced from IR-reflectivity and/or Raman scattering experiments, assigned to the various irreducible representations of the  $C_{2v}^9$  factor group. These data allow to compute the linear dielectric properties of LIS in the far-IR range, using Eq.(5). Typically, TO and

LO frequencies deduced from IR-reflectivity experiments are determined to better than  $1 \text{ cm}^{-1}$ . The precision of a Raman-active phonon frequency is also generally better than  $1 \text{ cm}^{-1}$ , except for broad and low-intensity lines for which it decreases to  $2 \text{ cm}^{-1}$ . The transverse or longitudinal character of the Raman-active modes for  $A_1$ ,  $B_1$  and  $B_2$  symmetries has been determined with the help of the IR reflectivity results where this TO or LO character is immediate. Non-observed IR-active modes indicate a small  $\text{TO} \approx \text{LO}$  splitting and generally did not allow an accurate determination of TO and LO frequencies from Raman spectra, but only of a mean value labelled by  $\text{TO} \approx \text{LO}$ . A few Raman lines have been attributed to an interference by an intense line active in another geometry. Taking into account the different conventions adopted by authors to label crystallographic axes (and modes symmetry), these results complement those from previous studies performed with unpolarized light [20, 38, 43].

The accurate determination of the frequencies in Table II allows to estimate the interatomic bonding force constants in LIS, using the theoretical considerations developed by Neumann about the correlation between the vibrational modes of compounds with sphalerite, chalcopyrite and  $\beta$ - $\text{NaFeO}_2$  structures [44]. According to this model the vibrational spectrum of a crystal with  $\beta$ - $\text{NaFeO}_2$  structure contains two sphalerite-like modes the TO-frequencies of which are nearly independent on the polarization direction. Further, one of these sphalerite-like modes always corresponds to the highest  $\bar{\nu}_{\text{TO}}$  frequency found in the IR reflectivity spectra. If the interaction between the atoms is restricted to next-nearest neighbors which is justified by the high bond ionicities in Li-containing ternary compounds, the wavenumbers of the transverse optical modes of these sphalerite-like modes in  $\text{LiB}^{\text{III}}\text{C}_2^{\text{VI}}$  are given by [45]

$$\bar{\nu}_{\text{TO},k}^2 = \frac{1}{\pi^2 c^2} (\alpha_k - \delta\alpha_k) \left( \frac{1}{m_k} + \frac{1}{m_C} \right) \quad (7)$$

with  $k = \text{Li, B (=In)}$ . Here  $c$  is the speed of light,  $\alpha_k$  the mechanical bond-stretching force constant,  $m_k$  the mass of the cation and  $m_C$  the mass on the chalcogen anion ( $\text{C}=\text{S}^{2-}$ ). The quantity  $\delta\alpha_k$  accounts for the fact that in the case of IR active modes the local atomic displacements give rise to a non-vanishing net dipole moment per unit cell and thus, to additional dipole-dipole interactions. It is given by  $\delta\alpha_k = \sqrt{3}(e_k)^2/(16\varepsilon_0 s_k^3)$ , where  $s_k$  is the average bond length ( $s_{\text{Li-S}} = 0.2438 \text{ nm}$ ,  $s_{\text{In-S}} = 0.2452 \text{ nm}$ ),  $e_k = 0.28ef_k(Z_k + Z_C)$  is an effective charge depending on the bond ionicity  $f_k$  and the valences of the cation and anion participating to the bond. In Ref. [38], from an unpolarized IR reflectivity spectrum of polycrystalline LIS restricted to the region  $200 - 400 \text{ cm}^{-1}$ , the highest-frequency TO/LO mode identified corresponds to  $356/406 \text{ cm}^{-1}$  and the second TO/LO sphalerite-like mode to  $323/334 \text{ cm}^{-1}$ . Actually from the inspection of Table II, the highest-frequency sphalerite-like modes with nearly identical frequencies in  $B_1$  and  $B_2$  symmetries are respectively the  $400.4/408.6$

TABLE II: Zone-center phonon wavenumbers ( $\bar{\nu}_{\text{TO}}/\bar{\nu}_{\text{LO}}$ ) and damping ( $\bar{\gamma}_{\text{TO}}/\bar{\gamma}_{\text{LO}}$ ), in  $\text{cm}^{-1}$ , deduced from IR reflectivity and Raman scattering experiments at room temperature for the various symmetry-adapted polarization configurations. The transverse (TO) and/or longitudinal (LO) character of the observed Raman-active phonons have been determined with the help of the IR reflectivity results (the notation TO+LO means that the splitting is too weak to be unambiguously identified).

Phonon symmetry	IR reflectivity		Raman scattering
	Wavenumbers $\bar{\nu}_j$	Dampings $\bar{\gamma}_j$	
A <sub>1</sub> TO/LO (cm <sup>-1</sup> )	-/-	-/-	56.4 (TO≈LO)
	-/-	-/-	88.1 (TO≈LO)
	-/-	-/-	112.7/113.3
	128.6/138.2	3.0/4.4	129.1/135.2
	266.0/267.1	8.5/8.7	268/269
	274.2/279.2	9.2/8.7	273/-
	274.2/279.2	9.2/8.7	273/-
	313.6/313.8	4.9/5.0	314 (TO≈LO)
	323.7/333.7	6.2/11.3	323.4/333
	341.7/356.0	14.3/13.9	341/-
357.0/373.0	14.5/14.7	357/-	
373.1/399.0	14.3/16.5	-/399	
A <sub>2</sub> (cm <sup>-1</sup> )	IR inactive		59.4
	IR inactive		68.7
	IR inactive		117.8
	IR inactive		125.9
	IR inactive		157.4
	IR inactive		253.5
	IR inactive		297.4
	IR inactive		319.4
	IR inactive		332.5
	IR inactive		332.5
B <sub>1</sub> TO/LO (cm <sup>-1</sup> )	-/-	-/-	61.1 (TO≈LO)
	-/-	-/-	93.5 (TO≈LO)
	125.8/133.4	2.6/3.0	125.8/133.3
	164.9/166.0	8.4/9.0	165 (TO≈LO)
	264.9/266.3	9.3/10.3	267 (TO≈LO)
	303.3/303.7	9.4/9.2	-/-
	318.3/334.6	5.0/7.2	318.7/-
	343.6/347.8	11.2/10.4	-/-
	356.4/375.9	10.4/22.8	356.5/-
	376.7/395.8	21.9/23.1	-/-
400.4/408.6	29.7/12.4	-/-	
B <sub>2</sub> TO/LO (cm <sup>-1</sup> )	-/-	-/-	59.3 (TO≈LO)
	96.1/96.4	3.3/3.1	96 (TO≈LO)
	104.7/105.7	4.8/5.2	104.7/105.5
	132.0/132.5	10.2/10.1	133 (TO≈LO)
	142.7/144.9	6.1/6.9	143.2 (TO≈LO)
	276.5/285.1	8.0/8.4	276.2/285
	324.6/329.8	5.9/7.3	325.2 (TO≈LO)
	333.4/336.0	7.2/7.5	334 (TO≈LO)
	348.0/358.4	10.3/8.9	348/-
	362.2/397.7	8.6/11.0	362/-
398.6/410.4	11.1/11.9	-/-	

$\text{cm}^{-1}$  and  $398.6/410.4 \text{ cm}^{-1}$  (this mode is not observed in A<sub>1</sub>). The second sphalerite-like mode is recognized from Table II as the  $323.7/333.7 \text{ cm}^{-1}$  (A<sub>1</sub>),  $318.3/334.6 \text{ cm}^{-1}$  (B<sub>1</sub>),  $324.6/329.8 \text{ cm}^{-1}$  (B<sub>2</sub>), close to the value identified in Ref. [38]. The Li-S bond force constant deduced from Eq.(7) by Sobotta *et al* [38],  $\alpha_{Li} = 24.7 \text{ N/m}$ , is then underestimated by  $(400.4/356)^2 = 24\%$  while the In-S bond force constant, deduced from the second sphalerite-

like mode remains unchanged to  $\alpha_{In} = 53.4 \text{ N/m}$ . But even with this slight correction, the Li-S bond remains still about twice weaker than the In-S bond. In contrast the strength of the Ag-C<sup>VI</sup> bond in chalcopyrite compounds is more comparable to that of the B<sup>III</sup>-C<sup>VI</sup> bonds [38], underlining the specific nature of the lithium-chalcogen bond in crystals with tetrahedral coordination of the atoms. As a consequence, the increased lattice

phonon energy of LIS, as compared with AGS or AGSe, favors heat dissipation, hence a higher thermal conductivity is expected. Indeed, an unpublished measurement of LIS thermal conductivity yielded  $K_a = 6.0$  W/(m·K),  $K_b = 6.2$  W/(m·K) and  $K_c = 7.6$  W/(m·K) [46], e.g. 5 times larger than for AGS and of the same magnitude as for LiNbO<sub>3</sub>.

A last important feature from the vibrational spectra is that the phonon spectrum for LIS is located at wavenumbers below 410 cm<sup>-1</sup>. The IR wavelength cut-off (8.1 μm) in Fig. 3 quite exactly corresponds to three times this highest energy phonon. The long wavelength shape of the transmission curves - and limit of the transparency range - seems then to be simply due to multiphonon processes. It is worth mentioning that, although the vibrational investigations have used rose tinge samples, the phonon spectrum should not depend on coloration since all LIS samples display the same IR cutoff edge, with or without annealing.

## V. THERMAL EXPANSION AND THERMO-OPTIC COEFFICIENTS

The principal thermal expansion and thermo-optic coefficients were determined by using the absolute interferometric dilatometer and the experimental procedure described in Ref. [47]. A two-beam interferometric modified Mach-Zehnder arrangement is employed for dilatation measurements (Fig. 8), while thermo-optic coefficients are obtained using the same set-up by recording changes in optical thickness of a sample acting as a thermal scanning Fabry-Perot interferometer, with the natural reflectivity of the two opposite parallel facets. Three parallelepipedic shaped samples of dimension 5 × 5 × 8 mm<sup>3</sup> cut along the crystallographic axes  $a$ ,  $b$  and  $c$  ( $L = 8$  mm) were used for these measurements. The samples were subjected to linear temperature ramps of 0.2°C/min in the range -20°C - +100°C.

### A. Thermal expansion

In a given temperature interval  $dT$  the linear thermal expansion coefficients are defined as

$$\alpha_i = \frac{1}{L_i} \frac{dL_i}{dT} \quad (8)$$

where  $L_i$  is the sample length along the direction  $i$ , with  $i = a, b, c$ . To be consistent with our assignment of the principal optical axes  $X, Y, Z$  in Section VII, we shall once and for all make the substitutions  $X \equiv b, Y \equiv a, Z \equiv c$  in the following. A plot of the experimental data is reported in Fig. 9.

For the measurement of the thermal expansion the light source of the absolute interferometric dilatometer was a frequency stabilized 2-mW He-Ne laser. A linear

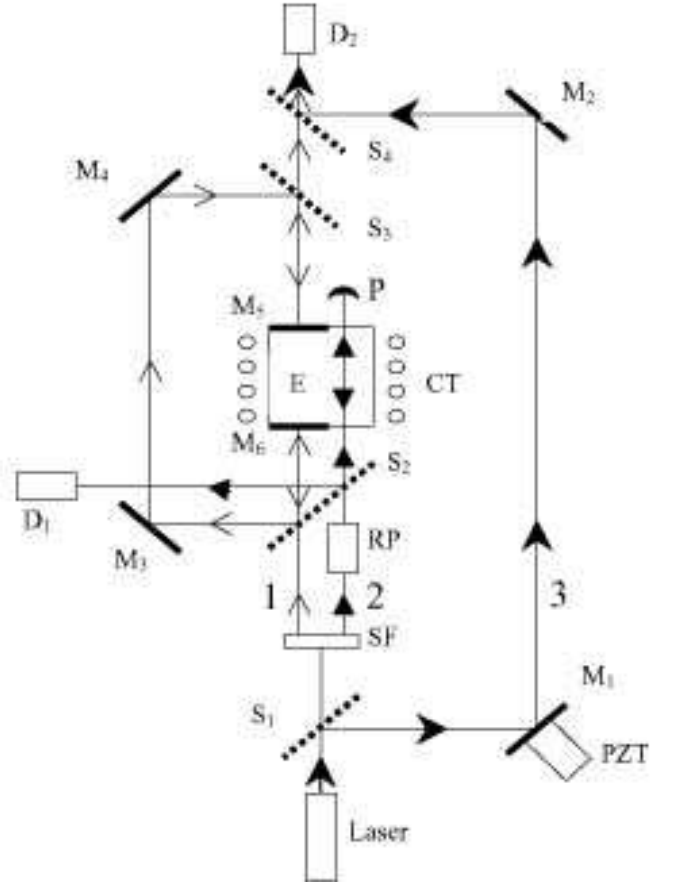


FIG. 8: Schematic of the thermal-scanning Fabry-Perot absolute interferometer (Ref. [47]). E: parallelepipedic polished sample. PZT: piezo-electric transducer. S<sub>1</sub>-S<sub>4</sub>: 50% beam-splitters. P: light dump. M<sub>1</sub>-M<sub>4</sub>: mirrors. SF: beam separator. RP: half-wave plate. CT: programmable temperature controller. Half of the sample parallel facets are metal-coated to form mirrors M<sub>5</sub> and M<sub>6</sub>. D<sub>1,2</sub>: light fringe photodetectors (D<sub>1</sub> is used for thermo-optic coefficients measurements and D<sub>2</sub> for thermal expansion measurements). The temperature is monitored by a thermo-couple embedded in the sample. The whole set-up is located inside vacuum.

fit of the data gives the following temperature dependence of the linear thermal expansion coefficients,

$$\alpha_X = 1.61 \times 10^{-5} + 1.4 \times 10^{-8}T, \quad (9)$$

$$\alpha_Y = 0.89 \times 10^{-5} + 0.7 \times 10^{-8}T, \quad (10)$$

$$\alpha_Z = 0.66 \times 10^{-5} + 0.9 \times 10^{-8}T, \quad (11)$$

where  $T$  is the temperature (°C). The deviation of experimental values from these fits are less than 10<sup>-6</sup> K<sup>-1</sup>. At  $T = 20^\circ\text{C}$  we have  $\alpha_X = 1.64 \times 10^{-5} \text{ K}^{-1}$ ,  $\alpha_Y = 0.90 \times 10^{-5} \text{ K}^{-1}$  and  $\alpha_Z = 0.68 \times 10^{-5} \text{ K}^{-1}$ , respectively. Such values are of the same order of magnitude (or even less) than those for AGS ( $\alpha_{\parallel c} = 1.25 \times 10^{-5} \text{ K}^{-1}$ ,  $\alpha_{\perp c} = -1.32 \times 10^{-5} \text{ K}^{-1}$ ) [48] and AGSe ( $\alpha_{\parallel c} = 1.68 \times 10^{-5} \text{ K}^{-1}$ ,  $\alpha_{\perp c} = -0.78 \times 10^{-5} \text{ K}^{-1}$ ) [49].

However, the main difference with those chalcopyrites is that LIS does not display their anomalous thermal

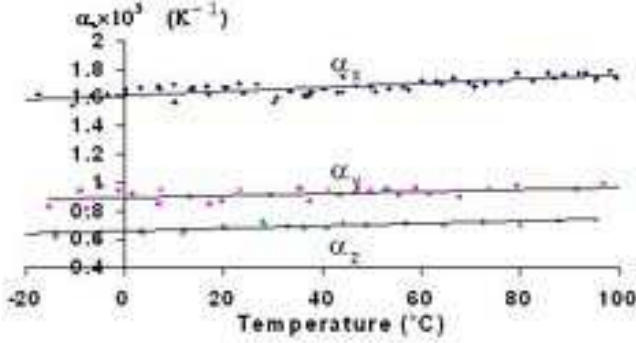


FIG. 9: Thermal expansion coefficients of LIS along the axes  $X \equiv b, Y \equiv a, Z \equiv c$  from  $-20^\circ\text{C}$  to  $+100^\circ\text{C}$ .

expansion behaviour (opposite sign of  $\alpha$  along the two orthogonal directions) that is a major source of thermo-mechanical stress in high power applications [28]. In contrast, LIS expands in the same direction as temperature increases and exhibits a rather weak temperature dependence. This favorable situation is related to the specific nature of the weak Li-S bond already evoked at the end of Subsection III B.

## B. Thermo-optic coefficients

We shall again make use of the labels  $X \equiv b, Y \equiv a, Z \equiv c$  denoting the principal optical axes to describe the change of the index of refraction versus temperature, for a light polarized along one of these principal axes and propagating along another principal direction. For a light wave polarized along direction  $p_j$  and propagating along direction  $e_i$ , we define the coefficient  $\gamma_{ji}$  related to thermal changes in optical thickness (path) by

$$\gamma_{ji} = \frac{1}{n_j L_i} \frac{d(n_j L_i)}{dT} \quad (12)$$

where  $n_j$  and  $L_i$  are respectively the refractive index and the length of the sample, with  $i, j = X, Y$  or  $Z$  and  $i \neq j$ . The thermo-optic coefficients  $\beta_j$ , that we define as  $\beta_j = \frac{1}{n_j} \frac{dn_j}{dT}$ , are derived from (8) and (12) and given by

$$\beta_j = \gamma_{ji} - \alpha_i. \quad (13)$$

As evident from Eq.(13), the knowledge on the values of the thermal expansion is pre-requisite for the interferometric determination of the thermo-optic coefficients at a given wavelength. For the orthorhombic symmetry of LIS it can be seen that each  $\beta_j$  may be obtained for two directions of light propagation. This has been performed at four laser wavelengths chosen in the transparency window of the material, and the resulting linear fits of experimental data are summarized in Table III. At  $\lambda = 1064 \text{ nm}$  and  $T = 20^\circ\text{C}$ , one has  $dn_X/dT = 3.725 \times 10^{-5} \text{ K}^{-1}$ ,  $dn_Y/dT = 4.545 \times$

TABLE III: Principal thermo-optic coefficients  $\beta_j = \frac{1}{n_j} \frac{dn_j}{dT}$  of LIS at four laser wavelengths. Experimental data are fitted to linear expressions  $\beta_j = a_1 + a_2 T$ , where  $T$  is measured in  $^\circ\text{C}$ . The indicated uncertainties in the parameters  $a_1$  and  $a_2$  represent the deviation from the mean value determined from the two possible propagation directions  $e_i$  for a given orientation  $p_j$  of light polarization. We remind that  $X \equiv b, Y \equiv a, Z \equiv c$ .

$\lambda$ ( $\mu\text{m}$ )	$\beta_j$	$10^5 a_1$	$10^8 a_2$
0.4765	$\beta_X$	$3.41 \pm 0.06$	$3.1 \pm 0.3$
	$\beta_Y$	$4.11 \pm 0.07$	$4.6 \pm 0.9$
	$\beta_Z$	$4.08 \pm 0.02$	$4.7 \pm 0.4$
0.6328	$\beta_X$	$2.28 \pm 0.07$	$1.5 \pm 0.4$
	$\beta_Y$	$2.76 \pm 0.05$	$2.1 \pm 0.4$
	$\beta_Z$	$2.69 \pm 0.01$	$2.4 \pm 0.1$
1.0642	$\beta_X$	$1.75 \pm 0.07$	$1.0 \pm 0.06$
	$\beta_Y$	$2.10 \pm 0.11$	$1.3 \pm 0.5$
	$\beta_Z$	$2.03 \pm 0.08$	$1.3 \pm 0.1$
3.392	$\beta_X$	$1.50 \pm 0.07$	$0.7 \pm 0.17$
	$\beta_Y$	$1.83 \pm 0.14$	$1.1 \pm 0.5$
	$\beta_Z$	$1.73 \pm 0.03$	$1.0 \pm 0.02$

$10^{-5} \text{ K}^{-1}$ ,  $dn_Z/dT = 4.467 \times 10^{-5} \text{ K}^{-1}$ . Compared with the thermo-optic coefficients of AGS [50], these values are about 5 times lower. Dispersion relations based on those wavelength-dependent data will be derived in Subsection VII B.

## VI. PIEZO-ELECTRIC AND ELECTRO-OPTIC COEFFICIENTS

### A. Apparent electro-optic coefficients

The measurement of electro-optic coefficients involves the determination of changes in optical thickness when applying an electric field to the material. LIS belongs to the symmetry class  $mm2$  for which the electro-optic tensor exhibits 5 nonzero components, namely  $r_{13}$ ,  $r_{23}$ ,  $r_{33}$ ,  $r_{42}$  and  $r_{51}$  [51]. In this subsection we will describe the electro-optic effect in the principal optic frame where  $XYZ$  are the axes of the index ellipsoid which as we shall see in the next section coincide with the crystallographic  $bac$  axes. We will address only the  $r_{i3}$ 's coefficients that can be obtained by applying a field  $E_3$  along the  $Z$ -axis which does not lead to a rotation of the ellipsoid. Optical interferometric methods may be advantageously used in this case for their determination. An applied electric field  $\mathbf{E}$ , with respective components  $(E_1, E_2, E_3)$  along the principal axes  $(X, Y, Z)$ , will modify the index ellipsoid according to

$$(n_X^{-2} + r_{13}E_3)X^2 + (n_Y^{-2} + r_{23}E_3)Y^2 + (n_Z^{-2} + r_{33}E_3)Z^2 + 2r_{42}E_2YZ + 2r_{51}E_1XZ = 1. \quad (14)$$

The new indices  $n_i(E_3)$  ( $i \equiv 1, 2, 3 \equiv X, Y, Z$ ) are given by

$$n_i(E_3) = n_i - \frac{1}{2}n_i^3 r_{i3} E_3 \quad (15)$$

where  $\delta(n_i) = -\frac{1}{2}n_i^3 r_{i3} E_3$  represents the variation of the refractive index  $n_i$ .

Due to the piezo-electric effect the field  $E_3$  will also generate a variation  $\delta(L_j)$  of the crystal thickness  $L_j$  along a given direction  $e_j$  such that

$$\delta(L_j) = L_j \bar{d}_{3j} E_3 \quad (16)$$

where  $\bar{d}_{3j}$  ( $j = 1, 2, 3$ ) are components of the piezo-electric tensor [52]. For a light wave propagating along direction  $e_j$  and polarized along direction  $p_i$  of the crystal the variation  $\delta(n_i L_j)$  of the optical path  $n_i L_j$  induced by an applied electric field  $E_3$  will be

$$\delta(n_i L_j) = n_i L_j \left( \bar{d}_{3j} - \frac{1}{2}n_i^2 r_{i3} \right) E_3. \quad (17)$$

We define the *effective* electro-optic coefficients as

$$r_{i3}^{\text{eff}} = -\frac{2}{n_i^2} \left( \bar{d}_{3j} - \frac{1}{2}n_i^2 r_{i3} \right) \quad (18)$$

with  $j = 1, 2$ , which represent in fact the (apparent) electro-optic coefficients obtained in most experiments where the piezo-electric contribution is ignored. The measurements of the  $r_{i3}^{\text{eff}}$ 's were performed by using the technique of Phase-modulated Thermal Scanning Interferometry (PTSI) [53]. In this method, as for the measurements of thermo-optic coefficients, the sample acts as a Fabry-Perot thermal scanning interferometer in which phase modulation is achieved by applying an AC field  $E_3$  along the Z axis. The various configurations of light polarization ( $E_X, E_Y, E_Z$ ) and wave vector  $\mathbf{k}$  ( $k_X, k_Y$ ) used to determine the apparent electro-optic coefficients of LIS are depicted in Fig. 10.

Two of the LIS samples of aperture  $5 \times 5 \text{ mm}^2$  used in Section V with lengths  $L = 8 \text{ mm}$  along the X and Y propagation axes were supplied with gold evaporated electrodes on their Z facets. The low frequency (480 Hz) applied voltage was 200 V peak-to-peak and linear temperature ramps of  $0.2^\circ\text{C}/\text{min}$  were used from  $20^\circ\text{C}$  to  $55^\circ\text{C}$ . Measurements of apparent electro-optic coefficients were performed at  $1.064 \mu\text{m}$  by using a 100mW TEM<sub>00</sub> single-frequency Nd:YAG laser. In the scanned temperature interval a constant value has been observed for each of them; they are summarized in Table IV. These data feature a quite weak electro-optic effect in LIS and the large discrepancy observed between  $r_{i3(X)}^{\text{eff}}$  and  $r_{i3(Y)}^{\text{eff}}$  suggests a strong contribution of the piezo-electric effect to the apparent electro-optic one.

## B. Piezo-electric and pure electro-optic coefficients

The non-vanishing piezo-electric coefficients  $\bar{d}_{31}$ ,  $\bar{d}_{32}$  and  $\bar{d}_{33}$  were measured by using the modified Mach-

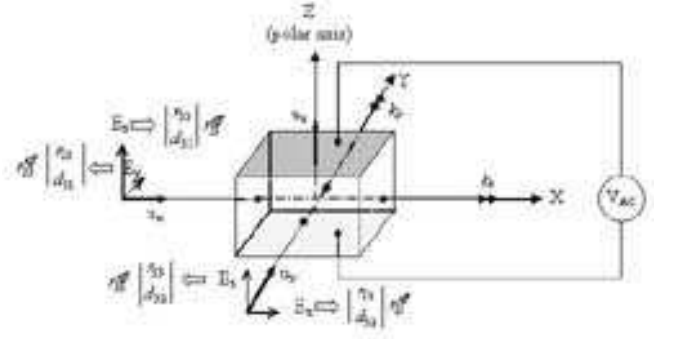


FIG. 10: Geometrical configurations used to measure the apparent electro-optic coefficients  $r_{i3}^{\text{eff}}$  of LIS. The various piezo-electric  $\bar{d}_{3j}$ , and true electro-optic  $r_{i3}$  coefficients involved are indicated for each one of them. The  $u_j$ 's denote thickness variations  $\delta(L_j)$ .

TABLE IV: Apparent electro-optic coefficients of LIS; 3(X) and 3(Y) represent the values of  $r_{33}^{\text{eff}}$  obtained for a light propagation along X and along Y, respectively.

$i$	$r_{i3}^{\text{eff}}$ (pm/V)
1	$2.18 \pm 0.04$
2	$2.82 \pm 0.33$
3(X)	$0.93 \pm 0.03$
3(Y)	$0.11 \pm 0.02$

Zehnder arrangement of the absolute interferometric dilatometer in a manner similar to the one employed for dilatation measurements (Fig. 8). Phase modulation of the interference pattern is performed by applying to the samples the same voltage and same thermal scanning procedure as described previously. The algebraic sign of the coefficients was attributed according to the ANSI/IEEE Standard 176-1987 on piezo-electric crystals [54] and we have found in pm/V units and in the XYZ frame:  $\bar{d}_{31} = -5.6 \pm 0.1$ ,  $\bar{d}_{32} = -2.7 \pm 0.2$  and  $\bar{d}_{33} = +7.5 \pm 0.2$ .

From Equation (18) we determine the pure electro-optic coefficients  $r_{13} = 1.0 \text{ pm/V}$ ,  $r_{23} = 0.4 \text{ pm/V}$  and  $r_{33} = -1.3 \text{ pm/V}$  which reveals a rather small true electro-optic effect compared to the piezo-electric one. The relative uncertainty in these values is close to 15%. These measurements confirm that, as AGS or AGSe, LIS is a poor candidate for electro-optic or piezo-electric based devices. A comparison of our results with earlier data of Negran *et al* [55] cannot be meaningful since the  $r_{13}$ ,  $r_{23}$  and  $r_{33}$  that were measured there did not account for the piezo-electric contribution and were not determined independently, but as a linear combination.

### C. Comparison of the electro-optic and pyroelectric coefficients

From the anharmonic oscillator model developed by Garrett [56], Soref [57] yields a semi empirical relationship between the pyroelectric coefficient at constant stress  $\sigma$  ( $p^\sigma = (\frac{\Delta P_s}{\Delta T})_\sigma$ ) and the second-order electronic susceptibility  $\chi^{(2)}$  describing the linear (true) electro-optic effect:

$$p^\sigma = \chi^{(2)}(\omega \pm 0; \omega, 0) 2C_v \frac{\epsilon_0 m_e^2 (\omega_e^2 - \omega^2)^2}{\mu \omega_i^2 N_A e^2} \left( \frac{3A + B}{C + 3D} \right). \quad (19)$$

The pyroelectric coefficient  $p^\sigma$  gives the variation of the spontaneous polarization  $\Delta P_s$  induced by a temperature variation  $\Delta T$ . The parameters  $m_e$  and  $e$  are the mass and charge of the electron,  $\omega_e$  and  $\omega_i$  are respectively the electronic and ionic resonance frequencies,  $C_v$  is the molar specific heat at constant volume (which differs from the specific heat at constant pressure  $C_p$  measured in Section III by a negligible quantity) and  $N_A$  the Avogadro number. The constant terms  $A, B, C$  and  $D$  are the coefficients related to the third order expansion of the crystal potential energy in the electronic and ionic coordinate system  $q_e$  and  $q_i$  [57]. The ratio  $(3A + B)/(C + 3D)$  indicates the extent to which the predominant ionic contribution to the anharmonic potential at  $\omega \approx \omega_i$  differs from the predominant electronic one at  $\omega \gg \omega_i$ . This ratio is expected to be constant whatever the material, suggesting a linear relationship between the electro-optic and pyroelectric coefficients. This hypothesis was verified for a few known materials, mostly of the oxide type, as can be seen on Fig. 11 which represents the correlation between the pyroelectric coefficient and the second order susceptibility.

The plot figuring LIS is obtained by using  $C_v = C_p$  as measured in section III and  $\chi_{333}^{(2)} = n_3^4 r_{33}$  from the previous sub-section. The pyroelectric coefficient was measured previously [58] as a function of temperature and its value extrapolated at 300 K is  $p^\sigma = 6 \times 10^{-10} \text{ C} \cdot \text{cm}^{-2} \text{ K}^{-1}$ . We observe that Soref's hypothesis is confirmed for the ternary semiconductor LIS, as it was already shown for the binary one CdS [57]. We note also that a rather good estimate of the pyroelectric effect may be deduced from electro-optic measurements and vice versa, but this requires at first an accurate determination of the piezo-electric contribution.

## VII. LINEAR OPTICAL AND THERMO-OPTIC DISPERSIONS

### A. Sellmeier equations at room-temperature ( $T = 20^\circ$ )

The only available dispersion data of LIS, measured using the minimum deviation technique, were compiled by

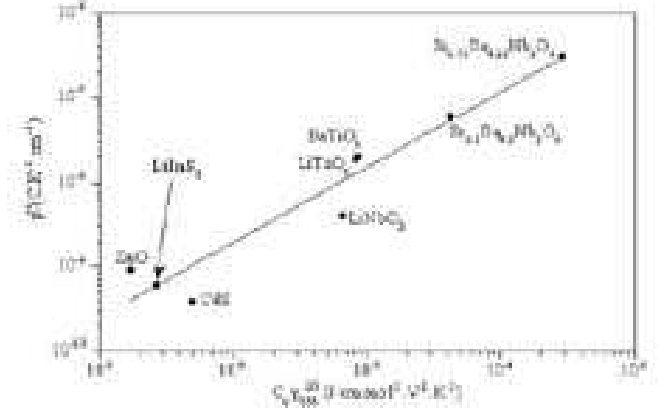


FIG. 11: Correlation between pyroelectric coefficient and second order susceptibility of several materials. LiInS<sub>2</sub>: our results; other compounds from Ref. [57].

Boyd *et al* in 1973 [11] and fitted to one-pole (UV) Sellmeier equations [59] reproduced also in Refs. [18, 60, 61]. Although the accuracy of their index determination was not reported, from subsequent nonlinear phase-matched conversion experiments it appeared that the Sellmeier equations based on their data are accurate to predict the birefringence (via angle acceptance bandwidth measurements [16]), but fail to predict accurately the absolute phase-matching directions. Discrepancies of several degrees from the expected phase-matching angles were reported [17], especially for wavevector propagation in the  $a - c$  plane where discrepancies of  $+6^\circ$  were found for the SHG of 2.55-2.65  $\mu\text{m}$  [40]. Such deviations cannot be attributed to the X-ray sample orientation uncertainties ( $\pm 0.5^\circ$ ). Furthermore, we have checked that the phase-matching angles, and hence the linear refractive indices, are independent of crystal coloration or exact stoichiometry.

Following the standard convention for assigning the principal axes ( $X, Y, Z$ ) to the crystallographic axes ( $a, b, c$ ), e.g.  $n_X < n_Y < n_Z$ , one has  $X \leftrightarrow b, Y \leftrightarrow a$  and  $Z \leftrightarrow c$  for LIS since  $n_b < n_a < n_c$ . A phase-matching direction will be labelled by  $(\theta, \varphi)$ , where  $\theta$  is the angle of the wavevector respective to the polar  $Z$  axis and  $\varphi$  is the azimuthal angle between its projection in the  $X - Y$  plane and the  $X$  axis. We have used the experimental type-II (eoe, oeo) SHG angles measured in the fundamental wavelength range 2.5 - 6  $\mu\text{m}$  [17, 40] to refit the Sellmeier equations given in Ref. [59]. The SHG data were supplemented with new recent data derived from type-II (eoe) difference-frequency generation (DFG) of two tunable cw Ti:sapphire lasers in the X-Y plane (see Subsection X B). It is therein shown that it is possible to generate mid-IR wavelength  $\lambda_1$  in the range 5.5 - 11.3  $\mu\text{m}$  by angle-tuning a 10-mm length yellow-tinge LIS sample cut at  $(\theta, \varphi) = (90^\circ, 42^\circ)$ . To avoid phase-matching angle measurement, the crystal was also studied at normal incidence while both pump lasers were tuned yielding  $(\lambda_3, \lambda_2, \lambda_1)$

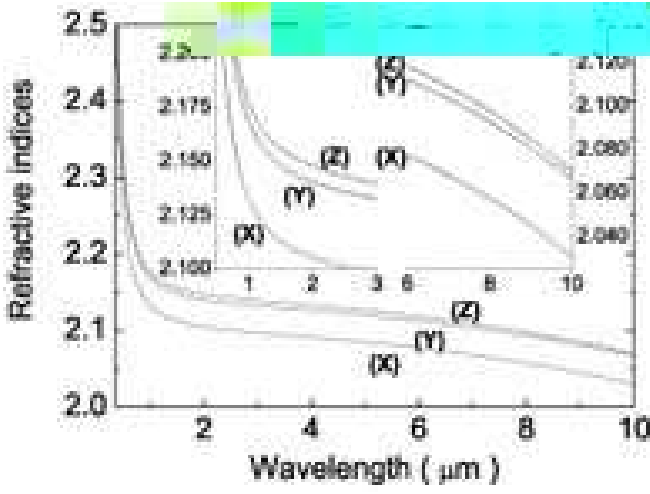


FIG. 12: Principal refractive indices of  $\text{LiInS}_2$  as computed from Eqs.(20)-(22). The inset plots show the UV and mid-IR portions on an expanded scale and also a comparison with a calculation based on the Sellmeier expansions from Ref. [59] (dotted lines).

phase-matched triplets used in the Sellmeier equations fit. With this wavelength-tuning mode, mid-IR down-conversion in the range  $\lambda_1 \in [6.6 - 7] \mu\text{m}$  was achieved. Table V compiles the experimental phase-matching data used to derive the following two-pole Sellmeier equations, valid over the full transparency window, using a nonlinear least-square fit of the data,

$$n_X^2 = 6.686059 + \frac{0.1385833}{\lambda^2 - 0.05910334} + \frac{2047.46509}{\lambda^2 - 897.7476} \quad (20)$$

$$n_Y^2 = 7.095493 + \frac{0.1422326}{\lambda^2 - 0.06614640} + \frac{2511.08936}{\lambda^2 - 988.2024} \quad (21)$$

$$n_Z^2 = 7.256327 + \frac{0.15072}{\lambda^2 - 0.06823652} + \frac{2626.10840}{\lambda^2 - 983.0503} \quad (22)$$

In Eqs.(20)-(22), the wavelengths are expressed in microns. The three IR wavelength poles  $\lambda_{IR}(X) = 29.96 \mu\text{m}$ ,  $\lambda_{IR}(Y) = 31.44 \mu\text{m}$ ,  $\lambda_{IR}(Z) = 31.35 \mu\text{m}$  (i.e.  $\bar{\nu}(X) = 333.7 \text{ cm}^{-1}$ ,  $\bar{\nu}(Y) = 318.1 \text{ cm}^{-1}$ ,  $\bar{\nu}(Z) = 318.9 \text{ cm}^{-1}$ ) correspond to the medium-frequency phonon band-centers of symmetry  $B_2$ ,  $B_1$  and  $A_1$  respectively, attributed to the In-S vibrations (see Table II). Fig. 12 displays the principal indices of refraction deduced from Eqs.(20)-(22) (the dotted lines are calculated using the Sellmeier expansions from Refs. [18, 59, 60]). The smaller birefringence  $\Delta n_{Y-Z} \simeq -0.006$  - as compared with  $\Delta n_{X-Z} \simeq -0.04$  at  $5 \mu\text{m}$  - explains the large  $+6^\circ$  discrepancies with the Sellmeier predictions of Ref. [59], previously observed in the Y-Z plane (inset of Fig. 14 and Ref.[40]). No anomalous index surface crossing is found in the blue part of the dispersion data, in contrast with the uniaxial AGS which has  $n_o = n_e$  at  $\lambda = 460 \text{ nm}$  [50]. The two optic axes, lying in the X-Z plane, determine the propagation directions where the index of refraction is independent of the polarization. The angle between

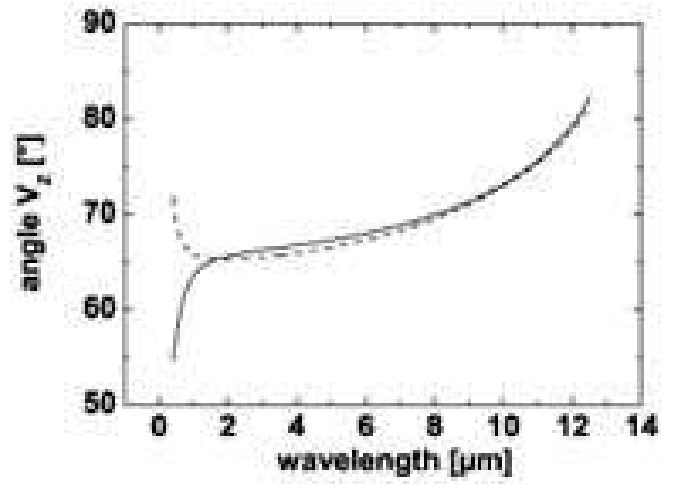


FIG. 13: Angle  $V_Z$  between the optic axes and the Z-axis in LIS calculated with the Sellmeier expansion of Ref. [59] (dashed line), and the new Sellmeier expansion (Eqs.(20)-(22)) (solid line).

the two optic axes is  $2V_Z$  where  $V_Z$  is the angle of each axis with the polar Z-axis.  $V_Z$  is wavelength dependent and can be calculated from [4]

$$\sin V_Z = \frac{n_Z(n_Y^2 - n_X^2)^{1/2}}{n_Y(n_Z^2 - n_X^2)^{1/2}}. \quad (23)$$

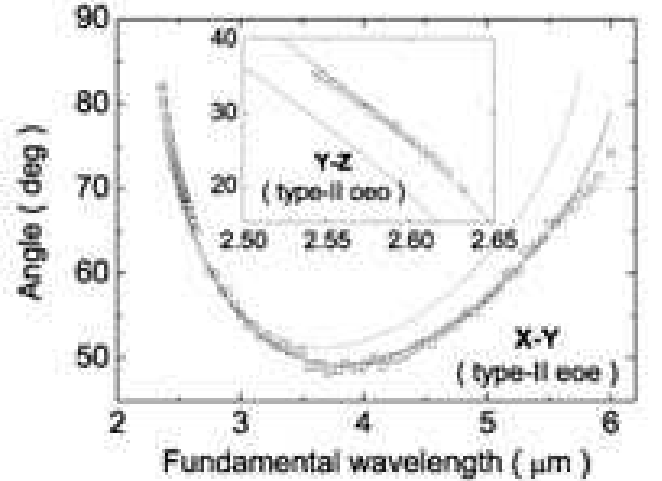


FIG. 14: Phase-matching angles for type-II (*oeo* or *oeo*) SHG in the X-Y principal plane (main frame) and type-II (*ooo* or *ooo*) SHG in the Y-Z plane (inset frame) of LIS. The fundamental source for  $\lambda < 2.65 \mu\text{m}$  ( $\lambda > 2.75 \mu\text{m}$ , respectively) is the idler wave of a Nd:YAG-pumped nanosecond  $\text{LiNbO}_3$  parametric oscillator (the frequency-doubled radiation from a Free-Electron Laser). The symbols refer to experiments while the solid lines are calculated from Eqs.(20)-(22). The dashed lines are computed from the Sellmeier equations of Refs. [59].

Fig. 13 plots  $V_Z$  as a function of the wavelength, using

TABLE V: Phase-matching conditions for type-II SHG and DFG in LiInS<sub>2</sub>.

	Wavelength ( $\mu\text{m}$ ) <sup>a</sup>			Phase-Matching Angles ( $\theta, \varphi$ ) <sup>b</sup>	
	$\lambda_1$	$\lambda_2$	$\lambda_3$	Measured	Calculated
SHG (XY: <i>oeo</i> )	2366	2366	1183	(90, 82.1)	(90, 83.908)
	2469	2469	1234.5	(90, 73.1)	(90, 72.755)
	2527	2527	1263.5	(90, 69.8)	(90, 69.235)
	2583	2583	1291.5	(90, 67.4)	(90, 66.507)
	2900	2900	1450	(90, 57.9)	(90, 56.884)
	3400	3400	1700	(90, 50.7)	(90, 50.543)
	3700	3700	1850	(90, 48.3)	(90, 49.392)
	3900	3900	1950	(90, 49.0)	(90, 49.381)
	4450	4450	2225	(90, 51.6)	(90, 51.772)
	4950	4950	2475	(90, 56.3)	(90, 56.543)
	5350	5350	2675	(90, 62.8)	(90, 62.227)
	5550	5550	2775	(90, 66.0)	(90, 65.916)
	5750	5750	2875	(90, 69.1)	(90, 70.508)
	5900	5900	2950	(90, 71.4)	(90, 75.006)
SHG (YZ: <i>ooo</i> )	2542.7	2542.7	1371.35	(35.4, 90)	(36.452, 90)
	2552.7	2552.7	1276.35	(34.0, 90)	(34.684, 90)
	2570.4	2570.4	1285.2	(31.0, 90)	(31.508, 90)
	2587	2587	1293.5	(28.7, 90)	(28.435, 90)
	2602.3	2602.3	1301.15	(25.9, 90)	(25.481, 90)
	2606.7	2606.7	1303.35	(25.1, 90)	(24.592, 90)
	2631.4	2631.4	1315.7	(19.6, 90)	(19.211, 90)
DFG (XY: <i>oeo</i> )	6585.14	872.240	770.220	(90, 42)	(90, 42.170)
	6623.95	865.801	765.716	(90, 42)	(90, 42.145)
	6719.87	850.443	754.905	(90, 42)	(90, 42.076)
	6762.44	843.761	750.162	(90, 42)	(90, 42.046)
	6832.63	833.187	742.629	(90, 42)	(90, 41.992)
	6899.92	822.391	734.810	(90, 42)	(90, 41.967)
	6989.56	810.827	726.544	(90, 42)	(90, 41.863)

<sup>a</sup> $1/\lambda_1 + 1/\lambda_2 = 1/\lambda_3$  with  $\lambda_1 \geq \lambda_2 > \lambda_3$ .

<sup>b</sup>In degree.

Eqs.(20)-(22) (solid line) and using the Sellmeier equations of Ref. [59] (dashed line). Let us note the different behavior for  $\lambda < 1 \mu\text{m}$  (absence of a retracing behavior). Note that although the principal indices on which the previous dispersion relations are based were measured from the minimum deviation technique in 1973 [11], the absorption coefficient of the prism samples used then was quite different (much larger than in Fig. 3 or in Table I up to about  $2.5 \mu\text{m}$ ) which obviously is the reason for the difference observed in Fig. 13. Since  $V_Z > 45^\circ$  LIS is a negative biaxial crystal. At longer wavelengths it can be regarded as quasi-uniaxial, which is a consequence of the fact that the two indices  $n_Y$  and  $n_Z$  are very close. Therefore no phase-matching can be expected for propagation directions in the vicinity the X-principal axis.

The agreement between the experimental phase-matching data used to derive Eqs.(20)-(22) and the calculated ones is illustrated in Fig.14 (solid lines) and Table V. The accuracy of phase-matching angle prediction is  $\pm 1.5^\circ$ . The eight last SHG points in Fig. 14 were discarded from the nonlinear fit for obvious lack of reliability. Only a two-pole form leads to the smallest resid-

ual discrepancies between calculated and experimental data, while the former one-pole Sellmeier equations [59] are unable to predict SHG near the cut-off wavelength of  $\sim 6 \mu\text{m}$ . Wavelength non-critical SHG occurs at around  $\lambda = 3.7 \mu\text{m}$  in the X-Y plane. Due to the small Y-Z birefringence, type-II (*ooo* or *oeo*) SHG in the Y-Z plane for the experimentally studied branch is restricted as we shall see in the next section to  $2353 < \lambda < 2675 \text{ nm}$  (with vanishing nonlinearity at this second cut-off wavelength), while in the X-Y plane type-II (*oeo* or *oee*) SHG is possible for  $2353 < \lambda < 6111 \text{ nm}$ . By comparison, the DFG phase-matching curves calculated with the previous one-pole Sellmeier equations are shifted upward by  $\sim +40 \text{ nm}$ . Under the usual designation  $\lambda_1 \geq \lambda_2 > \lambda_3$  the FWHM DFG angular acceptance (FWHM) measured at fixed wavelengths was  $\Delta\varphi = 0.19^\circ$  for a crystal length of 10 mm, e.g. much smaller than the uncertainty on crystal orientation ( $\pm 0.5^\circ$ ). Hence the uncertainty ( $\pm 1 \text{ nm}$  at maximum) of wavelength measurement in Table V cannot explain the  $\sim 40 \text{ nm}$  shift observed with the previous Sellmeier equations, confirming the increased accuracy in dispersion provided by Eqs.(20)-(22).

## B. Thermo-optic dispersion relations

The thermo-optic coefficients  $\beta_j$  [Eq. (13)] are functions of both temperature  $T$  and wavelength  $\lambda$ . From the determined temperature behavior (subsection VB), they will be expressed as

$$\beta(\lambda, T) = a_1(\lambda) + a_2(\lambda)T. \quad (24)$$

In analogy with the index dispersion equations at room-temperature (see previous Subsection A) the parameters  $a_k$  ( $k = 1, 2$ ) in Table III are fitted according to the following two-pole functional form,

$$a_k(\lambda) = C_{0,k} + \frac{C_{1,k}}{\lambda^2 - \lambda_{01,k}^2} + \frac{C_{2,k}}{\lambda^2 - \lambda_{02,k}^2}. \quad (25)$$

Table VI compiles the fitting parameters  $C_{0,k}$ ,  $C_{1,k}$ ,  $C_{2,k}$ ,  $\lambda_{01,k}$  and  $\lambda_{02,k}$ . According to the definition of  $\beta_j(\lambda, T)$  ( $\beta_j = \frac{1}{n_j} \frac{dn_j}{dT}$ ), the index of refraction at a given temperature  $T$  will be given by

$$\begin{aligned} \frac{n(\lambda, T)}{n(\lambda, T_0)} &= \exp \left[ a_1(\lambda)(T - T_0) + a_2(\lambda) \frac{(T - T_0)^2}{2} \right] \\ &\simeq 1 + a_1(\lambda)(T - T_0) + a_2(\lambda) \frac{(T - T_0)^2}{2} \end{aligned} \quad (26)$$

where  $T_0 = 20^\circ\text{C}$  and  $n(\lambda, T_0)$  is given by Eqs.(20)-(22).

These thermo-optic dispersion relations will have to be refined by experimental temperature phase-matching data in the future. Relations (25) with the constant values in Table VI would provide a suitable basis for such a refit procedure. They predict a FWHM temperature acceptance of  $\Delta TL = 248^\circ\text{C}\cdot\text{cm}$  ( $L$ : crystal length) at room temperature for the type-II (eoe) SHG of  $\lambda = 2.5\ \mu\text{m}$  in the X-Y plane, hence an extremely low temperature dependence when the three wavelengths are located in the mid-IR spectral region of constant dispersion. However for the DFG of near-IR sources ( $\lambda_3 = 754.905\ \text{nm}$ ,  $\lambda_2 = 850.443\ \text{nm}$ , see Table V), the FWHM temperature acceptance is predicted to be only  $\Delta TL = 46^\circ\text{C}\cdot\text{cm}$ . Hence LIS is expected to be very stable against self-induced thermal effects. As a counterpart, its temperature tunability is expected to be somewhat reduced.

## VIII. PHASE-MATCHING INVESTIGATIONS

### A. Effective nonlinearity and Hobden classification

The phase-matching loci and the effective nonlinearity for LIS will be analyzed in the XYZ-principal optic axis frame, but the tensor elements of the nonlinear susceptibility are defined traditionally, in accordance with ANSI/IEEE Std 176-1987 [54], in the *abc*-crystallographic frame where  $c$  is the polar two-fold axis as in Ref. [11]. The chosen convention  $n_X < n_Y < n_Z$

in order to have the two optic axes in the X-Z principal plane affects therefore the expressions for the effective second order nonlinearity  $d_{\text{eff}}$ .

The general form of the contracted  $\mathbf{d}^{(2)}$  tensor for the orthorhombic class *mm2* reads as

$$\mathbf{d}^{(2)} = \begin{pmatrix} 0 & 0 & 0 & 0 & d_{15} & 0 \\ 0 & 0 & 0 & d_{24} & 0 & 0 \\ d_{31} & d_{32} & d_{33} & 0 & 0 & 0 \end{pmatrix}. \quad (27)$$

For an arbitrary propagation direction assuming collinear interaction and neglecting the spatial walk-off effect analytical expressions for  $d_{\text{eff}}$  can be derived in our conventions from the general formulae presented by Dmitriev *et al* [63],

$$\begin{aligned} d_{\text{eff}}^{ssf} &= 2 d_{15} \sin \theta \cos \delta (\cos \theta \sin \varphi \sin \delta - \cos \varphi \cos \delta) \\ &\quad \times (\cos \theta \sin \varphi \cos \delta + \cos \varphi \sin \delta) \\ &\quad + 2 d_{24} \sin \theta \cos \delta (\cos \theta \cos \varphi \cos \delta - \sin \varphi \sin \delta) \\ &\quad \times (\cos \theta \cos \varphi \sin \delta + \sin \varphi \cos \delta) \\ &\quad + d_{31} \sin \theta \sin \delta (\cos \theta \sin \varphi \cos \delta + \cos \varphi \sin \delta)^2 \\ &\quad + d_{32} \sin \theta \sin \delta (\cos \theta \cos \varphi \cos \delta - \sin \varphi \sin \delta)^2 \\ &\quad + d_{33} \sin^3 \theta \cos^2 \delta \sin \delta \end{aligned} \quad (28)$$

and

$$\begin{aligned} d_{\text{eff}}^{fssf} &= d_{\text{eff}}^{sfff} \\ &= -d_{15} [\sin \theta \cos \delta (\cos \theta \sin \varphi \sin \delta - \cos \varphi \cos \delta)^2 \\ &\quad + \sin \theta \sin \delta (\cos \theta \sin \varphi \sin \delta - \cos \varphi \cos \delta) \\ &\quad \times (\cos \theta \sin \varphi \cos \delta + \cos \varphi \sin \delta)] \\ &\quad - d_{24} [\sin \theta \cos \delta (\cos \theta \sin \varphi \sin \delta + \sin \varphi \cos \delta)^2 \\ &\quad + \sin \theta \sin \delta (\cos \theta \cos \varphi \cos \delta - \sin \varphi \sin \delta) \\ &\quad \times (\cos \theta \cos \varphi \sin \delta + \sin \varphi \cos \delta)] \\ &\quad - d_{31} \sin \theta \sin \delta (\cos \theta \sin \varphi \sin \delta - \cos \varphi \cos \delta) \\ &\quad \times (\cos \theta \sin \varphi \cos \delta + \cos \varphi \sin \delta) \\ &\quad - d_{32} \sin \theta \sin \delta (\cos \theta \cos \varphi \cos \delta - \sin \varphi \sin \delta) \\ &\quad \times (\cos \theta \cos \varphi \sin \delta + \sin \varphi \cos \delta) \\ &\quad - d_{33} \sin^3 \theta \sin^2 \delta \cos \delta \end{aligned} \quad (29)$$

for type-I and type-II phase-matching, respectively, where the superscripts "s" and "f" stand for the "slow" and "fast" eigenmodes of polarization and their sequence follows the usual convention  $\lambda_1 \lambda_2 \lambda_3$  with  $\lambda_1 \geq \lambda_2 > \lambda_3$ . The angle  $\delta$  whose introduction simplifies the expressions and which is determined from

$$\tan 2\delta = \frac{\cos \theta \sin 2\varphi}{\cot^2 V_Z \sin^2 \theta + \sin^2 \varphi - \cos^2 \theta \cos^2 \varphi} \quad (30)$$

( $0 < 2\delta < \pi$ ) defines the polarization directions of the slow and fast waves which are orthogonal to each other. It is the angle between the polarization direction of the

TABLE VI: Fitting parameters describing the thermal and wavelength dependence of the principal thermo-optic coefficients of LIS, according to Eqs.(24)-(25).

$a_k(\lambda)$	$p_i$	$C_0$	$C_1$	$C_2$	$\lambda_{01}$	$\lambda_{02}$
$a_1$	X	$2.899680 \times 10^{-5}$	$0.2033761 \times 10^{-5}$	$297.0535 \times 10^{-5}$	0.3475601	14.86755
	Y	$2.478267 \times 10^{-5}$	$0.2612463 \times 10^{-5}$	$122.3207 \times 10^{-5}$	0.3391212	13.91854
	Z	$3.315830 \times 10^{-5}$	$0.2555208 \times 10^{-5}$	$364.9813 \times 10^{-5}$	0.3451539	15.44113
$a_2$	X	$1.987083 \times 10^{-8}$	$0.1860292 \times 10^{-8}$	$250.0777 \times 10^{-8}$	0.3886392	14.25991
	Y	$0.1523235 \times 10^{-8}$	$0.2601335 \times 10^{-8}$	$-191.8712 \times 10^{-8}$	0.3969192	14.79803
	Z	$-06564806 \times 10^{-8}$	$0.4291068 \times 10^{-8}$	$-343.1015 \times 10^{-8}$	0.3435849	14.94811

slow wave and the plane of propagation containing the principal Z-axis. An approach for the generalization of the  $d_{\text{eff}}$  expressions in the case of collinear interactions taking into account the spatial walk-off can be found in Ref. [64].

In the principal planes the expressions for  $d_{\text{eff}}$  (28)-(29) are reduced to:

$$d_{\text{eff}}^{oee} = d_{\text{eff}}^{oeo} = -(d_{24} \sin^2 \varphi + d_{15} \cos^2 \varphi) \text{ (X-Y)}, (31)$$

$$d_{\text{eff}}^{eoo} = d_{\text{eff}}^{eoe} = -d_{24} \sin \theta \text{ (Y-Z plane)}, (32)$$

$$d_{\text{eff}}^{oeo} = +d_{31} \sin \theta \text{ (X-Z plane, } \theta < V_Z), (33)$$

$$d_{\text{eff}}^{eoe} = d_{\text{eff}}^{eoo} = -d_{15} \sin \theta \text{ (X-Z plane, } \theta > V_Z) (34)$$

with superscripts "o" and "e" denoting the ordinary and extraordinary beams. LIS behaves as an optically negative uniaxial crystal in the X-Y and X-Z (for  $\theta < V_Z$ ) planes and as an optically positive uniaxial crystal in the Y-Z and X-Z (for  $\theta > V_Z$ ) planes. Assuming the Kleinman symmetry condition to hold then  $d_{15} = d_{31}$  and  $d_{24} = d_{32}$ .

The biaxial phase-matching loci for collinear SHG can be categorized using the classification of Hobden [65]. Our calculations based on the relatively simple transcendental equations derived by Yao *et al* [66], predict that no phase-matched SHG is possible below 1618 nm. LIS enters Hobden's class 13 at 1618 nm, class 11 at 1783 nm, class 10 at 2353 nm, and class 9 at 2675 nm, then it goes back to class 10 at 5493 nm, to class 11 at 6111 nm, to class 13 at 8224 nm, and finally no SHG phase-matching is possible again above 8710 nm. These transitional fundamental wavelengths correspond to propagation directions along the Y - or along the Z - principal axes (noncritical phase-matching) either for the *ssf* or the *fsf* (*fff*) polarization configurations.

Figs. 15a,b illustrate the different classes for SHG in LIS at several representative fundamental wavelengths. The surface of the unit sphere is projected onto the X-Z plane of the crystal. The direction of the wave vectors of the interacting waves for phase-matching as given by their interception with the surface of the unit sphere is plotted.

The stereographic projection of the first octant is presented only but the loci in the other octants can be obtained by mirror reflections across the principal planes.

We do not present plots of the angle  $\delta$  which can be easily calculated from Eq.(30). Its dispersive properties (determined by the angle  $V_Z$ ) lead to slightly different values at the three interacting wavelengths but normally the effect on the conversion efficiency can be neglected. Qualitative arguments relating the spatial walk-off (magnitude and direction) to the topology depicted in Fig. 15 can be found in Ref. [31]. The calculation of the spatial walk-off for an arbitrary propagation direction is beyond the scope of this paper but several works provide suitable approaches to this aim [67, 68, 69, 70]. Analytical approaches for the estimation of acceptance parameters based on the small-signal approximation in the general case of biaxial crystals can be found in Ref. [68, 77]. We note here only, that since the angle  $V_Z$  for LIS is not far from  $90^\circ$  the dispersive properties and in particular the spectral acceptance are not expected to be substantially modified by propagation outside the principal planes. Fig. 15 indicates that double solutions for the angles exist (e.g. for Hobden's class 9) which is equivalent to the existence of points outside the principal planes where  $\partial\varphi/\partial\theta = 0$  holds. This means that noncritical phase-matching can also occur outside the principal planes (e.g. at  $\varphi = 26.7^\circ, \theta = 74.35^\circ$  for *ssf* type SHG at  $4 \mu\text{m}$ ).

## B. SHG in principal planes

The SHG phase-matching directions in the principal planes are shown in the lower part of Fig. 16. The two first panels (X-Y) and (Y-Z) in the bottom part correspond respectively to the experimental phase-matching plots in the main and inset panels of Fig. 14. The transitional wavelengths enumerated above can be easily identified there. The SHG ranges where  $d_{\text{eff}} \neq 0$  are 1783-8224 nm for type-I (*oeo*) phase-matching in the X-Z plane, 2353-6111 nm for type-II (*oeo*) phase-matching in the X-Y plane, and 2353-2675 nm and 5493-6111 nm for type-II (*oeo*) phase-matching in the Y-Z plane. We observe an interesting feature in this crystal: the SHG limits with  $d_{\text{eff}} \neq 0$  are larger for propagation *outside* the principal planes where type-I phase-matching down

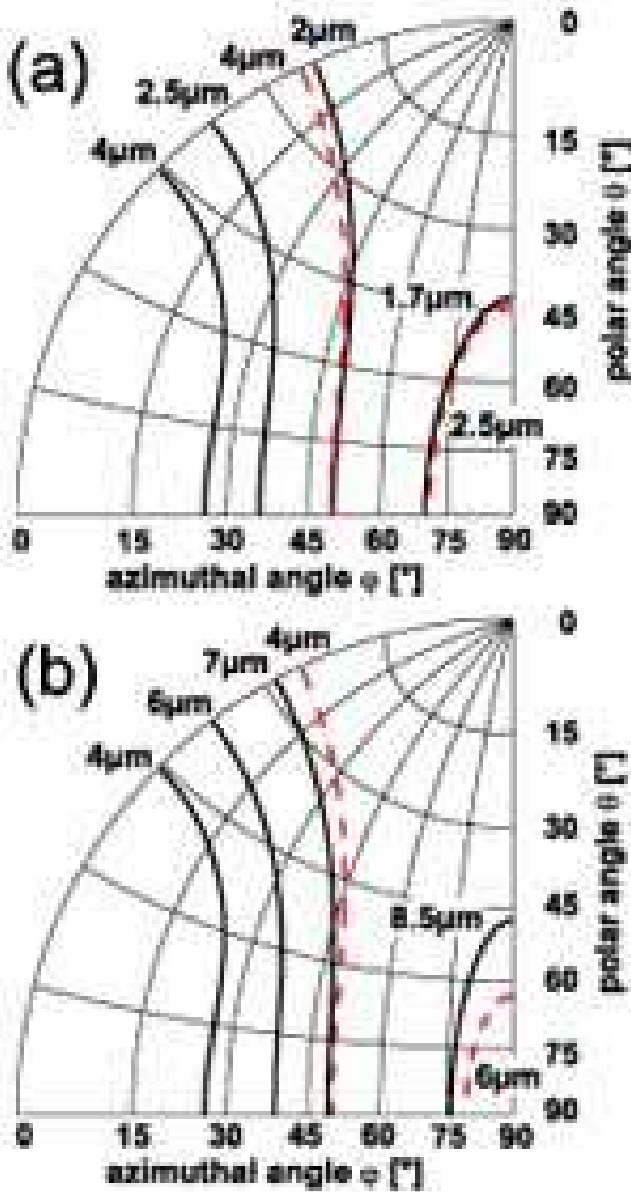


FIG. 15: (a)-(b): Stereographic projections of the SHG in the first octant of LIS calculated for wavelengths representative of the Hobden classes. Type-I (*ssf*) interaction (solid lines) and type-II (*fsf*, *sff*) interactions (dashed lines). The wavelength annotations refer to the fundamental ones.

to 1618 nm and up to 8710 nm is possible. Under the convention  $n_X < n_Y < n_Z$  the largest birefringence and consequently the shortest SHG wavelength is obviously achieved for type-I interaction and propagation along the Y-axis. However, in LIS when the Y-axis is approached in the principal planes X-Y or Y-Z  $d_{\text{eff}}$  for type-I interaction vanishes and this is true also for the limiting case of propagation along the Y-axis. This is the reason why propagation outside the principal planes can be used e.g. to shorten the SHG lower wavelength limit (Fig. 15). A

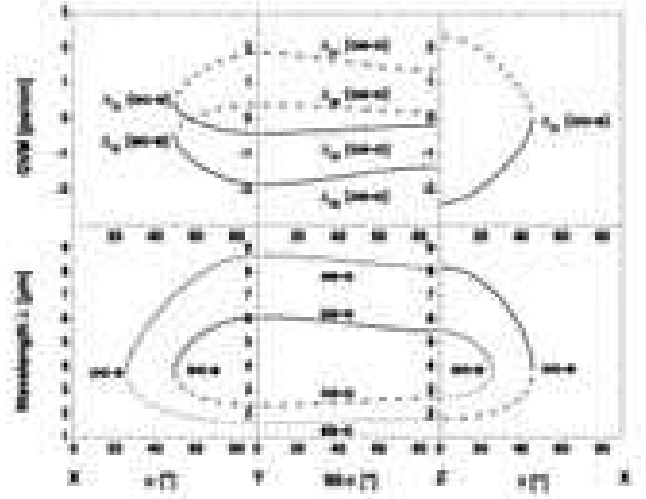


FIG. 16: SHG phase-matching in the principal planes of LIS. Thick lines in the lower part show fundamental wavelengths for which  $d_{\text{eff}} \neq 0$  and thin lines indicate cases where  $d_{\text{eff}}$  vanishes. The inverse group velocity mismatch ( $\Delta_{31} = v_3^{-1} - v_1^{-1}$  and  $\Delta_{32} = v_3^{-1} - v_2^{-1}$  where  $v_1, v_2, v_3$  denote the group velocities  $\partial\omega_i/\partial k_i$  at  $\lambda_1, \lambda_2$ , and  $\lambda_3$ ) is shown in the upper part only for the cases where  $d_{\text{eff}} \neq 0$ . The solid (dashed) lines correspond to the branch with longer (shorter) wavelengths.

similar situation is known to exist and has been experimentally verified in KTP [71].

It is seen from Fig. 16 that in the Y-Z plane the type-II interaction is quasi angle-noncritical (but wavelength-critical, see inset of Fig. 14) which ensures a large acceptance angle and a small walk-off angle. On the opposite, type-I interaction in the X-Z plane and type-II interaction in the X-Y plane have regions of quasi-wavelength-noncritical phase-matching ( $\partial\Phi/\partial\lambda \sim 0$ ) centered at 3889 nm and 3803 nm, respectively (Fig. 16, see also Fig. 14). Letting  $\Phi = \varphi$  or  $\theta$ , the walk-off angles in the upper panels of Fig. 17 are calculated using the simplified formula  $\tan \rho_i = [n_i^e(\Phi)]^{-1} \partial n_i^e / \partial \Phi$  valid for uniaxial crystals, where the subscript  $i = 1, 2, 3$  is associated with wavelength  $\lambda_i$  ( $\lambda_3^{-1} = \lambda_2^{-1} + \lambda_1^{-1}$ ) and  $n_i^e(\Phi)$  is the extraordinary index of refraction of the walking-off wave as given by the uniaxial analogy in the principal planes. We preserved its sign which is in accordance with the corresponding phase-matching angles i.e. a positive value of the walk-off means that the Poynting vector is at an angle larger than the phase-matching angle and vice-versa. Note that the walk-off is very similar for the two branches of the solution for phase-matching in all three principal planes. In the X-Y plane these branches and the two different walk-off parameters (we have here two extraordinary waves) are almost undistinguishable. The maximum walk-off amounts to  $\rho_3 = +1.15^\circ$  in the X-Z plane for SHG at 3889 nm.

The acceptance angle is evaluated from the phase velocity mismatch  $\Delta k(\delta\Phi)$  due to an angular deviation

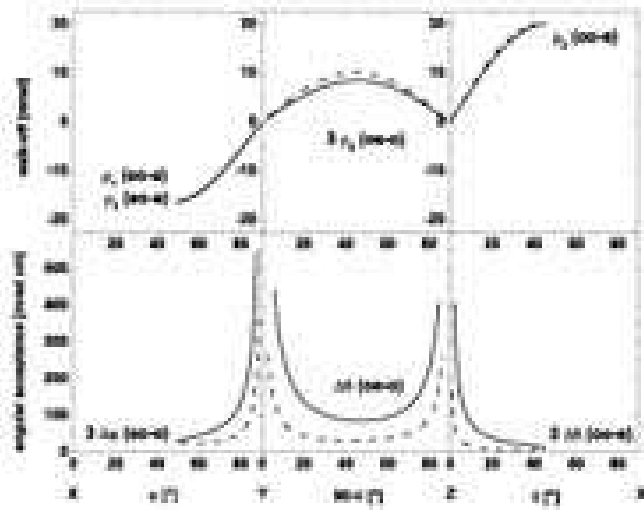


FIG. 17: SHG internal angular acceptance (bottom) and walk-off angles (top) in the principal planes of LIS. Thick solid lines correspond to the branches with longer wavelengths from Fig. 16 and thick dashed lines correspond to the branches with shorter wavelengths. Only the cases with  $d_{eff} \neq 0$  are included.

$\delta\Phi = \Phi - \Phi_{PM}$  of the wavevectors around the nominal phase-matched direction  $\Phi_{PM}$ . A Taylor expansion of  $\Delta k$  leads to

$$\Delta k(\delta\Phi) = \gamma_{CPM} \delta\Phi + \gamma_{NCPM}(\delta\Phi)^2 + \dots \quad (35)$$

where  $\gamma_{CPM} = [\partial(\Delta k)/\partial\Phi]_{\Phi=\Phi_{PM}}$  vanishes for non-critical phase-matching (NCPM, e.g. for  $\Phi = 0, 90^\circ$ ) and  $\gamma_{NCPM} = \frac{1}{2} [\partial^2(\Delta k)/\partial\Phi^2]_{\Phi=\Phi_{PM}}$ . The acceptance angle, defined as the bandwidth at FWHM of the  $\text{sinc}^2(\Delta k L/2)$  phase mismatch function, is given by  $\Delta\Phi = 2.784/|\gamma_{CPM}|L$  for a critical phase-matching (CPM), while for NCPM it is  $\Delta\Phi = |2.784/\gamma_{NCPM}L|^{1/2}$ . The lower panels of Fig. 17 display the acceptance angles (for a length  $L = 1$  cm) in the three principal planes. The acceptance curves, computed with  $\gamma_{CPM}$  only in the expansion (35), are interrupted near non-criticality at maximum values corresponding to the ones calculated for  $L = 1$  cm using  $\gamma_{NCPM}$  only. Although that type of presentation in Fig. 17 is not very accurate in these limits we still prefer it since it permits the results to be presented as scalable with respect to the crystal length  $L$  (simultaneous consideration of both derivatives would not allow this).

The experimental comparison of type-II SHG acceptance angles in the Y-Z and X-Y planes is shown with symbols in Fig. 18, for  $\lambda = 2590$  nm. The solid lines depict the plane-wave  $\text{sinc}^2(\Delta k L/2)$  phase-mismatch tuning functions computed with the first-order term in Eq.(35), with  $\gamma_{CPM}(\theta_{PM}) = (\pi/\lambda)[n_2^e \rho_2]_{\theta_{PM}} = 7.2 \times 10^{-3} \mu\text{m}^{-1}$  (type-II (o eo) SHG in the Y-Z plane) and  $\gamma_{CPM}(\varphi_{PM}) = (\pi/\lambda)[2n_3^e \rho_3 - n_1^e \rho_1]_{\varphi_{PM}} = 3.17 \times 10^{-2} \mu\text{m}^{-1}$  (type-II (e oe) SHG in the X-Y plane) [72].

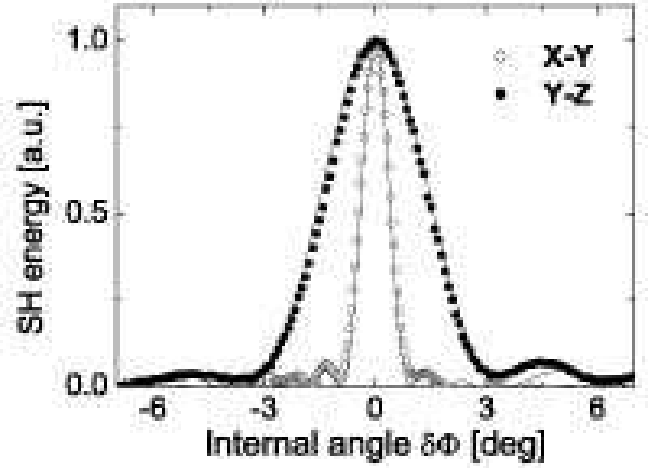


FIG. 18: Experimental angular tuning curves for type-II SHG of  $\lambda = 2590$  nm in the X-Y plane (at  $\Phi_{PM} \equiv \varphi_{PM} = 66.2^\circ$ , blank circles) and in the Y-Z plane (at  $\Phi_{PM} \equiv \theta_{PM} = 27.9^\circ$ , black circles). The larger acceptance angle in the Y-Z plane is due to the much smaller  $\Delta n_{Y-Z}$  birefringence as compared with  $\Delta n_{X-Y}$  (Fig. 12). The walk-off angles are  $\rho_1 \simeq \rho_3 = 12.2$  mrad (X-Y),  $\rho_2 = 2.8$  mrad (Y-Z). The crystal lengths are  $L = 6$  mm (sample LIS(1) used in X-Y) and  $L = 7$  mm (sample LIS(2) used in Y-Z plane), see Subsection IX A. The fundamental beam (diameter  $2w_0 \approx 2.6$  mm) is the idler output of a ns Nd:YAG-pumped LiNbO<sub>3</sub> OPO.

The perfect match of the theoretical curves with the experimental symbols highlights both the accuracy of the dispersion data and the single-domain feature of the samples used.

The chosen presentation of the inverse group velocity mismatch in the upper part of Fig. 16 is equivalent to the spectral acceptance  $\Delta\nu$  but contains the sign as an additional information. In the simplest cases of type-I SHG or degenerate DFG we have e.g.  $\Delta\nu L = 0.886/|\Delta_{31}|$  and the gain bandwidth in optical parametric amplification assuming a narrow-band pump wave at  $\lambda_3$  is inversely proportional to  $|\Delta_{21}| = |1/v_2 - 1/v_1|$ . The two parameters  $\Delta_{31}$  and  $\Delta_{32}$  vanish at 3889 nm in the X-Z plane which means large spectral acceptance for the SHG of short pulses where the second derivative of the wavevector-mismatch comes into play. The situation is different for type-II interaction in the X-Y plane: here  $\Delta_{32} = -\Delta_{31}$  at 3803 nm, at 2915 nm  $\Delta_{32}$  vanishes and at 4946 nm  $\Delta_{31}$  vanishes but in none of these cases an extremum of the spectral acceptance occurs because in type-II SHG of short pulses all three waves should be considered as broad-band. Thus long crystals can be used to increase the conversion efficiency for type-I SHG in the X-Z plane near 3889 nm even at femtosecond pulse durations. For type-II SHG of femtosecond pulses near 3803 nm in the X-Y plane the second harmonic will not be lengthened either because the temporal walk-off between the two polarizations of the fundamental wave will limit the interaction length, but consequently the conversion

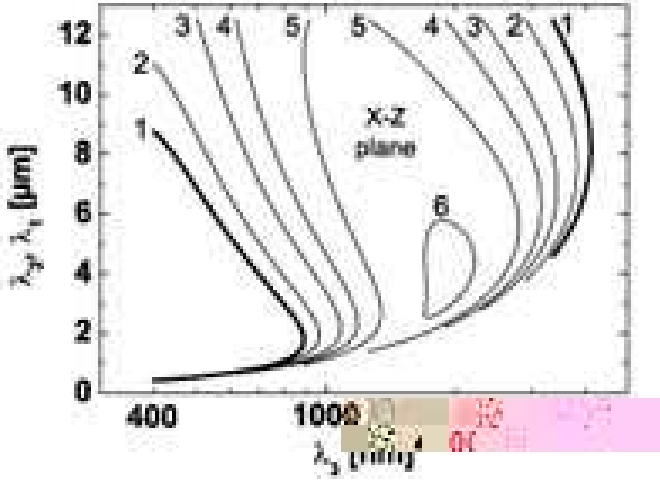


FIG. 19: Type-I (*ooe*) phase-matching for sum- and difference-frequency generation in the X-Z plane of LIS and several values of the polar angle :  $0^\circ$ -noncritical configuration (thick solid lines 1),  $20^\circ$  (lines 2),  $30^\circ$  (lines 3),  $35^\circ$  (lines 4),  $40^\circ$  (lines 5) and  $45^\circ$  (line 6). The wavelengths are such that  $\lambda_3^{-1} = \lambda_2^{-1} + \lambda_1^{-1}$ , with  $\lambda_1 > \lambda_2 > \lambda_3$ . The curves are terminated at the left and top side by the transparency range of the crystal.

efficiency will be low.

### C. Sum-and-difference frequency mixing

Type-I phase-matching in the X-Z plane for non-degenerate three-wave interactions (sum- and difference-frequency mixing as well as optical parametric generation, amplification and oscillation) is presented in Fig. 19 where two branches of the solution can be seen. The whole transparency range of LIS can be covered for  $0^\circ < \theta < 40^\circ$  in the X-Z plane but  $d_{\text{eff}}$  increases with the phase-matching angle  $\theta$ . Note that  $d_{\text{eff}} = 0$  in the noncritical ( $\theta = 0^\circ$ ) configuration and that the situation  $\theta > V_Z$  (Eq. 34) is never reached. At larger angles  $\theta$  we observe a retracing behavior in the left branch: e.g. in the case of OPO, one and the same pump wavelength  $\lambda_3$  corresponds to two pairs  $(\lambda_1, \lambda_2)$  of signal-idler wavelengths (curve 5). In this region the spectral acceptance is very large. Thus for  $\theta = 40^\circ$  (left branch of curve 5),  $\lambda_3 = 900$  nm and  $\lambda_2 = 1150$  nm all three group velocities are very close: at the point where  $\Delta_{31} = 0$  we have  $\Delta_{32} = 23$  fs/mm. This means that this phase-matching configuration is especially suitable for frequency conversion of femtosecond pulses. In the regions near the degeneracy points (SHG points) we have on the other hand  $\Delta_{21} = 0$  but the wave at  $\lambda_3$  can have in general a different group velocity. Such a regime is attractive for broadband parametric amplification in the field of a narrow-band pump pulse as in the case of chirped pulse optical parametric amplification [73]. In optical parametric amplifiers (OPA's) this advantage can be utilized, how-

ever, only in combination with a control of the spectral bandwidth through the seed signal. For femtosecond-laser based frequency metrology applications [74], this phase-matching when implemented in a synchronously-pumped OPO would provide a wide frequency comb grid spanning the  $10 - 12 \mu\text{m}$  region useful for high precision spectroscopy of spherical reference standard molecules. Increasing the phase-matching angle (curve 6 for  $\theta = 45^\circ$  in Fig. 19) the two branches merge into a closed contour and we approach the point where SHG phase-matching only for a single wavelength is possible (see Fig. 16) and all three group velocities are again very close but the tunability in that case is very limited.

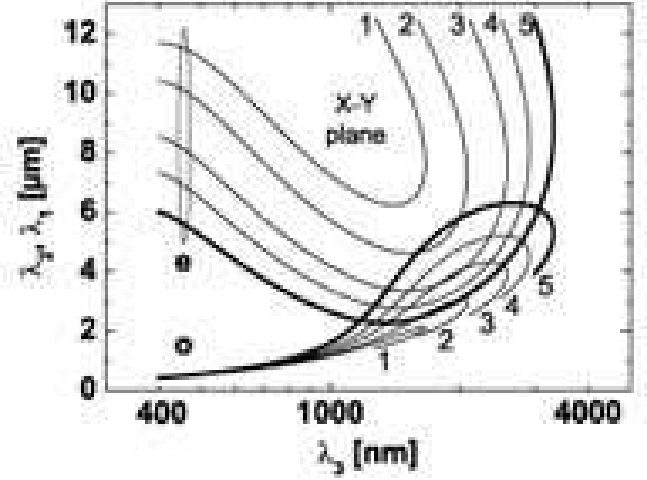


FIG. 20: Type-II (*eoe* and *oee*) phase-matching for sum- and difference-frequency generation in the X-Y plane of LIS and several values of the azimuthal angle  $\varphi$  :  $35^\circ$  (lines 1),  $40^\circ$  (lines 2),  $50^\circ$  (lines 3),  $60^\circ$  (lines 4) and  $90^\circ$ -noncritical configuration (thick lines 5). The curves are terminated at the left and top side by the transparency range of the crystal.

The curves for type-II phase-matching in the X-Y plane (Fig. 20) have a completely different shape. The two branches of the solution are represented by curves of opposite curvature which can cross at two points where phase-matching for degenerate DFG or SHG occurs. With decreasing phase-matching angle these branches separate and a single crossing point is reached (see the curves 3 for  $\varphi = 50^\circ$ ) which corresponds to the single SHG solution in Fig. 16. For yet smaller angles no crossing occurs and the degeneracy point is not reached. For all phase-matching curves presented we observe again a retracing behavior at longer  $\lambda_3$ : for each  $\lambda_3$  two couples  $(\lambda_1, \lambda_2)$  are phase-matched. At the point where these two pairs merge into one (at the maximum  $\lambda_3$  permitting phase-matching) the waves at  $\lambda_1$  and  $\lambda_2$  have equal group velocities and similarly to the case discussed for Fig. 19 broadband parametric amplification with a narrow-band pump wave can be realized. The deviation from the pump group velocity remains, however, essential. Thus e.g. at  $\varphi = 90^\circ$  and  $\lambda_3 = 3310$  nm,  $\Delta_{21} \simeq 0$  and  $\Delta_{31} \simeq \Delta_{32} \simeq -1.65$  ps/cm. Improved pump group-

matching at this point occurs when decreasing the phase-matching angle  $\varphi$  in accordance with Fig. 16.

Comparing Fig. 20 to Fig. 19 we note that at relatively short  $\lambda_3$  (e. g. 1064 nm) full tunability with a fixed crystal cut is achievable only in the X-Z principal plane. The group velocity mismatch depends on the specific wavelengths chosen. At  $\lambda_3 = 1064$  nm (a case interesting for parametric down-conversion)  $\Delta_{21}(X-Z) < \Delta_{21}(X-Y)$  up to  $\lambda_1 = 10 \mu\text{m}$ . This means that in this practical wavelength range type-II phase-matching in the X-Y plane is more advantageous for the development of narrow-band parametric generators or oscillators.

Our analysis of the phase-matching properties of LIS is just a first order approximation because it was based on the small signal limit where saturation is neglected. We considered also only collinear interactions. Non-collinear interactions attracted recently great interest because in addition to the possibility to improve the tunability, to spatially separate the beams, and to compensate for the spatial walk-off, this can considerably reduce the group velocity mismatch [75]. The latter is very promising for short pulse interactions. Explicit expressions for non-collinear phase-matching in the principal planes of a biaxial crystal can be found in Ref. [76] and calculations of non-collinear group velocity matching for arbitrary wave vector directions in Ref. [77].

## IX. SECOND-ORDER NONLINEAR COEFFICIENTS

There has been only one characterization study of the nonlinear properties of LIS made by Boyd *et al* in the early seventies [11]. The samples used then were of limited size and poor quality, and besides their results were derived only from non-phase matched SHG at  $10.6 \mu\text{m}$  (wedge technique). Further their measurements were performed relative to the nonlinearity of GaAs, that was several times corrected during the past years. So it is important to confirm or to correct these previous results using phase-matched second-order interactions on our mature and large enough samples.

The elements  $d_{ij}$  of the nonlinear tensor (27) have been determined from the measurement of the SHG efficiency of various laser sources, using either type-I or type-II interactions in the principal planes of LIS and also out of them. Two kinds of measurements have been performed: in one kind (Subsection A), the source is the idler output (in the range  $2.4 - 2.6 \mu\text{m}$ ) of a 12-ns pulsewidth, 10-Hz repetition rate, type-I LiNbO<sub>3</sub>-OPO [16]. Long samples were used and hence the residual absorption and the beam walkoff effect, as well as the focusing effects, have to be taken into account to derive the nonlinear coefficients. The second independent series of SHG experiments (Subsection B) used femtosecond pulses and very thin oriented samples. This allows to neglect the effect of absorption and beam walk-off and focusing effects, the data analysis in the low-depletion limit being

derived from the standard plane-wave SHG theory.

### A. Measurements based on Gaussian beam SHG theory

In order to remain in the low pump depletion limit, the peak on-axis fundamental intensity used was below  $10 \text{ MW/cm}^2$ , and the maximum idler energy of the LiNbO<sub>3</sub>-OPO was 10 mJ at  $\lambda = 2590$  nm. The spectral linewidth of the idler was below 15 GHz, and the transverse beam profile resembled a Gaussian. Three thick samples of different coloration (rose and yellowish) were used in conjunction with weak focusing producing Gaussian beam waist of either  $w_0 \sim 1 \text{ mm}$  or  $w_0 \sim 1.3 \text{ mm}$ . Sample LIS(1) was rose-annealed, cut at ( $\varphi = 66.5^\circ, \theta = 90^\circ$ ) for type-II (*oeo*) SHG in the X-Y plane, with dimensions  $4 \times 4 \times 6 \text{ mm}^3$  ( $L = 6 \text{ mm}$ ). Sample LIS(2) was yellowish (as-grown), cut at ( $\varphi = 90^\circ, \theta = 28^\circ$ ) for type-II (*oeo*) SHG in the Y-Z plane, with dimensions  $4 \times 4 \times 7 \text{ mm}^3$  ( $L = 7 \text{ mm}$ ). LIS(1) and LIS(2) were the same samples already used in Subsection VII A, see Fig. 14 and also Fig. 18. Sample LIS(3) had almost identical cut as LIS(1) ( $\varphi = 66^\circ, \theta = 90^\circ$ ), but was of yellowish tinge and with dimensions  $4 \times 4 \times 5 \text{ mm}^3$  ( $L = 5 \text{ mm}$ ). We have checked that, as the linear dispersion data, the nonlinear coefficients do not significantly depend on coloration when the additional absorption effect of the yellow samples was taken into account. For typical pump energy  $E_\omega = 1 \text{ mJ}$  and  $w_0 = 1.3 \text{ mm}$ , LIS(2) yielded  $E_{2\omega} = 2.5 \mu\text{J}$ , while LIS(1) yielded  $E_{2\omega} = 11 \mu\text{J}$  and LIS(3),  $E_{2\omega} = 7 \mu\text{J}$ . The difference between the efficiencies of LIS(1) and LIS(3) was mainly due to the much stronger second harmonic absorption of the latter ( $\alpha_{2\omega} = 0.27 \text{ cm}^{-1}$ ) [40]. For LIS(1), the residual fundamental and harmonic absorption amounted to  $\alpha_{\omega,2\omega} = 0.05 - 0.06 \text{ cm}^{-1}$  while for LIS(2)  $\alpha_{\omega,2\omega} \simeq 0.6 \text{ cm}^{-1}$  [40].

The measurements were performed relatively to a dual-band anti-reflection-coated KTP sample with  $L = 5.93 \text{ mm}$ , cut at ( $\varphi = 0^\circ, \theta = 56.4^\circ$ ) for SHG of  $\lambda = 2.53 \mu\text{m}$  in the X-Z plane. The measured nonlinear coefficient of KTP was  $d_{24} = 2.3 \pm 0.2 \text{ pm/V}$  [78] and served as a reference, without having to correct for dispersion since the measurement wavelength is almost identical to that used for LIS. We only corrected for the residual absorption loss ( $\alpha_\omega = 0.068 \text{ cm}^{-1}$  at  $2.59 \mu\text{m}$ ) of this KTP sample, due to OH<sup>-</sup> band [78]. According to the Gaussian beam SHG theory in the nanosecond pulse regime, the effective nonlinearity in the absence of depletion scales as [79]

$$d_{\text{eff}}^2 = \Gamma_{\text{SH}} \frac{\tau_\omega^2}{\tau_{2\omega}} \frac{c\epsilon_0 n^2 \lambda^3}{16\pi^2 L h} \quad (36)$$

where  $\Gamma_{\text{SH}} = E_{2\omega}/E_\omega^2$  is the pulse energy conversion efficiency (in unit of  $\text{J}^{-1}$ ),  $n$  is the average index of refraction at fundamental and harmonic wavelengths and  $h$  is the walkoff-focusing function that accounts for diffraction, absorption and beam-walkoff effects. The exact

expression of  $h$  for type-II interaction can be found in Ref. [80]. The second harmonic pulse duration was taken as  $\tau_{2\omega} \simeq \tau_{\omega}/\sqrt{2}$ . In the nanosecond regime and for the given crystal lengths, group-velocity mismatch can be safely neglected in SHG. The advantage of measuring the LIS coefficient relative to a reference material stems from the fact that it is neither necessary to evaluate the absolute energies nor to take into account the loss due to the numerous filter sets used to isolate the fundamental and second harmonic field, since from Eq.(36), the ratio of the two  $d_{\text{eff}}$ 's scales as

$$\frac{d_{\text{eff}}^2(\text{LIS})}{d_{\text{eff}}^2(\text{KTP})} = \frac{\Gamma_{\text{SH}}(\text{LIS})}{\Gamma_{\text{SH}}(\text{KTP})} \frac{n^2(\text{LIS})}{n^2(\text{KTP})} \frac{L(\text{KTP})}{L(\text{LIS})} \frac{h(\text{KTP})}{h(\text{LIS})}. \quad (37)$$

The efficiencies  $\Gamma_{\text{SH}}$  were derived from the linear fit of the plot of  $E_{2\omega}$  versus  $E_{\omega}^2$ , for fundamental energies ranging from 0 to 5 mJ [40]. The results of the data analysis, averaged over the two waist values, are the following:

$$d_{\text{eff}}[\text{LIS}(2)] = 1.36 (\pm 15\%) d_{\text{eff}}(\text{KTP}), \quad (38)$$

$$d_{\text{eff}}[\text{LIS}(1)] = 3.05 (\pm 15\%) d_{\text{eff}}(\text{KTP}), \quad (39)$$

$$d_{\text{eff}}[\text{LIS}(3)] = 3.15 (\pm 15\%) d_{\text{eff}}(\text{KTP}). \quad (40)$$

The rather large uncertainties are mainly due to the uncertainty in the absorption coefficients through the evaluation of the  $h$  focusing functions. Given that  $d_{\text{eff}}(\text{KTP}) = d_{24} \sin \theta$  ( $\theta = 58.7^\circ$  at  $\lambda = 2590$  nm), from (38) and (32) one derives  $d_{24}(\text{LIS}) = 5.73 \pm 20\%$  pm/V. The two last relations (39)-(40) were average to yield, using (31) and the determined value of  $d_{24}$ ,  $d_{15}(\text{LIS}) = 7.94 \pm 20\%$  pm/V. The ratio of the two nonlinear coefficients is hence found to be  $d_{24}/d_{15} = 0.72$ .

## B. Measurements based on femtosecond SHG

The SHG experiments with femtosecond pulses were performed also in the low depletion limit for the fundamental in order to avoid complications from saturation effects and spatial effects across the beam cross section. The coefficient  $d_{31}$  was estimated by type-I SHG in the X-Z plane from Eq.(33), once it was known it was used for the determination of  $d_{24}$  from type-II SHG in the X-Y plane using Eq.(31) and assuming Kleinman symmetry to hold (i.e.  $d_{15} = d_{31}$ ). Finally the diagonal element  $d_{33}$  was measured by type-I SHG outside the principal planes using Eq.(28) and the already determined off-diagonal components of the  $\mathbf{d}^{(2)}$ -tensor, again assuming Kleinman symmetry. Note that a similar strategy was used previously to determine  $d_{33}$  of KTP by phase-matched SHG [81] and as outlined there the error in the determination of this diagonal element is normally larger since it accumulates the uncertainties of the other coefficients. Alternatively the plane Y-Z could be used for determination of  $d_{24}$  as done in the previous subsection, however, the spectral tunability is very narrow in this principal plane (see Fig. 16) which is not adequate for measurements with broadband femtosecond pulses.

All three LIS samples used here were annealed and rose in colour, had an aperture of  $4 \times 5$  mm<sup>2</sup> and were 0.2 mm thick. They were cut at ( $\varphi = 0^\circ, \theta = 34^\circ$ ) [LIS(4)], ( $\varphi = 59^\circ, \theta = 90^\circ$ ) [LIS(5)], and ( $\varphi = 30^\circ, \theta = 44^\circ$ ) [LIS(6)], respectively. The small thickness allows to neglect absorption or scattering losses, the focusing effects and also spatial beam walk-off effects. This measurement was also relative and we used as a reference sample an AGS crystal with the same dimensions cut at  $\varphi = 45^\circ$  and  $\theta = 45^\circ$  for type-I SHG. In order to minimize the error originating from the still different group-velocity mismatch the pulsewidth at the fundamental was chosen relatively large (160 fs in all cases) since LIS samples with thickness less than 0.2 mm could not be prepared with sufficient quality. This pulsewidth corresponds to spectral bandwidths of 80-90 nm. For  $d_{36}$  of AGS we used the value of 13.9 pm/V [82] which was measured at a similar wavelength ( $\lambda = 2.53 \mu\text{m}$ ) and actually relative to  $d_{24}$  of KTP using the same value for the latter as in the previous subsection of the present work. In the plane wave approximation and having in mind the equal fundamental energy and crystal thickness,  $d_{\text{eff}}$  of LIS was determined simply from

$$\frac{d_{\text{eff}}^2(\text{LIS})}{d_{\text{eff}}^2(\text{AGS})} = \frac{E_{2\omega}(\text{LIS})}{E_{2\omega}(\text{AGS})} \frac{[1 - R(\text{AGS})]^3}{[1 - R(\text{LIS})]^3} \frac{n^3(\text{LIS})}{n^3(\text{AGS})} \quad (41)$$

where  $n^3$  is the product of the three refractive indices involved, and  $R$  takes into account the Fresnel reflections at the entrance surface (twice for the fundamental) and the exit surface (second harmonic).

The femtosecond source at 1-kHz repetition rate was a KTP-based OPA which was seeded by the frequency-doubled idler of a BBO-based OPA, both OPAs being pumped by the same 800 nm, 40 fs pump source (Ti:sapphire regenerative amplifier). The 3-mm KTP used in the OPA ensured sufficiently long wavelengths that cannot be achieved by BBO. Seeding by the frequency doubled idler of the BBO-OPA was preferred against seeding by the signal wavelength for two reasons: the signal wavelengths available from the BBO-OPA were not short enough to produce idler wavelengths above  $2.5 \mu\text{m}$  with the KTP-OPA, and frequency doubling in a 2-mm thick BBO crystal of the idler used for seeding resulted in temporal broadening and spectral narrowing which was a prerequisite to improve the accuracy. SHG was performed at 2330 nm with LIS(4), 2850 nm with LIS(5) and 2300 nm for LIS(6). In all cases more than  $5 \mu\text{J}$  at the fundamental were available so that it was possible to reliably measure the SHG with a large area pyroelectric detector even at low conversion efficiency. We established that up to a conversion efficiency of 20% (energy) into the second harmonic the result did not change. In the case of LIS(6) the polarization angle  $\delta$  was adjusted by a He-Ne laser monitoring the polarization rotation by the leakage through an analyser till an eigenmode was reached. No additional improvement of the SHG efficiency could be observed later by further alignment of this angle which was in good agreement with the calcu-

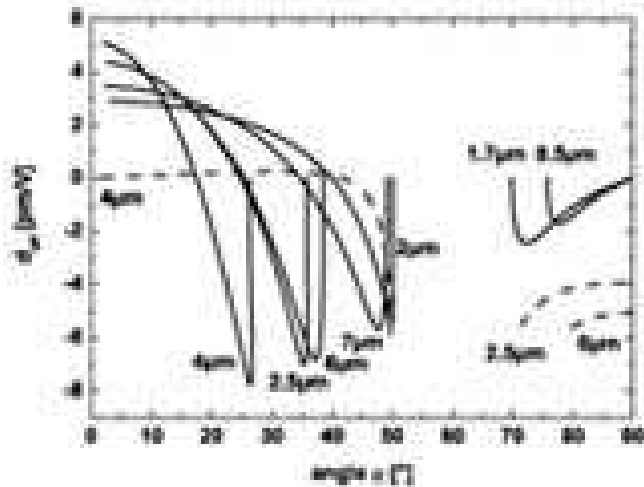


FIG. 21: Effective nonlinearity for type-I ( $ssf$ , solid lines) and type-II ( $fsf$ , dashed lines) SHG outside the principal planes of LIS as a function of the azimuthal angle  $\varphi$ . The labels indicate the fundamental wavelengths corresponding to the  $(\varphi, \theta)$  phase-matching loci of Fig. 15.

lated value from Eq.(30). Note that the dispersion of the optic axis angle  $V_Z$  (see Eq.(23) and Fig. 13) is relatively small and the deviation between visible (633 nm) and 2300 nm is less than  $2^\circ$ , so that the error originating from that effect is estimated to be less than 5%. The following results are values of the  $\mathbf{d}^{(2)}$  tensor components scaled to  $\lambda = 2300$  nm by using Miller's rule, i.e. assuming the same wavelength dispersion for the second-order nonlinearity as for the linear susceptibility,

$$d_{31}(\text{LIS}) = 7.25 (\pm 5\%) \text{ pm/V}, \quad (42)$$

$$d_{24}(\text{LIS}) = 5.66 (\pm 10\%) \text{ pm/V}, \quad (43)$$

$$d_{33}(\text{LIS}) = -16 (\pm 25\%) \text{ pm/V}. \quad (44)$$

The uncertainties are related to the group velocity mismatch and to the relatively large angular acceptance using thin samples. The above results are in very good agreement with the values obtained in the previous subsection by a completely different strategy and we also confirmed the different sign of the diagonal element  $d_{33}$  as established by Boyd *et al* [11]. Note that if the results from Ref. [11] which were obtained by non-phase-matched SHG are renormalized using a more recent value of  $d_{14}(\text{GaAs})=83$  pm/V [31] we arrive at  $d_{31} = 6.14$  pm/V,  $d_{32} = 5.31$  pm/V and  $d_{33} = 9.8$  pm/V. Having in mind the different wavelength (10.6  $\mu\text{m}$ ) used in Ref. [11], we obtain a good agreement within  $\pm 20\%$  with the present work for all three nonlinear coefficients.

### C. Effective nonlinearity of LIS

Once the nonlinear coefficients are determined the effective nonlinearity  $d_{\text{eff}}$  can be easily calculated in the

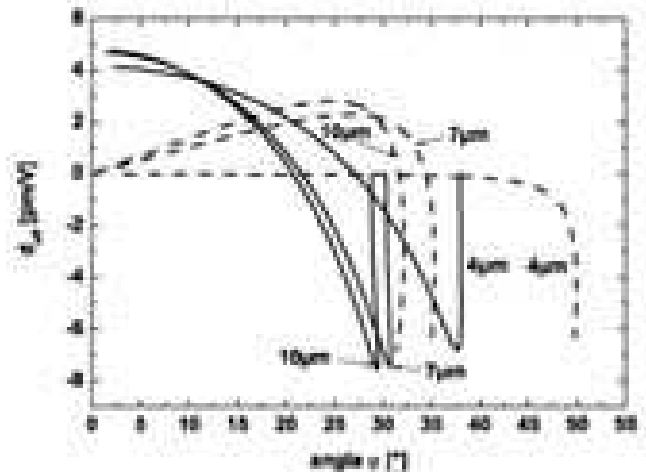


FIG. 22: Effective nonlinearity for type-I ( $ss-f$ , solid lines) and type-II ( $fs-f$ , dashed lines) down-conversion of  $\lambda_3 = 1064$  nm radiation (optical parametric generation, amplification or oscillation) to three selected idler wavelengths  $\lambda_1 = 4, 7, 10 \mu\text{m}$  for propagation outside the principal planes of LIS as a function of the azimuthal angle  $\varphi$ .

principal planes using Eqs. (31)-(33). The main conclusion drawn in Ref. [11], namely that the maximum  $d_{\text{eff}}$  is achieved in the X-Y plane where it is wavelength (angle) independent because of the similar magnitude of  $d_{24}$  and  $d_{15}$ , remains valid with our updated values for the  $d_{ij}$ 's. However, as already mentioned in subsection VIII B, interesting effects can be expected for propagation outside the principal planes. Fig. 21 shows the calculated  $d_{\text{eff}}(\varphi, \theta)$  for SHG using Eq. (28)-(29) with the nonlinearities obtained in the previous subsection and assuming for simplicity a constant angle  $V_Z = 66^\circ$  between the optic axes and the Z-principal axis (see Fig. 13) which for the wavelengths selected leads to only negligible errors. The fundamental wavelengths indicated in the figure correspond exactly to the phase-matching stereographic projections presented in Fig. 15 where the values for the polar angle  $\theta$  for the limiting cases  $\varphi = 0, 90^\circ$  can be seen. As can be seen from the figure for type-I SHG in the Hobden classes 9, 10, and 11 (see subsection VIII A and Ref. [65]) the improvement in  $d_{\text{eff}}$  when propagating outside the principal planes is not significant. On the contrary for Hobden class 13, it is definitely advantageous to use propagation outside the principal planes for maximum  $d_{\text{eff}}$  in type-I SHG. In type-II SHG the curves in Fig. 21 have a different character and maximum  $d_{\text{eff}}$  is achieved always in the X-Y plane which is advantageous as compared to type-II SHG in the Y-Z plane.

For various applications it is important to consider the down-conversion into the mid-IR of high power sources, e.g. lasers emitting at 1064nm (Fig. 22). For the selected wavelengths, the absolute negative extremum of the type-II curves which occurs in X-Y plane (right end, with  $d_{\text{eff}}^{\text{II}}(90^\circ, \varphi) \simeq -6.5$  pm/V) is larger than the ex-

tremum of the type-I curves in the X-Z plane (i.e. on the left side, with  $+4 < d_{\text{eff}}^{\text{I}}(\theta, 0^\circ) < 5 \text{ pm/V}$ ). Hence type-II interaction in the X-Y plane has larger  $d_{\text{eff}}$  than type-I interaction in the X-Z plane. However, propagation outside the principal planes allows to reach a slightly larger maximum  $-7 < d_{\text{eff}}^{\text{I}}(\theta, \varphi) < -7.5 \text{ pm/V}$  for type-I interaction which can be advantageous since other parameters like e.g. the spectral bandwidth can be better in type-I interaction. We believe the potential for future applications of LIS in the mid-IR is related also to the utilization of propagation schemes outside the principal planes.

## X. PARAMETRIC DOWN-CONVERSION IN LIS

### A. Femtosecond optical parametric amplification

As outlined in subsection II A LIS possesses the largest bandgap among all known mid-IR nonlinear crystals which results in an extremely low two-photon absorption near 800 nm. This unique feature can be utilized for the generation of femtosecond pulses in the mid-IR by down conversion of the most widely spread Ti:sapphire femtosecond laser systems operating near 800 nm. In Ref. [18] initial results were presented in the  $4.8 - 9 \mu\text{m}$  region but the gain and the output energy (2 nJ) were extremely low with a 1.5 mm thick LIS sample used as a seeded OPA. Here we report an improvement by a factor of about 50 for the output idler energy and an extension of the tunability range.

We applied for this experiment a cube of  $5 \times 5 \times 5 \text{ mm}^3$  of rose annealed LIS cut at  $\varphi = 41^\circ$  and  $\theta = 90^\circ$  for type-II interaction in the X-Y plane. The single-stage travelling-wave-type OPA was pumped by longer pulses than in Ref. [18] in order to increase the interaction length. We used 300 fs long pump pulses at 820 nm from a Ti:sapphire regenerative amplifier operating at 1kHz. The pulse lengthening was achieved by adjustment of the pulse compressor and the pump pulses were not bandwidth-limited (appr. three times the Fourier limit). About  $30 \mu\text{J}$  were used to generate continuum in a 2 mm thick sapphire plate and 5 different interference filters between 875 and 975 nm were used to select portions (of about 10 nm) of the continuum for seeding the OPA at the signal wavelength (Fig. 23). The seed pulse duration was measured by sum-frequency cross-correlation with a small fraction of the pump pulses in a 0.5 mm thick type-I BBO crystal and deconvolution yielded a pulse FWHM of the order of 400 fs (about 3 times above the Fourier limit). The OPA was pumped by  $150 \mu\text{J}$  and the pump beam parameters corresponded to a peak on-axis pump intensity of  $60 \text{ GW/cm}^2$ .

The mid-IR spectra depicted in Fig. 23 were recorded with a 0.5 m monochromator (150 gr/mm grating) and a liquid-N<sub>2</sub>-cooled HgCdTe detector. Tunability from 5 up to almost  $12 \mu\text{m}$  (i.e. the mid-IR cutoff wavelength of Fig. 3) could be demonstrated. From 8 to  $12 \mu\text{m}$  an

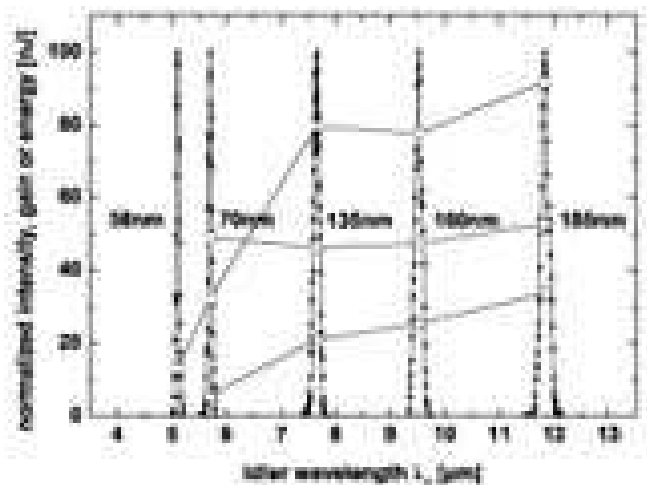


FIG. 23: Idler spectra (the labels indicate FWHM) that demonstrate the achieved tunability with the LIS-based OPA. The squares show the experimentally achieved output idler energy, the circles show the achieved (internal) signal gain, and the diamonds show the applied seed (signal) energy.

almost constant energy level exceeding 80 nJ could be achieved, despite the stronger absorption. This can be attributed to the lower group velocity mismatch at longer idler wavelengths [18] and also to the increasing seed level which effects compensate for the reduced transmission. The pulse duration of the idler pulses was estimated from sum-frequency cross-correlation with a 820 nm reference pulse in a 0.3 mm thick type-I AGS crystal in which the group mismatch between the two input pulses ranged from 715 fs/mm at  $\lambda_1 = 9.5 \mu\text{m}$  to 800 fs/mm at  $\lambda_1 = 6.5 \mu\text{m}$ . Fig. 24 shows the corresponding cross-correlation traces. The deconvolved pulse duration at

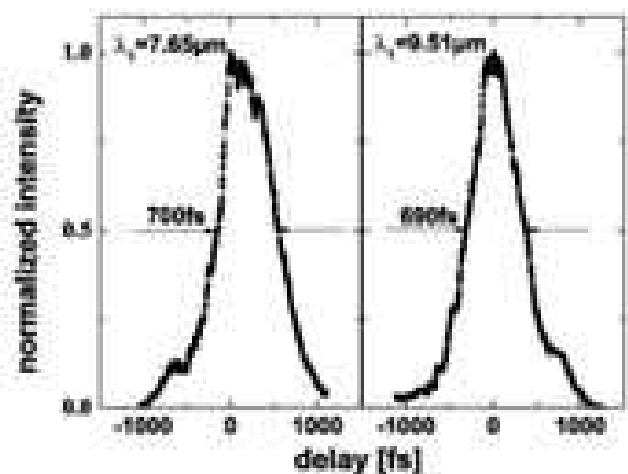


FIG. 24: Cross-correlation traces at two idler wavelengths obtained by sum-frequency mixing with a 820 nm, 300 fs reference pulse. The deconvolved Gaussian pulse durations (FWHM) are in both cases 575 fs.

7.65 and 9.51  $\mu\text{m}$  (585 fs in both cases) corresponds to bandwidth-limited Gaussian shaped idler pulses (time bandwidth product equal to 0.44).

Thus LIS is the only nonlinear crystal that permits the direct frequency conversion of short pulses from the 800 nm region to the mid-IR above  $\sim 5 \mu\text{m}$  in a *single step* extending the region covered by crystals like LiNbO<sub>3</sub>, KNbO<sub>3</sub> or KTP and its isomorphs [5]. The results in this section were obtained with amplified pump pulses at low (1kHz) repetition rates. Similar single stage down conversion of high repetition rate (100 MHz) Ti:sapphire femtosecond oscillators should be possible in synchronously pumped LIS-based OPOs.

A further potential application of LIS in femtosecond technology which relies on the extremely low two photon absorption near 800nm [18] is related to the generation of single (or sub-) cycle femtosecond pulses (both at low and high repetition rates) in the mid-IR by DFG of spectral components belonging to the same broadband spectrum of an ultrashort 800nm pulse [83]. If 15 fs long bandwidth-limited pulses centered at 800nm are used for this purpose the generated mid-IR wavelength is about 10  $\mu\text{m}$  at which wavelength a 30fs long pulse would possess only one optical cycle. The basic limitation in the conversion efficiency when using GaSe as previously demonstrated for this purpose [83] was its strong two-photon absorption at 800nm.

### B. Continuous-wave mid-IR DFG in LIS ( $5.5 < \lambda_1 < 11.3 \mu\text{m}$ )

We report in this subsection the first DFG experiments ever performed with LIS, whose partial results were already used to derive the accurate Sellmeier equations of Subsection VII A. Continuous-wave (cw) DFG is most suited for high-resolution spectroscopy in the mid-IR range: when both DFG laser sources have linewidths  $< 1 \text{ MHz}$  the mid-IR radiation at  $\lambda_1$  allows to perform sub-Doppler spectroscopy of heavy atmospheric molecules with only  $\sim 1 \mu\text{W}$  of power. Until now, cw DFG of two near-IR lasers for the generation of deep mid-IR light either used AGS [84, 85, 86] or GaSe [87]. We demonstrate that LIS is an alternative promising candidate, since we report cw parametric generation up to 11.3  $\mu\text{m}$  with an uncoated yellowish LIS sample of dimension  $5 \times 5 \times 10 \text{ mm}^3$  ( $L = 10 \text{ mm}$ ), cut in the X-Y plane for type-II (*eo*e) DFG at ( $\theta = 90^\circ$ ,  $\varphi = 42^\circ$ ).

Two tunable cw single-frequency Ti:sapphire lasers (Autoscan 899-29, Coherent Inc.) were used as difference-frequency mixing sources. The laser beams, orthogonally polarized, were collinearly focused onto the crystal with a 35-cm-focal length lens, yielding a nearly optimal  $w_0 = 55 \mu\text{m}$  waist for both pump wavelengths  $\lambda_3 < \lambda_2$ . The pump wavelengths were blocked after the sample by a 1-mm thick uncoated germanium (Ge) filter and the mid-IR radiation was detected by a calibrated liquid-N<sub>2</sub>-cooled HgCdTe photoconductive detector with

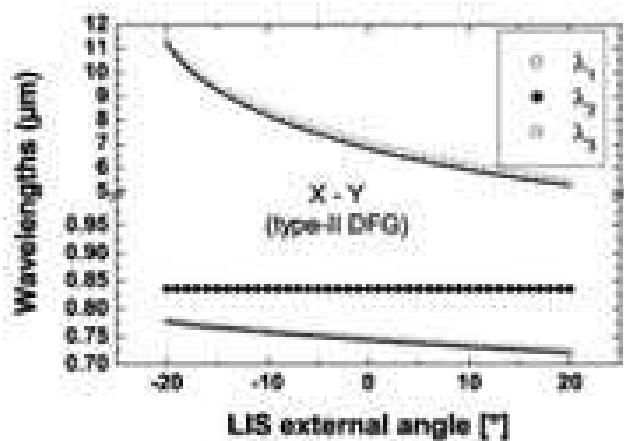


FIG. 25: Wavelength and angle tuning characteristics of type-II (*eo*e) DFG of two cw Ti:Sapphire lasers in LIS. The solid lines are calculated from the Sellmeier equations of Subsection VII A.

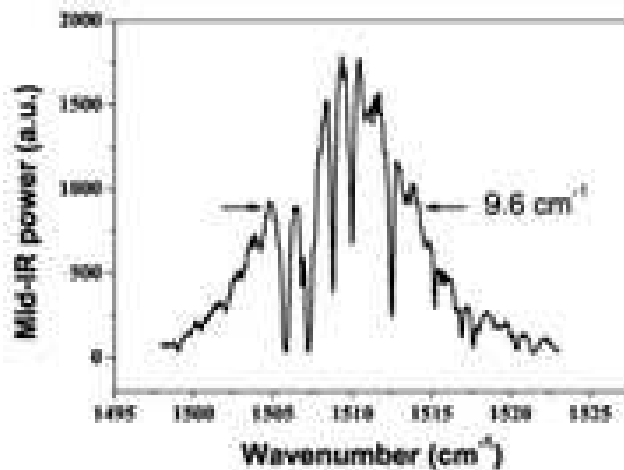


FIG. 26: Mid-IR DFG spectral tuning curve in pump tuning mode around  $\lambda_3 \simeq 765 \text{ nm}$ . The other wavelength was fixed at  $\lambda_2 = 865.3 \text{ nm}$ . In this frequency scan, we could observe atmospheric water vapor absorption lines in laboratory ambient air over 42.5-cm open path between the LIS crystal and the MCT detector.

a  $1 \times 1 \text{ mm}^2$  active area (EG&G, model J15D12). The detected voltage was amplified by a low-noise preamplifier and fed to a lock-in amplifier.

In Table V, we have already seen that at fixed  $\varphi = 42^\circ$ , wavelength tuning alone can cover only the 6.6 – 7  $\mu\text{m}$  range, limited by the tunability range of the Ti:sapphire lasers (from curves 2-3 of Fig. 20, a tunability range extending into the blue would be required to extend the DFG to  $\sim 10 \mu\text{m}$ ). Taking profit of angle tuning, mid-IR radiation was generated with broad wavelength tunability in the 5.5 – 11.3  $\mu\text{m}$  spectral region with combined pump laser wavelength ( $\lambda_3$ ) and crystal angle ( $\varphi$ ) tuning [85]: in Fig. 25 one Ti:sapphire laser was fixed at

$\lambda_2 \sim 836$  nm, and the other ( $\lambda_3$ ) was tuned from 724 to 778 nm. The solid lines are calculated phase-matching curves from Eqs.(20)-(22), highlighting the accuracy of the Sellmeier equations that were fitted using the fixed-angle DFG data of Table V.

Fig. 26 displays the mid-IR spectral tuning bandwidth around  $1510 \text{ cm}^{-1}$  ( $\lambda_1 \sim 6.6 \mu\text{m}$ ), when  $\lambda_2$  is set at 865.3 nm and  $\lambda_3$  is tuned around 765 nm, corresponding to a quasi-normal incidence phase-matching. A  $\Delta\bar{\nu}_1 \sim 10 \text{ cm}^{-1}$  ( $\bar{\nu} = 1/\lambda \equiv \nu/c$ ) FWHM spectral bandwidth is obtained, within which sharp atmospheric water vapor absorption lines can be observed. The FWHM plane-wave spectral acceptance for this pump tuning mode expresses as [4]

$$\Delta\nu_1 = 1.722 \frac{\pi}{L} \left[ \frac{\partial \Delta k}{\partial \nu_1} \right]_{\nu_1^{\text{PM}}}^{-1} \quad (45)$$

where  $\partial \Delta k / \partial \nu_1$  can be expanded, taking the constraint  $\nu_3 - \nu_2 = \nu_1$  into account, as

$$\begin{aligned} \frac{\partial \Delta k}{\partial \nu_1} &= \frac{2\pi}{c} \left[ n_3(\varphi) - \lambda_3 \frac{\partial n_3(\varphi)}{\partial \lambda_3} - n_1(\varphi) + \lambda_1 \frac{\partial n_1(\varphi)}{\partial \lambda_1} \right] \\ &\equiv \frac{2\pi}{c} \Delta_{31}. \end{aligned} \quad (46)$$

In Eq.(46), the angle-dependent indices are the extraordinary indices in the X-Y plane. From (45)-(46), the calculated spectral acceptance is  $\Delta\nu_1 = 214 \text{ GHz}$  ( $\Delta\bar{\nu}_1 \simeq 7.2 \text{ cm}^{-1}$ ) corresponding to a pump tuning over  $\Delta\lambda_3 = 0.42 \text{ nm}$ . The bandwidth broadening observed in Fig. 26 is attributed to the focused beam effect [88].

Let us note that despite the strong mid-IR absorption at  $11.3 \mu\text{m}$  (Fig. 3), we could still detect  $\sim 3 \text{ nW}$  mid-IR power for input powers  $P_3 = 200 \text{ mW}$  and  $P_2 = 265 \text{ mW}$ . This power is generated by the last exit layers of material. For the same incident powers, the detected power at  $\lambda_1 = 7 \mu\text{m}$  was  $P_1 = 33.5 \text{ nW}$ . The net conversion efficiency at this wavelength, corrected for all Fresnel optical loss, amounted to  $\Gamma = P_1/P_3P_2 \simeq 1.6 \mu\text{W}/\text{W}^2$ . Using the general focused-beam theory for DFG [88] that evaluates the focusing function  $h_{\text{DFG}}$  for type-II DFG for the given focusing parameters, walk-off value ( $|\rho_{1,3}| = 0.97^\circ$ ) and absorption loss ( $\alpha_3 \sim 0.15 \text{ cm}^{-1}$ ,  $\alpha_2 \sim 0.1 \text{ cm}^{-1}$ ,  $\alpha_1 \sim 0.05 \text{ cm}^{-1}$ ), we derive an effective nonlinear coefficient  $d_{\text{eff}}(7 \mu\text{m}) \simeq 5.3 \text{ pm}/\text{V}$ . This value is slightly lower than the calculated value using Eq.(31) and the determined values of  $d_{24}$  and  $d_{15}$  (Eqs.(43)-(42)),  $d_{\text{eff}} \simeq 6.55 \text{ pm}/\text{V}$ . The difference may arise from the residual atmospheric water absorption lines in this region.

## XI. LASER-INDUCED DAMAGE IN $\text{LiInS}_2$

### A. Photo-induced absorption and gray-tracking

Illumination with various laser sources resulted in the following photo-induced phenomena observed in LIS,

whose magnitude depends on wavelength and pulse duration:

1. Micro-cracking (at  $\lambda = 5 \mu\text{m}$  using femtosecond pulses from a free-electron laser [17]).
2. Dendrite structure formation (at  $\lambda = 1.079 \mu\text{m}$  using nanosecond pulses)
3. Photo-induced absorption (PIA) as grey-tracks (at  $\lambda = 0.8 \mu\text{m}$  using femtosecond pulses).

Optical damage of types 1 and 2 is irreversible, while PIA damage is to a certain extent reversible. It disappears at lower levels spontaneously after several hours of storage at room temperature or several minutes of illumination with  $\lambda > 500 \text{ nm}$ . The PIA was detected first in femtosecond OPA experiments with a 1.5mm thick LIS sample pumped by a 1kHz Ti:sapphire regenerative amplifier delivering pulses at 800nm with a duration of 200fs and energy of  $200 \mu\text{J}$  [18]. No surface damage was observed in these experiments up to a peak on-axis intensity of  $140 \text{ GW}/\text{cm}^2$ . In principle as with other materials optical damage in the femtosecond regime is expected to occur indirectly as a result of filamentation and self-focussing through higher-order nonlinear effects. These studies permitted to estimate only an upper limit on the nonlinear absorption losses at 800 nm which were independent of polarization and presumably caused by inclusions. They could not be fitted by a TPA process and the estimated upper limit of TPA is  $\beta_{\text{TPA}} \sim 0.04 \text{ cm}/\text{GW}$  at 800 nm [18] which was about 100 times lower than the  $\beta_{\text{TPA}} = 3.5 - 5.6 \text{ cm}/\text{GW}$  (depending on the polarization) fitted for a 0.3mm thick AGS crystal under identical conditions, which is a manifestation of the advantages of LIS related to its larger bandgap. An updated value for the upper TPA limit that we derived for a different sample, namely the LIS crystal used in Subsection X A, is only slightly higher:  $\beta_{\text{TPA}} = 0.05 \text{ cm}/\text{GW}$ . Note that recent TPA measurements on  $\text{KNbO}_3$  (which belongs to the same class mm<sup>2</sup>) at 846 nm using a 5-mm thick sample phase-matched for cw blue light generation yielded a TPA magnitude ( $\beta_{\text{TPA}} = 3.2 \text{ cm}/\text{GW}$ ) of the same order as that for AGS [89]. In the experiment of Ref. [18] the gray tracks formation (leading to PIA) was attributed to non-phase-matched SHG and residual blue light absorption, i.e. this damage mechanism is only indirectly related to the high intensity of the femtosecond pulses that resulted in higher probability for unwanted SHG. Subsequently differential absorption (before and after illumination) was measured that had a magnitude reaching several  $\text{cm}^{-1}$  and extended from 400 nm up to the near-IR ( $1 - 2 \mu\text{m}$ ) [90]. Well pronounced maxima of this absorption were observed at 430 nm and 650 nm. This photochromic induced-absorption is similar to the so-called Blue-Induced Infrared Absorption (BLIIRA) observed in SHG experiments with  $\text{KNbO}_3$ , for which an increased near-IR absorption coefficient ( $0.011$  to  $0.056 \text{ cm}^{-1}$  depending on the sample and corresponding to 2.5 to 9 times the usual linear absorption) at the fundamental

wavelength of 860 nm was detected with 100 mW of blue SH power ( $30 \text{ kW/cm}^2$ ) generated with a Ti:sapphire laser [91]. The BLIIRA damage was also reported to be reversible, after a few hours of relaxation at room temperature, and could be minimized by heating the crystal or pumping at longer wavelengths [92].

In order to understand the origin of the PIA in LIS, we proceeded with a direct illumination of LIS samples at  $300 < \lambda < 450 \text{ nm}$  using a 1 kW Xe lamp filtered through a monochromator for  $\sim 10$  minutes: The same coloration effect was indeed obtained, with a maximum effect at 360 nm excitation and vanishing at wavelengths shorter than 300 nm. Thus the PIA observed in the OPA experiments is really caused by linear absorption of non-phase matched blue SHG by point defects present in the lattice. In line with the photo-induced signal in absorption spectra (see Fig.3 in Ref. [90]), a complicated system of lines appears in the Electron Spin Resonance (ESR) spectrum. Analysis of the angular dependence allowed us to reveal the superposition of two spectra related to different paramagnetic defects. One of them has a spin  $S = 1/2$  and an anisotropic  $g$ -factor with the following principal values of the  $\mathbf{g}$ -tensor:  $g_1 = 2.160$ ,  $g_2 = 2.023$ ,  $g_3 = 2.023$ . This spectrum is associated with a center of axial symmetry with  $g_1$ , directed along the In-S bond and is related to sulfur  $\text{S}^-$  ion in a regular site. The second spectrum comprising a broad enough line at  $H \sim 3300 \text{ Gauss}$  ( $g = 2.0024$ ) is associated with  $\text{Li}^0$ .

The interpretation of these results is the following. At short-wavelength excitation ( $\lambda < 450 \text{ nm}$ ) the following recharge process occurs in LIS:



Such excitation produces free charge carriers which are captured in some deep traps and can be released at  $\lambda > 500 \text{ nm}$  illumination. We established that the gray track formation is maximized for excitation near 360 nm but dropped by one order of magnitude at 420 nm, which means that in OPO/OPA experiments it can be reduced by using slightly longer pump wavelength  $\lambda_3$ . Note that the same process also takes place at x-ray irradiation, which is used for crystal orientation when fabricating optical elements: some darkening occurs sometimes in the bulk sample during this operation. The PIA magnitude was found to be dependent on the LIS composition [93]: The effect is minimum in the case of nearly stoichiometric composition. The PIA was also found to be much more pronounced in LIS than in LISe. A detailed analysis of thermo-luminescence in LIS, ESR studies and the role of point defects in the PIA phenomenon will be given elsewhere.

### B. Optical damage threshold measurements at 1064 nm

Systematic optical damage threshold measurements were performed with Nd:YAG lasers at 1064 nm - i.e.

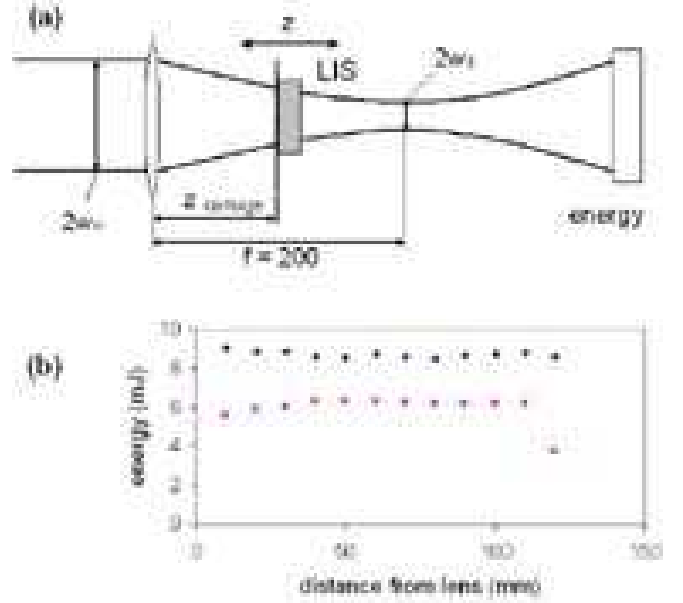


FIG. 27: (a): Experimental configuration for damage threshold measurements. (b): Measured pulse energy with crystal inserted (squares) and without it (diamonds). The drop in transmitted energy (last square) indicates damage formation.

well within the clear transmission range and far from the TPA region - with the experimental arrangement shown in Fig. 27. Initial measurements with a 6 W cw focused Nd:YAG laser beam failed to produce measurable damage, and subsequent measurements were performed with a pulsed laser. By varying the excitation current, the pulse energy could be varied between 6 mJ and 25 mJ at a repetition rate of 10 Hz and a pulse width of about 10 ns. The collimated Gaussian beam with a beam radius of  $w_{in} = 1.47 \text{ mm}$  was focused with a 200 mm focal length lens to produce a beam waist with a radius of  $w_0 = 46 \mu\text{m}$ . The crystal used was the A1 sample with dimensions  $4 \times 5 \times 5 \text{ mm}^3$  ( $\theta = 90^\circ$ ,  $\varphi = 24^\circ$ ) already used for linear absorption measurements (Subsection III A and Table I). It was mounted on a  $xyz$  translation stage which

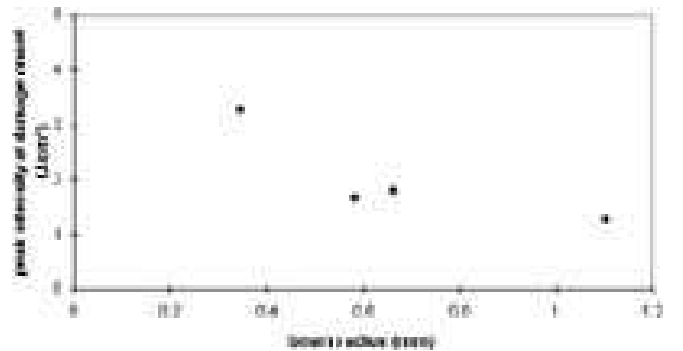


FIG. 28: Damage threshold, expressed as fluence, versus beam radius at the crystal surface.

could be moved along the laser beam over a distance extending from the lens to the focus location. The corresponding fluences ranged from  $0.19 \text{ J/cm}^2$  to  $752 \text{ J/cm}^2$ , and by using different pulse energies, the same fluence could be sustained over a range of spot radii. The Gaussian character of the beam was verified, and the beam radius measured by the knife-edge technique.

The onset of radiation damage was determined from the observed sudden drop in the transmitted signal as shown in Fig. 27. At each experimental point ( $z$ -value), the crystal was inspected visually in a low-power microscope, and the drop in transmission was found to correlate with the onset of visible damage at the surface. By performing experiments with different pulse energies it was found that the damage threshold, expressed in  $\text{J/cm}^2$ , tends to decrease with increasing spot size as seen in Fig. 28. Although the amount of data is too limited to warrant a detailed analysis, it suggests a levelling off at about  $1 \text{ J/cm}^2$  at large spot sizes (e.g. a peak intensity threshold of  $100 \text{ MW/cm}^2$ ), and this value agrees well with the value  $1.1 \text{ J/cm}^2$  reported by Knippels *et al.* at a wavelength of  $5 \mu\text{m}$  [17]. The observed dependence in Fig. 28 is understandable in view of the fact that as the spot size increases, it becomes increasingly difficult for heat generated at the centre to diffuse to the unexposed regions of the crystal.

The visual appearance of the damage is illustrated in Fig. 29, where the  $z$ -scan sequence shown in the lower part of Fig. 27 corresponds to the uppermost spot of the picture. In Fig. 27, the initial increase of transmitted energy reflects the fact that the center of the beam is too close to the edge to allow the entire beam to be intercepted by the crystal when the beam radius is largest. In some cases damage was found to extend into the interior of the crystal, as seen at the lower spot in Fig. 29.

These damage properties should be discussed in comparison with available damage data on AGS or AGSe. For AGS under cw pumping the onset of thermal lensing has been previously evaluated at  $\sim 11 \text{ kW/cm}^2$  from a cw AGS doubly resonant OPO containing  $\sim 3 \text{ W}$  of circulating power at  $1.26$  and  $2.52 \mu\text{m}$  focused to a waist of  $w_0 = 90 \mu\text{m}$  [8, 9]. The cw damage threshold value is actually unknown, but is estimated to occur in the range  $\sim 20 - 40 \text{ kW/cm}^2$  [36], despite a report that  $3.5 \text{ W}$  of cw Nd:YAG radiation focused to a waist of  $20 \mu\text{m}$  ( $280 \text{ kW/cm}^2$ ) did not damage an AGS sample [94]. For AGSe, the measured damage threshold at  $9 \mu\text{m}$  (cw  $\text{CO}_2$  laser) was ascertained to be  $5 - 22 \text{ kW/cm}^2$  [95], corroborating that chalcopyrites display extremely low cw damage threshold. The fact that at  $6 \text{ W}$  -pumping at  $1064 \text{ nm}$ , focused down to  $w_0 = 40 \mu\text{m}$  no visible damage was observed in the LIS sample sets the cw damage threshold to a lower limit of  $> 120 \text{ kW/cm}^2$ . The 5 times larger thermal conductivity of LIS as compared to AGS certainly favors the use of LIS in intra-cavity cw applications. Under similar nanosecond pulsed regime, however, the  $\sim 1 \text{ J/cm}^2$  damage threshold measured with LIS is comparable to the threshold found for AGS or AGSe [96, 97].

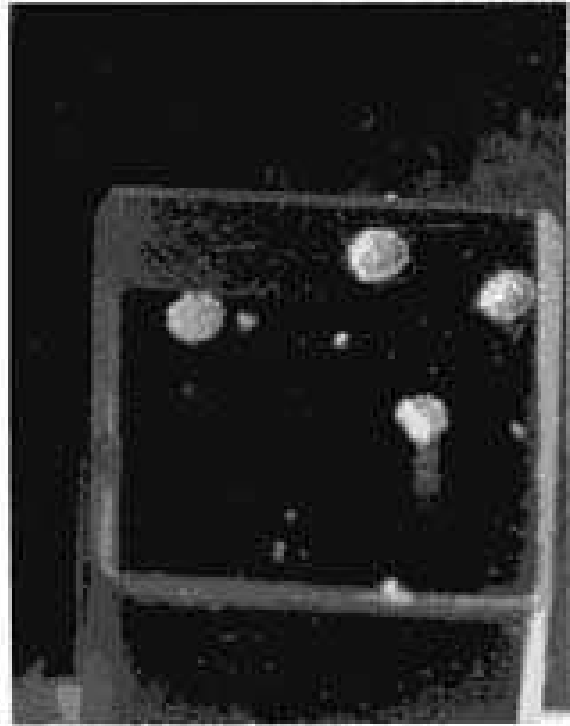


FIG. 29: Photograph of the A1 sample from Subsection III A showing the visible appearance of radiation damage spots. We emphasize the *bulk* feature of the damage on the lowest spot.

Independent measurements under identical experimental conditions at longer wavelengths ( $9.55 \mu\text{m}$ ) with  $30 \text{ ns}$  long pulses yielded damage thresholds of  $6.5 \text{ J/cm}^2$  for LIS [60] and  $5.5 \text{ J/cm}^2$  and  $4.2 \text{ J/cm}^2$  for AGS and AGSe, respectively [98].

From these preliminary damage threshold investigations, it is premature to assess whether the damage mechanisms are due to native point defects or are intrinsic to the compound. Considering the current state-of-the-art of residual absorption on this compound, one may expect that with an improvement in residual transparency and a better control of the growth parameters toward the production of stoichiometric material, the above damage threshold values can be improved.

## XII. IS LIS RELATED TO FERRO-ELECTRICS?

In contrast with the chalcopyrites, LIS and LISe are pyroelectric as the orthorhombic symmetry oxides (KTP isotypes) belonging to the same  $mm2$  point group. The spontaneous polarization is due to the fact that in each bipyramid formed by two adjacent tetrapores (Fig. 2) only one is occupied by a  $\text{Li}^+$  cation. The other one is empty, which corresponds to a negative effective charge. An intriguing issue, which has not still received a def-

inite answer, is whether such Li-chalcogenides can be related to ferroelectric materials, i.e. if it is possible to invert their spontaneous polarization along the polar  $c$ -axis. In their short note [55], Negran *et al* concluded that LIS and LISe do not display a para-to-ferroelectric phase transition from the absence of a sudden anomalous rise in the record of the pyro-electric current versus temperature. This is not surprising because of the screening effect of the high ionic conductivity of Li. They measured a pyroelectric coefficient  $p^\sigma(300K) = 2.6 \times 10^{-10} \text{C}/(\text{cm}^2 \cdot \text{K})$ . A more recent and reliable measurement of the pyro-electric coefficient performed with our rose samples yielded a 2.3 times higher value  $p^\sigma(300K) = 6.0 \times 10^{-10} \text{C}/(\text{cm}^2 \cdot \text{K})$  [58], which is 5 times smaller than the value for KTP [99]. In contrast with Negran *et al*'s report, a strong increase of the pyro-current slightly above room-temperature, preceded by a sharp current spike, was noticed but this increase was attributed to space charge relaxation of the thermally-activated  $\text{Li}^+$  cations [58].

The issue about whether Li-chalcogenides are (or are not) related to ferroelectrics is of utmost importance, considering their deep mid-IR transparency which would allow to fabricate quasi-phase matched periodically-poled structures for wavelengths longer than  $\sim 4-5 \mu\text{m}$ , which is the current limitation of oxide-based ferroelectrics such as  $\text{LiNbO}_3$  or  $\text{KNbO}_3$ . The measurement of the Curie temperature (a temperature at which the material tends to lose its spontaneous polarization), the study of its dielectric conductivity versus an applied ac electric field in order to reveal a dielectric hysteresis loop (and the value of the coercive field) have to be performed to answer to the question. Future investigations will be aimed at this issue.

Nevertheless, we have attempted to invert the spontaneous polarization by use of an external electric field. We tried to invert domains in 0.5 mm thick  $c$ -cut LIS plates by using standard methods developed for the fabrication of PPLN for quasi-phase-matching [100]. A periodic structure of photoresist with a periodicity of  $\Lambda = 30 \mu\text{m}$  was lithographically formed on the  $+c$  surface of the crystal. Silicon O-rings with a diameter of 4 mm on each surface fixed the crystal between two acrylic glass plates.

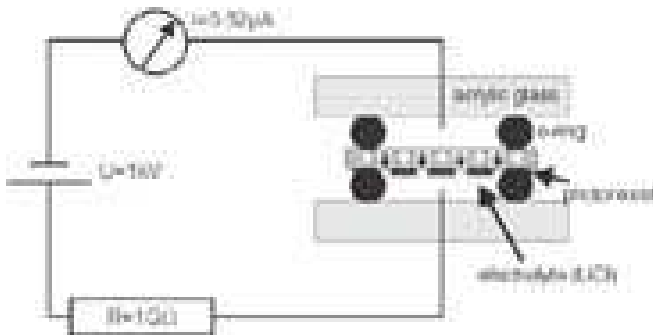


FIG. 30: Experimental setup for periodic domain inversion.

A solution of  $\text{LiCl}$  in water was used to establish the electrical contact between the power-supply and the crystal (see Fig. 30). An electrical resistor in the circuit limited the current. An oscilloscope measured the voltage and the current.

Because the coercive field - if any - is unknown, rectangular pulses of different voltages from 200 V to 6.4 kV were applied to the crystal using a resistor of  $1 \text{ G}\Omega$ . Even at the lowest voltage a current was measured. At a voltage of 1 kV the current was  $0.52 \mu\text{A}$ . The dependence of the voltage on the current was linear and the current did not terminate after a time when the whole crystal should be domain-inverted. This implies that the measured current does not result from domain switching but from ionic conductivity of the  $\text{Li}^+$  ions, confirming the results of the pyro-electric coefficient measurements [58]. From our measurements we estimate a value for the conductivity of  $\sigma_Z = 4.3 \times 10^{-10} \Omega^{-1} \text{cm}^{-1}$ . Etching of the crystal in a mixture of ethanol and  $\text{HNO}_3$  did not reveal any periodic domain structure on the crystal surface. So far, we were not able to obtain inverted domains.

In parallel to the afore-mentioned ferroelectricity studies, we plan in the future to perform *ab initio* low-temperature-poling of LIS, a method which was developed for periodic domain reversal in KTP, which also exhibits a high ionic conductivity of the  $\text{K}^+$  ion at room temperature [101]. Cooling the crystal down to temperatures of 170 K reduces the conductivity in KTP by a factor of  $10^5$ . This possibly could work for LIS as well. Further, the conductivity is expected to be lower in future crystals with a composition close to stoichiometry. In the case of  $\text{LiNbO}_3$  or  $\text{LiTaO}_3$ , the coercive field is much lower for stoichiometric crystals as compared with congruent material [102, 103]. If similar effects would occur in LIS, this would be an additional advantage.

Given the varying stoichiometry of the LIS samples currently produced [15], the presence of point defects and the high ionic conductivity due to Li ions, the failure of the poling attempts is not quite surprising. It is still premature to conclude on the ferroelectricity issue, and further systematic investigations for a para-electric to ferro-electric phase transition are still required.

### XIII. CONCLUSIONS

We have characterized the main physical properties of the newly emerging lithium thio-indate chalcogenide semi-conductor that are relevant for nonlinear applications from the visible down to the deep mid-IR. Table VII summarizes these properties, as well as those determined in previous works.  $\text{LiInS}_2$  or LIS can now be considered as a mature compound and its future widespread use in nonlinear devices should refine all the data collected from this investigation campaign.

Among its most relevant advantages over the existing mid-IR crystals, one may quote its excellent thermal stability and high damage threshold suitable for high power

TABLE VII: Summary of the main physical properties of LiInS<sub>2</sub>.

Summary of the main physical properties of LiInS <sub>2</sub> .	
<b>CRYSTALLOGRAPHIC DATA</b>	
Structure type	Wurtzite-type ( $\beta$ -NaFeO <sub>3</sub> structure)
Symmetry, point group	Orthorhombic, mm2 (negative biaxial)
Space group	Pna2 <sub>1</sub>
Lattice parameters (Å)	$a = 6.878$ ; $b = 8.033$ ; $c = 6.462$ [15]
Principal axes assignment	$(X, Y, Z) \longleftrightarrow (b, a, c)$
Density (g/cm <sup>3</sup> )	3.54
<b>OPTICAL PROPERTIES</b>	
Optical transmission ( $\mu\text{m}$ )	0.34 - 11.5
Bandgap energy ( $T = 300$ K) (eV)	3.55 ( $E \parallel c$ ); 3.61 ( $E \parallel b$ ); 3.58 ( $E \parallel a$ ) [15]
Indices of refraction at $T = 20^\circ$ :	
$\lambda = 0.532\mu\text{m}$	$n_X = 2.2413$ ; $n_Y = 2.2824$ ; $n_Z = 2.2991$
$\lambda = 1.064\mu\text{m}$	$n_X = 2.1288$ ; $n_Y = 2.1645$ ; $n_Z = 2.1734$
$\lambda = 10.6\mu\text{m}$	$n_X = 2.0200$ ; $n_Y = 2.0566$ ; $n_Z = 2.0595$
Optical axis angles ( $0.35\mu\text{m} < \lambda < 11.5\mu\text{m}$ )	$55^\circ < V_Z < 80^\circ$
Birefringence walkoff at 1064 nm (mrad)	$\rho_{X-Y} = 14.7$ ; $\rho_{X-Z} = 20$
SHG fundamental wavelength range (nm)	1618 - 8710
Thermo-optic coefficients ( $10^{-5}/^\circ\text{C}$ ) at 1064 nm, $T = 20^\circ\text{C}$	$dn_X/dT = 3.72$ ; $dn_Y/dT = 4.55$ ; $dn_Z/dT = 4.47$
Absorption coefficient at $1.064\mu\text{m}$ (cm <sup>-1</sup> )	$\alpha \leq 0.04$
Laser damage threshold:	
• surface, at 10 ns, $f = 10$ Hz, $\lambda = 1.064\mu\text{m}$	1.1 J/cm <sup>-1</sup>
• bulk, at 500 fs, $f = 25$ MHz, $\lambda = 1.064\mu\text{m}$	> 6 GW/cm <sup>2</sup> [17]
• surface, at 200 fs, $f = 1$ kHz, $\lambda = 0.8\mu\text{m}$	> 140 GW/cm <sup>2</sup> [18]
Two-photon absorption at $0.8\mu\text{m}$ (cm/GW)	$\beta_{\text{TPA}} \leq 0.04$
Nonlinear optical coefficients (pm/V)	
• by cw SHG at $2.5\mu\text{m}$	$d_{15} = 7.9(\pm 1.6)$ ; $d_{24} = 5.7(\pm 1.2)$
• by femtosecond SHG at $2.3\mu\text{m}$	$d_{31} = 7.2(\pm 0.4)$ ; $d_{24} = 5.7(\pm 1.1)$ ; $d_{33} = -16(\pm 4)$
<b>THERMAL PROPERTIES</b>	
Melting point ( $^\circ\text{C}$ )	$T_{\text{melt}} \sim 1000$
Thermal expansion at $T = 20^\circ$ ( $10^{-5}/^\circ\text{C}$ )	$\alpha_X = +1.64$ ; $\alpha_Y = +0.90$ ; $\alpha_Z = +0.68$
Specific heat (J/mole/ $^\circ\text{C}$ )	$C_p = 99$
Thermal conductivity (W/m/ $^\circ\text{C}$ )	$K_X = 6.2$ ; $K_Y = 6.0$ ; $K_Z = 7.6$
<b>ELECTRICAL PROPERTIES</b>	
Pyroelectric coefficient at $T = 300$ K ( $\mu\text{C}/\text{m}^2\text{K}$ )	2.6 [58]
Pure electro-optic coefficients (pm/V)	$r_{13} = 1.0$ ; $r_{23} = 0.4$ ; $r_{33} = -1.3$
Piezo-electric coefficients (pm/V)	$\bar{d}_{31} = -5.6$ ; $\bar{d}_{32} = -2.7$ ; $\bar{d}_{33} = +7.5$
Electric conductivity ( $\Omega^{-1}\text{cm}^{-1}$ )	$\sigma_Z = 4.3 \times 10^{-10}$

laser applications and its extremely extended phase-matching capabilities (over its whole transparency range) using either type-I or type-II interactions in or out-of principal planes. Such an extended phase-matching capability is still compatible with low birefringence walkoff angles. LIS is the only existing material for direct down-conversion from the near-IR to the deep mid-IR up to  $12\mu\text{m}$ , owing to its highest bandgap energy. Its high effective nonlinearity of  $\sim 7$  pm/V (slightly lower than that of the chalcopyrite crystals) is substantially higher than that of the oxides of the KTP family and is almost constant for type-II interaction in the azimuthal principal plane. We have shown that LIS should be very promising for the frequency down-conversion of femtosecond laser

sources. We have also enlightened its favorable properties as a crystal host either for laser action up to  $\lambda = 6\mu\text{m}$  using active rare-earth ion doping, or for self down-conversion medium provided that the doping process during growth is mastered, in order to obtain high quality optical elements. We are also confident to bring its residual absorption to a level comparable to that of AGS or AGSe, by refining the Bridgman-Sockbarger growth technique and post-growth treatments. At equivalent loss level, LIS would be less subject to thermal lensing than AGS [8, 9] permitting its use in cw OPOs for deep mid-IR generation. The next challenge and effort will be directed to the detailed studies on its eventual ferroelectric properties. Also, we started to investigate other

Li-containing compounds such as  $\text{LiInSe}_2$  (LISe),  $\text{LiGaS}_2$  (LGS),  $\text{LiGaSe}_2$  (LGSe),  $\text{LiGaTe}_2$  (LGT) [22, 104].

### Acknowledgments

This Concerted Action could not have been possible without the grant awarded by the European Commission (DG12-MZCN directorate), in the frame of its International CO-operation program of the 4th Framework

Program (INCO-Copernicus contract No IC15-CT98-0814). The authors are highly grateful to J.F. Bardeau (L.P.E.C., Le Mans, France) and to P. Simon and his collaborators (C.R.M.H.T., Orléans, France) for their expert collaboration in the Raman and IR studies and the use of their experimental facilities. They also acknowledge the use of the nanosecond  $\text{LiNbO}_3$ -based OPO from the DPE/SLCS/LSCO department of the CEA (Saclay, France) for the nonlinearity characterization.

- 
- [1] J.C. Brice, *Crystal Growth Processes*, Blackie & Son, Wiley, New York, 1986.
- [2] G.C. Bhar, R.C. Smith, *Optical properties of II-IV-V<sub>2</sub> and I-III-VI<sub>2</sub> crystals with particular reference to transmission limits*, Phys. Stat. Sol. A **13**, 157-168 (1972).
- [3] J.L. Shay, B. Tell, L.M. Schiavone, H.M. Kasper and F. Thiel, *Energy bands of  $\text{AgInS}_2$  in the chalcopyrite and orthorhombic structures*, Phys. Rev. B **9**, 1719-1723 (1974).
- [4] V.G. Dmitriev, G.G. Gurzadyan and D.N. Nikogosyan, *Handbook of Nonlinear Optical Crystals*, 3rd revised edn, Springer, Berlin, 1999.
- [5] V. Petrov, F. Rotermund and F. Noack, *Generation of high-power femtosecond light pulses at 1 kHz in the mid-infrared spectral range between 3 and 12  $\mu\text{m}$  by second-order nonlinear processes in optical crystals*, J. Opt. A: Pure Appl. Opt. **3**, R1-R19 (2001).
- [6] K. Stoll, J.-J. Zondy and O. Acef, *Fourth-harmonic generation of a continuous-wave  $\text{CO}_2$  laser by use of an  $\text{AgGaSe}_2/\text{ZnGeP}_2$  doubly resonant device*, Opt. Lett. **22**, 1302-1304 (1997).
- [7] D. Lee, T. Kaing and J.-J. Zondy, *An all-diode-laser-based, dual-cavity  $\text{AgGaS}_2$  cw difference-frequency source for the 9 – 11  $\mu\text{m}$  range*, Appl. Phys. B **67**, 363-367 (1998).
- [8] A. Douillet and J.-J. Zondy, *Low-threshold, self-frequency-stabilized  $\text{AgGaS}_2$  continuous-wave subharmonic optical parametric oscillator*, Opt. Lett. **23**, 1259-1261 (1998).
- [9] A. Douillet, J.-J. Zondy, A. Yelisseyev, S. Lobanov and L. Isaenko, *Stability and frequency tuning of thermally loaded continuous-wave  $\text{AgGaS}_2$  optical parametric oscillators*, J. Opt. Soc. Am. B **16**, 1481-1498 (1999).
- [10] R. Hoppe, *Ternäre Oxide der Alkalimetalle*, Bull. Soc. Chim. France **1965**, 1115-1121 (1965).
- [11] G. D. Boyd, H. M. Kasper, and J. H. McFee, *Linear and nonlinear optical properties of  $\text{LiInS}_2$* , J. Appl. Phys. **44**, 2809-2812 (1973).
- [12] T. Kamijoh, K. Kuriyama, *Single crystal growth of  $\text{LiInS}_2$* , J. Cryst. Growth **46**, 801-803 (1979); *Blue-band emission in  $\text{LiInS}_2$  crystals*, J. Appl. Phys. **51**, 1827-1828 (1981).
- [13] K. Kuriyama, T. Kato, A. Takahashi, *Optical band gap and blue-band emission of a  $\text{LiInS}_2$  single crystal*, Phys. Rev. B **46**, 15518-15519 (1992).
- [14] K. Kuriyama and T. Kato, *Optical band gap and photoluminescence studies in blue-band region of Zn-doped  $\text{LiInS}_2$  single crystals*, Solid State Commun. **89**, 959-962 (1994).
- [15] L. Isaenko, I. Vasilyeva, A. Yelisseyev, S. Lobanov, Y. Malakhov, L. Dovlitova, J.-J. Zondy and I. Kavun, *Growth and characterization of  $\text{LiInS}_2$  single crystals*, J. Cryst. Growth **218**, 313-322 (2000).
- [16] A. Yelisseyev, L. Isaenko, S. Lobanov, J.-J. Zondy, A. Douillet, I. Thénot, Ph. Kupecek, G. Mennerat, J. Mangin, S. Fossier and S. Salaiün, *New ternary sulfide for double applications in laser schemes*, in Advanced Solid State Lasers, H. Injeyan, U. Keller, and C. Marshall, eds., OSA-TOPS Vol. **34**, 561-568 (Optical Society of America, Washington D.C., 2000).
- [17] G. M. Knippels, A. P. G. van der Meer, A. M. MacLeod, A. Yelisseyev, L. Isaenko, S. Lobanov, I. Thénot and J.-J. Zondy, *Mid-infrared (2.75-6.0  $\mu\text{m}$ ) second-harmonic generation in  $\text{LiInS}_2$* , Opt. Lett. **26**, 617-619 (2001).
- [18] F. Rotermund, V. Petrov, F. Noack, L. Isaenko, A. Yelisseyev, S. Lobanov, *Optical parametric generation of femtosecond pulses up to 9  $\mu\text{m}$  with  $\text{LiInS}_2$  pumped at 800 nm*, Appl. Phys. Lett. **78**, 2623-2625 (2001).
- [19] J. Brückner, V. Krämer, E. Nowak, V. Riede, B. Schumann, *Crystal growth and characterization of  $\text{LiInS}_2$* , Cryst. Res. Technol. **31**(Supplement), 15-18 (1996).
- [20] A. Eifler, V. Riede, J. Brückner, S. Weise, V. Krämer, G. Lippold, W. Schmitz, K. Bente and W. Grill, *Band gap energies and lattice vibrations of the lithium ternary compounds  $\text{LiInSe}_2$ ,  $\text{LiInS}_2$ ,  $\text{LiGaSe}_2$  and  $\text{LiGaS}_2$* , Jap. J. Appl. Phys. **39**, suppl.39-1, 279-281(2000).
- [21] S. Pearl, S. Fastig, Y. Ehrlich, and R. Lavi, *Limited efficiency of a silver selenogallate optical parametric oscillator caused by two-photon absorption*, Appl. Opt. **40**, 2490-2492 (2001).
- [22] L. Isaenko, A. Yelisseyev, S. Lobanov, V. Petrov, F. Rotermund, G. Slekyas, and J.-J. Zondy,  *$\text{LiInSe}_2$ : A biaxial ternary chalcogenide crystal for nonlinear optical applications in the mid-infrared*, J. Appl. Phys. **91**, 9475-9480 (2002).
- [23] S.K. Kovach, E.E. Semrad, Yu.V. Voroshilov, V.S. Gerasimenko, V.Yu. Slivka, and N.P. Stasyuk, *Preparation and principal physicochemical properties of alkali metal indates and thioindates*, Inorganic Mat. **14**, 1693-1697 (1978) [transl. from Izv. Akad. Nauk SSSR, Neorg. Materialy **14**, 2172-2176 (1978)].
- [24] Z.Z. Kish, V.B. Lazarev, E.E. Semrad, H. Yu. Peresh, and I.V. Galagovets, *Some properties of single crystals of  $\text{LiInS}_2$  and  $\text{NaInS}_2$* , Inorganic Mat. **20**, 647-649 (1984) [transl. from Izv. Akad. Nauk SSSR, Neorg. Materialy **20**, 750-752 (1984)].

- [25] J. Brückner, *I-III-VI Verbindungshalbleiter mit Lithium als Gruppe I-Element: Kristallzüchtung und Charakterisierung*, Ph. D dissertation thesis, Albert-Ludwigs Univ., Freiburg, Germany (1997).
- [26] L. Isaenko, A. Yelissev, J.-J. Zondy, G. Knippels, I. Thénot and S. Lobanov, *Growth and characterization of single crystals of ternary chalcogenides for laser applications*, Opto-Electron. Rev. **9**, 135-141 (2000).
- [27] Z.Z. Kish, E.Yu. Peresh, V.B. Lazarev, and E.E. Semrad, *Systematics and the rules of variations in the properties of  $A^I B^{III} C_2^{VI}$ -type compounds*, Inorganic Mat. **23**, 697-703 (1987) [transl. from Izv. Akad. Nauk SSSR, Neorg. Materialy **23**, 777-784 (1987)].
- [28] R. S. Feigelson and R. K. Route, *Recent developments in the growth of chalcopyrite crystals for nonlinear infrared applications*, Opt. Eng. **26**, 113-119 (1987).
- [29] H. J. Beister, S. Ves, W. Hönle, K. Syassen, and G. Kühn, *Structural phase transitions and optical absorption of  $LiInSe_2$  under pressure*, Phys. Rev. B **43**, 9635-9642 (1991).
- [30] Z.Z. Kish, A.S. Kanishcheva, Yu. N. Mikhailov, V.B. Lazarev, E.E. Sempad, and E. Yu. Peresh, *Synthesis and crystal structure of lithium thioindate  $LiInS_2$* , Soviet Physics /Doklady (Physical Chemistry) **30**, 36-38 (1985) [transl. from Doklady Akad. Nauk SSSR **280**, 398-401 (1985)].
- [31] D.A. Roberts, *Simplified characterization of uniaxial and biaxial nonlinear optical crystals: a plea for standardization of nomenclature and conventions*, IEEE J. Quantum Electron. **28**, 2057-2074 (1992).
- [32] A. Yelissev, S. Lobanov, L. Isaenko and J.-J. Zondy, *Spectroscopic study of Neodimium-doped  $LiInS_2$  single crystals*, Proc. SPIE **3749**, 687-688 (1999). Digest of the 18th Congress of the International Commission for Optics (ICO XVIII Optics for the Millenium) 2-6 Aug. 1999, San Francisco, CA (USA).
- [33] M. Nostrand, R.H. Page, S.A. Payne, L.I. Isaenko, A.P. Yelissev, *Optical properties of  $Dy^{3+}$  and  $Nd^{3+}$ -doped  $KPb_2Cl_5$* , J. Opt. Soc. Am. B **18**, 264-276 (2001).
- [34] W.F. Krupke, *Ytterbium solid-state lasers - the first decade*, IEEE J. Sel. Top. Quantum Electron. **6**, 1287-1296 (2000).
- [35] A. Douillet, J.-J. Zondy, G. Santarelli, A. Makdissi, and A. Clairon, *A phase-locked frequency divide-by-3 optical parametric oscillator*, IEEE Trans. Instr. Meas. **50**, 548-551 (2001).
- [36] G. C. Catella and D. Burlage, *Crystal growth and optical properties of  $AgGaS_2$  and  $AgGaSe_2$* , MRS Bulletin / July 1998, pp. 28-36.
- [37] G. Kühn, E. Piel, H. Neumann, and E. Nowak, *Heat capacity of  $LiInS_2$ ,  $LiInSe_2$  and  $LiInTe_2$  between 300 and 550K*, Cryst. Res. Technol. **22**, 265-269 (1987).
- [38] H. Sobotta, H. Neumann, V. Riede and G. Kühn, *Lattice vibrations and interatomic forces in  $LiInS_2$* , Cryst. Res. Technol. **21**, 1367-1371 (1986).
- [39] H. Neumann, G. Kühn and W. Möller, *High-temperature specific heat of  $AgInS_2$  and  $AgGaSe_2$* , Cryst. Res. Technol. **20**, 1225-1229 (1985).
- [40] J. Mangin, S. Salaiin, S. Fossier, P. Strimer, J.-J. Zondy, L. Isaenko and A. Yelissev, *Optical properties of lithium thioindate*, in "Growth, Fabrication, Devices, and Applications of Laser and Nonlinear Materials", J.W. Pierce, K.I. Schaffers, eds., Proc. SPIE **4268**, 49-57 (2001).
- [41] T.C. Damen, S.P.S. Porto and B. Tell, *Raman effect in zinc oxide*, Phys. Rev. **142**, 570-574 (1966).
- [42] S. Salaiin, A. Bulou, J.Y. Gesland and P. Simon, *Lattice dynamics of the fluoride scheelite  $CaZnF_4$* , J. Phys: Cond. Matter **12**, 7395-7408 (2000).
- [43] V.S. D'Ordyaï, V.A. Stefanovich, E.I. Pan'ko, V.B. Lazarev, E. Yu. Peresh and Z.Z. Kish, *Raman scattering in  $LiInS_2$* , Inorganic Mat. **24**, 461-464 (1988) [transl. from Izv. Akad. Nauk SSSR, Neorg. Materialy **24**, 555-559 (1988)].
- [44] H. Neumann, *Vibrational properties of  $LiGaO_2$ . II: Theoretical model considerations*, Cryst. Res. Technol. **21**, 1361-1366 (1986).
- [45] H. Neumann, *Lattice vibrations in  $A^I B^{III} C_2^{VI}$  chalcopyrite compounds*, Helv. Phys. Acta **58**, 337-346 (1985).
- [46] C. Ebbers, Lawrence Livermore National Laboratory, USA, private communication.
- [47] J. Mangin, P. Strimer and L. Lahlou-Kassi, *An interferometric dilatometer for the determination of thermo-optic coefficients of NLO materials*, Meas. Sci. Technol. **4**, 826-834 (1993).
- [48] P. Korczak and C.B. Staff, *Liquid encapsulated Czochralski growth of silver thiogallate*, J. Cryst. Growth **24/25**, 386-389 (1974).
- [49] G.W. Iseler, *Thermal expansion and seed Bridgman growth of  $AgGaSe_2$* , J. Cryst. Growth **41**, 146-150 (1977).
- [50] J.-J. Zondy, and D. Touahri, *Updated thermo-optic coefficients of  $AgGaS_2$  from temperature-tuned noncritical  $3\omega - \omega \rightarrow 2\omega$  infrared parametric amplification*, J. Opt. Soc. Am. B **14**, 1331-1338 (1997).
- [51] A. Yariv and P. Yeh, *Optical Waves in Crystals*, John Wiley and Sons Ed., New York, 1984.
- [52] J. F. Nye, *Physical Properties of Crystals*, Clarendon Press, Oxford, 2000.
- [53] S. Fossier, *Métrologie des propriétés optiques de cristaux massifs; Etude de  $LiInS_2$ , matériau optiquement non linéaire pour l'infrarouge moyen*, Thèse de Doctorat, Université de Bourgogne, France (2002).
- [54] An Americal National Standard, IEEE Standard on Piezoelectricity, ANSI/IEEE Std 176-1987, IEEE, New York, 1988.
- [55] T.J. Negran, H.M. Kasper and A.M. Glass, *Pyroelectric and electrooptic effects in  $LiInS_2$  and  $LiInSe_2$* , Mat. Res. Bull. **8**, 743-748 (1973).
- [56] C.G.B. Garrett, *Nonlinear optics, anharmonic oscillators and pyroelectricity*, IEEE J. Quantum Electron. **QE-4**, 70-84 (1968).
- [57] R.A. Soref, *Interrelation of pyroelectric and nonlinear optical coefficients in ferroelectric crystals*, IEEE J. Quantum Electron. **QE-5**, 126-129 (1969).
- [58] O. Bidault, S. Fossier, J. Mangin, P. Strimer, A. Yelissev, L. Isaenko, and S. Lobanov, *Study of the pyroelectricity in  $LiInS_2$  crystal*, Solid State Commun. **121**, 207-211 (2002).
- [59] Ch. Ebbers, *Summary of known nonlinear properties of  $LiInS_2$* , preprint UCRL-ID-116744 Feb. 1994, LLNL, Livermore, USA.
- [60] Yu M. Andreev, L.G. Geiko, P.P. Geiko, S.G. Grechin, *Optical properties of a nonlinear  $LiInS_2$  crystal*, Quantum Electronics **31**, 647-648 (2001) [transl. from Kvantov. Elektronika (Moscow) **31**, 647-648 (2001)].
- [61] Yu M. Andreev, V.V. Badikov, P.P. Geiko, S.G.

- Grechin, *Fulfillments of phase-matching conditions and optical characteristics of lithium thioindate nonlinear crystals*, Atmospheric and Oceanic Opt. **14**, 1001-1004 (2001) [transl. from Optika Atmosfery i Okeana **14**, 1087-1090 (2001)].
- [62] W. Chen, J.-J. Zondy, E. Pouillet, L. Isaenko, A. Yelisseyev, and S. Lobanov, *Widely tunable continuous-wave mid-infrared radiation by difference-frequency generation in LiInS<sub>2</sub> crystal*, to be submitted (2003).
- [63] V.G. Dmitriev, D. N. Nikogosyan, *Effective nonlinearity coefficients for three-wave interactions in biaxial crystals of mm<sup>2</sup> point group symmetry*, Opt. Commun. **95**, 173-182 (1993).
- [64] K.V. Diesperov, V. G. Dmitriev, *Effective nonlinear coefficient for sum-frequency generation with collinear phase matching calculated taking account of the birefringence in biaxial crystals*, Quantum Electron. **27**, 433-436 (1997) [transl. from Kvantovaya Elektronika **24**, 445-448 (1997)].
- [65] M.V. Hobden, *Phase-matched second-harmonic generation in biaxial crystals*, J. Appl. Phys. **38**, 4365-4372 (1967).
- [66] J.Q. Yao, T.S. Fahlen, *Calculations of optimum phase match parameters for the biaxial crystal KTiOPO<sub>4</sub>*, J. Appl. Phys. **55**, 65-68 (1984).
- [67] F. Brehat, B. Wyncke, *Calculation of double-refraction walk-off angle along the phase-matching directions in non-linear biaxial crystals*, J. Phys. B: At. Mol. Opt. Phys. **22**, 1891-1898 (1989).
- [68] J. Yao, W. Sheng, W. Shi, *Accurate calculation of the optimum phase-matching parameters in three-wave interactions with biaxial nonlinear-optical crystals*, J. Opt. Soc. Am. B **9**, 891-902 (1992).
- [69] W. Q. Zhang, *Optical parametric generation for biaxial crystals*, Opt. Commun. **105**, 226-232 (1994).
- [70] V. I. Zadorozhnyi, *Improved analytical method for calculating the parameters of phase-matched nonlinear-optical interactions in biaxial crystals*, Opt. Commun. **176**, 489-501 (2000).
- [71] M. H. van der Mooren, Th. Rasing, H. J. A. Bluyssen, *Determination of the type I phase matching angles and conversion efficiency in KTP*, Appl. Opt. **34**, 934-937 (1995).
- [72] R.L. Sutherland, in *Handbook of Nonlinear Optics*, p. 69, Marcel Dekker, Inc., ed., New York, NY (1996).
- [73] F. Rotermund, V. Petrov, F. Noack, V. Pasiskevicius, J. Hellström, F. Laurell, H. Hundertmark, P. Adel, C. Fallnich, *Compact all-diode-pumped femtosecond laser source based on chirped pulse optical parametric amplification in periodically poled KTiOPO<sub>4</sub>*, Electron. Lett. **38**, 561-563 (2002).
- [74] R. Holzwarth, Th. Udem, T.W. Hänsch, J.C. Knight, W.J. Wadsworth, and P. St. J. Russell, *Optical frequency synthesizer for precision spectroscopy*, Phys. Rev. Lett. **85**, 2264-2267 (2000).
- [75] F. Rotermund, V. Petrov, *Femtosecond noncollinear optical parametric amplification in the mid-infrared range with 1.25 μm pumping*, Jpn. J. Appl. Phys. **40**, 3195-3200 (2001).
- [76] H. J. Liu, G. F. Chen, W. Zhao, Y. S. Wang, T. Wang, S. H. Zhao, *Phase-matching analysis of noncollinear optical parametric process in nonlinear anisotropic crystals*, Opt. Commun. **197**, 507-514 (2001).
- [77] W.Q. Zhang, *Group-velocity matching in the mixing of three noncollinear phase-matched waves for biaxial crystal*, Opt. Commun. **221**, 191-197 (2003).
- [78] J.-J. Zondy, M. Abed, and A. Clairon, *Type-II frequency doubling at λ = 1.30 μm and λ = 2.53 μm in flux-grown potassium titanyl phosphate*, J. Opt. Soc. Am. B **11**, 2004-2015 (1994).
- [79] R.C. Eckardt, H. Masuda, Y.X. Fan, and R.L. Byer, *Absolute and relative nonlinear optical coefficients of KDP, KD\*P, BaB<sub>2</sub>O<sub>4</sub>, LiIO<sub>3</sub>, MgO:LiNbO<sub>3</sub>, and KTP measured by phase-matched second-harmonic generation*, IEEE J. Quantum Electron. **26**, 922-933 (1990).
- [80] J.-J. Zondy, *Comparative theory of walkoff-limited type-II versus type-I second harmonic generation with Gaussian beams*, Opt. Commun. **81**, 427-440 (1991).
- [81] B. Boulanger, J. P. Feve, G. Marnier, C. Bonnin, P. Villeval, J. J. Zondy, *Absolute measurement of quadratic nonlinearities from phase-matched second-harmonic generation in a single KTP crystal cut as a sphere*, J. Opt. Soc. Am. B **14**, 1380-1386 (1997).
- [82] J.-J. Zondy, D. Touahri, O. Acef, *Absolute value of the d<sub>36</sub> nonlinear coefficient of AgGaS<sub>2</sub>: prospect for a low-threshold doubly resonant oscillator-based 3:1 frequency divider*, J. Opt. Soc. Am. B **14**, 2481-2497 (1997).
- [83] R. A. Kaindl, F. Eickemeyer, M. Woerner, T. Elsaesser, *Broadband phase-matched difference frequency mixing of femtosecond pulses in GaSe: experiment and theory*, Appl. Phys. Lett. **75**, 1060-1062 (1999).
- [84] P. Canarelli, Z. Benko, R. Curl, and F.K. Tittel, *Continuous-wave infrared laser spectrometer based on difference frequency generation in AgGaS<sub>2</sub> for high-resolution spectroscopy*, J. Opt. Soc. Am. B **9**, 197-202 (1992).
- [85] W. Chen, J. Burie, D. Boucher, *Midinfrared cw difference-frequency generation using a synchronous scanning technique for continuous tuning of the full spectral region from 4.7 to 6.5 μm*, Rev. Sci. Instrum. **67**, 3411-3415 (1996).
- [86] D. Lee, T. Kaing, and J.-J. Zondy, *An all-diode-laser-based, dual-cavity AgGaS<sub>2</sub> cw difference-frequency source for the 9 – 11 μm range*, Appl. Phys. B **67**, 363-367 (1998).
- [87] W. Chen, G. Mouret, D. Boucher, *Difference-frequency laser spectroscopy detection of acetylene trace constituent*, Appl. Phys. B **67**, 375-378 (1998).
- [88] J.-J. Zondy, *The effects of focusing in type-I and type-II difference-frequency generations*, Opt. Commun. **149**, 181-206 (1998).
- [89] A.D. Ludlow, H.M. Nelson, and S.D. Bergeson, *Two-photon absorption in potassium niobate*, J. Opt. Soc. Am. B **18**, 1813-1820 (2001).
- [90] L. Isaenko, A. Yelisseyev, S. Lobanov, V. Petrov, F. Rotermund, J.-J. Zondy, G.H.M. Knippels, *LiInS<sub>2</sub>: A new nonlinear crystal for the mid-IR*, Mat. Sci. Semicond. Proc. **4**, 665-668 (2001).
- [91] H. Mabuchi, E.S. Polzik, and H.J. Kimble, *Blue-light-induced infrared absorption in KNbO<sub>3</sub>*, J. Opt. Soc. Am. B **11**, 2023-2029 (1994).
- [92] L. Shiv, J.L. Sorensen, and E.S. Polzik, *Inhibited light-induced absorption in KNbO<sub>3</sub>*, Opt. Lett. **20**, 2270-2272 (1995).
- [93] L. Isaenko, A. Yelisseyev, L. Lobanov, I. Vasilyeva, V. Petrov, V. Nadolnny, J. Smirnova, J.-J. Zondy, *Effect of deviation from stoichiometry on photoinduced absorption in LiInS<sub>2</sub> nonlinear crystals*, Abstract of the 8th

- European Conf. on Solid State Chemistry (ECSSC-8), 4-7 July, 2001, Oslo, Norway, p. 119 (2001).
- [94] U. Simon, S. Waltman, I. Loa, F.K. Tittel, and L. Hollberg, *External-cavity difference-frequency source near 3.2  $\mu\text{m}$  based on combining a tunable diode laser with a diode-pumped Nd:YAG laser in AgGaS<sub>2</sub>*, J. Opt. Soc. Am. B **12**, 323-327 (1995).
- [95] M.A. Acharekar, J.L. Montgomery, and R.J. Rapp, *Laser damage threshold measurements of AgGaSe<sub>2</sub> crystal at 9  $\mu\text{m}$* , in Laser-Induced Damage in Optical Materials: 1991, H.E. Bennett, L.L. Chase, A.H. Guenther, B.E. Newnam, M.J. Soileau, eds., Proc. SPIE **1624**, 46-54 (1992).
- [96] A. Harasaki and K. Kato, *New data on the nonlinear optical constant, phase-matching and optical damage of AgGaS<sub>2</sub>*, Jpn. J. Appl. Phys. **36**, 700-703 (1997).
- [97] B.C. Ziegler and K.L. Schepler, *Transmission and damage-threshold measurements in AgGaSe<sub>2</sub> at 2.1  $\mu\text{m}$* , Appl. Opt. **30**, 5077-5080 (1991).
- [98] Yu. M. Andreev, V. V. Badikov, V. G. Voevodin, L.G. Geiko, P.P. Geiko, M.V. Ivashchenko, A.I. Karapuzikov, I.V. Sherstov, *Radiation resistance of nonlinear crystals at a wavelength of 9.55  $\mu\text{m}$* , Quantum Electronics **31**, 1075-1078 (2001) [transl. From Kvantov. Elektronika (Moscow) **31**, 1075-1078 (2001)].
- [99] J. Mangin, G. Jeandel, and G. Marnier, *Temperature dependence of polarization in KTiOPO<sub>4</sub> single crystals*, Phys. Stat. Sol. A **117**, 319-323 (1990).
- [100] M. Yamada, N. Nada, M. Saitoh, and K. Watanabe, *First-order quasi-phase matched LiNbO<sub>3</sub> waveguide periodically poled by applying an external field for efficient blue second-harmonic generation*, Appl. Phys. Lett. **62**, 435-436 (1993).
- [101] G. Rosenman, A. Skliar, D. Eger, M. Oron, and M. Katz, *Low temperature periodic electrical poling of flux-grown KTiOPO<sub>4</sub> and isomorphic crystals*, Appl. Phys. Lett. **73**, 3650-3652 (1998).
- [102] V. Gopalan, T. E. Mitchell, Y. Furukawa, and K. Kitamura, *The role of nonstoichiometry in 180° domain switching of LiNbO<sub>3</sub> crystals*, Appl. Phys. Lett. **72**, 1981-1983 (1998).
- [103] M. Nakamura, S. Takekawa, K. Terabe, K. Kitamura, T. Usami, K. Nakamura, H. Ito, and Y. Furukawa, *Near-stoichiometric LiTaO<sub>3</sub> for bulk quasi-phase-matched devices*, Ferroelectrics **273**, 199-204 (2002).
- [104] L. Isaenko, A. Yelissev, S. Lobanov, A. Titov, V. Petrov, J.-J. Zondy, P. Krinitsin, A. Merkulov, V. Vedenyapin, J. Smirnova, *Growth and properties of LiGaX<sub>2</sub> (X=S, Se, Te) single crystals for nonlinear optical applications in the mid-IR*, Cryst. Res. Technol. **38**, 379-387 (2003).